Use of Transmission Electron Microscopy to Identify Nanocrystals of Challenging Protein Targets

by

Hilary Paige Stevenson

Bachelor of Science, Denison University, 2007.

Submitted to the Graduate Faculty of

The University of Pittsburgh School of Medicine

in partial fulfillment of the requirements for the degree of

Doctor of Philosophy

University of Pittsburgh

2014

UNIVERSITY OF PITTSBURGH

SCHOOL OF MEDICINE

This dissertation was presented

by

Hilary Paige Stevenson

It was defended on

May 8, 2014

and approved by

Angela Gronenborn, PhD, Structural Biology

Guillermo Romero, PhD, Pharmacology and Chemical Biology

Andrew VanDemark, PhD, Biological Sciences

William Furey, PhD, Thesis Committee Chair, Pharmacology and Chemical Biology

Guillermo Calero, MD, PhD, Thesis Advisor, Structural Biology

**Use of Transmission Electron Microscopy to
Identify Nanocrystals of Challenging Protein Targets**

Hilary Paige Stevenson, BS

University of Pittsburgh, 2014

Existing crystallographic methods require micro-meter sized crystals for structure determination. However, due to their intrinsic disorder, many biological molecules are not amenable to the formation of such large crystals. X-ray free electron lasers (X-FEL) provide a new avenue to determine crystal structures of such challenging biological targets, as this technology enables the acquisition of diffraction patterns from nano-meter sized crystals. As proof of principle, X-FELs have been employed to determine crystal structures obtained using conventional crystallographic methods. A major limitation to the application of X-FEL technology to de novo structure determination of challenging targets is the inability to identify protein nanocrystals (NCs) that are suitable for diffraction by X-FEL. Here, I establish a method using Transmission Electron Microscopy (TEM) to reliably identify and characterize protein NCs. I then use this method to compare crystallographic seeding techniques to identify conditions that yield larger and higher quality NCs.

Negative stain Transmission Electron Microscopy (TEM) was used to detect NCs of several challenging targets. One such challenging target is a Family B G-Protein Coupled Receptor, the parathyroid hormone receptor (PTHR1). Crystallization trials of the PTHR1 were performed to isolate potential NC containing drops. UV tryptophan fluorescence microscopy was employed to identify UV positive granular aggregates. Positive samples were examined by negative stain TEM with the aim of distinguishing NCs from protein aggregates. In those PTHR1 NCs that were identified, the presence of negative stained lattices was used as an indicator of their proteic nature. This method was successfully employed to identify protein NCs of seven additional challenging targets. Crystal quality was determined by calculating fast Fourier transforms of NC lattices.

TEM was also used to visualize crystallographic seeds for the first time, and identify optimal seeding conditions.   The quality of seeds produced by traditional seeding methods were compared to those produced by "nanoseeding," a novel method in which multiple millimeter seed beads are used. The nanoseeding approach proved to be far superior to traditional methods at producing larger and higher quality seeds. This work demonstrates that TEM identified NCs, as well as fragmented NCs are powerful tools for optimizing and growing crystals.

TABLE OF CONTENTS

LIST OF TABLES

LIST OF FIGURES

PREFACE

"By perseverance the snail reached the ark."

- Charles H. Spurgeon

This work would not have been possible without the tireless efforts of many people. This help has come in many forms, be it moral support, direct teaching, training in the necessary laboratory skills to move my project forward or editing milestone documents. There are also many who have served as mentors along the way. Without their wisdom and support I would not have made it through.

I would first like to thank my committee members: Drs. Bill Furey, Angela Gronenborn, Guillermo Romero and Andy VanDemark. You have seen me through a tough project and I am grateful for your suggestions and guidance. I very much appreciate the time you have given to furthering my graduate career.

Dr. Guillermo Calero is a unique mentor in that he has helped me in all sectors of graduate school. This has included patiently giving his time to teach me what has amounted to be a large skill set at the bench. He has provided exciting and engaging projects while also allowing me to try, what can be described generously as "creative" approaches to research problems, even when it was obvious that it may not have been the most efficient path. I am extremely grateful for the amazing opportunities that I have had while in the lab, be it, conferences in Hawaii or

trips to LCLS. Furthermore I am extremely grateful for his encouragement to pursue my dream of medical school; it has meant a great deal that you are so supportive of my plans for the future while also believing in my capabilities as a researcher. And none of this would have been possible if you hadn't take the chance on me, and let me join the lab, even though it was anything but easy to take me on. I know the day will soon come when I am calling you up for advice, even though I am long gone from the lab.

Dr. Aina Cohen has served as another incredible mentor during my time in graduate school, and I expect that just as is the case with Guillermo, she will play an important part in my future endeavors. Aina has introduced me to new and exciting components of structural biology, instilled in me an enthusiasm for research while also making me believe in my capabilities as a researcher. Our lab's collaborations have provided me with interesting projects and exciting publications for which I am very grateful.

Thank you also to the Molecular Pharmacology graduate program. I think it is safe to say that with every graduate student it takes a village to see her to defense day and it is particularly so in my case. Thank you to Drs. Patrick Pagan, Guillermo Romero, and Bruce Freeman of the department. I have not always been the easiest student in the program to push forward, and you have gone above and beyond to get me through. And I don't know what I would have done without all of you backing me up during my younger graduate student years. Guillermo Romero in particular has served as an anchor during graduate school. He has supported me in all of my scientific endeavors while also sustaining me through the typical (and not so typical) challenges that are inherent to graduate school itself.

The work I present in this thesis would not be possible without the contributions of many people who have taught me specific laboratory skills while also giving me guidance on my

various projects. I am particularly grateful to Sasha Makhov, Tommy Tillman, Laurie Betts, Lisa Chariton, Christopher Divito and Aaron Hirko. I am incredibly grateful to the Laboratory of GPCR biology, particularly Drs. Guillermo Romero, Peter Friedman, Jean-Pierre Vilardaga and Alessandro Bisello who have given me invaluable advice on the PTHR1 project that has encompassed many years of work. Their openness and willingness to collaborate has provided me with so many opportunities and room to grow as a scientist, for which I'm very grateful.

I would like to thank the numerous friends whom I've met during my development as a researcher who have supported me during graduate school. Without your friendship, encouragement and humor I would not have made it. In particular, I want to give a special thanks to Nicole Brandon, Punya Navaratnarajah and The Pharmers; you are saints for putting up with me.

In addition to the invaluable support of Dr. Calero I must acknowledge those mentors that originally lead me into science. I owe a particular debt of gratitude to Mrs. Martha Panning and Dr. Kimberly Specht.

Lastly, I dedicate this work to my parents Kathleen and David Stevenson. Without their tireless support, endless encouragement, and stubborn resistance to letting me give up, this work would not be possible.

1.0 INTRODUCTION

Structural biologists who wish to determine and analyze structures of large proteins rely on the well-established techniques of X-ray crystallography. However, obtaining crystals of any protein is not always feasible, particularly when challenging targets are being pursued. As a result, specific techniques for crystallizing targets such as membrane proteins have become more robust in the last 15 years in order to overcome crystallization challenges. One example of this capitalizes on the instability of membrane receptors after extraction with detergent, and uses specific detergent concentrations to crystallize membrane receptors. However, in many instances, particularly with the G-Protein Coupled Receptors, the best efforts of structural biologists have failed to yield visible crystals. And in some cases, even after exhaustive optimization efforts, only small unusable crystals are obtained. Rather than focus on growing large crystals, as many have done in that past, this work seeks to use G-Protein Coupled Receptors as a model system to uncover novel methods for identifying and optimizing crystals for difficult targets for which no visible or usable crystals have previously been observed.

1.1 G -PROTEIN COUPLED RECEPTORS

G-protein coupled receptors (GPCRs) represent over 40% of drug targets in clinical use (1, 2). More than a thousand GPCRs have been identified to date, and they have immensely varying roles in human physiology (3, 4) including controlling cardiovascular homeostasis and

pathology (5), immune response (6, 7), and neurobiology that contributes to psychiatric conditions (8, 9), olfaction (10), taste (11) and vision (12, 13). Though these receptors play diverse roles in many different disease pathways, GPCRs share a common motif: seven transmembrane α-helices which are connected by alternating extracellular and intracellular loops. These extracellular and intracellular loops are the major sites of interactions for ligands and heterotrimeric G-proteins, respectively.

1.1.1   GPCR Structure and Classification

All GPCRs share the same basic structural features: a seven transmembrane α-helical structure that is connected by alternating loops. However, there are significant structural differences amongst GPCRs that can be used to categorized them into three distinct families, as well as several smaller seven-transmembrane families (14). All of these families share significant sequence homology amongst group members, but have as low as 2% sequence homology with GPCRs of other classes (3, 14, 15). Although these differences amongst the families of GPCRs are complex, an underlying distinction lies in the extracellular domains of these receptors as illustrated in **Figure 1**. This figure compares representative full-length crystal structures from the A and B Families as well as a full-length model of a Family C, of which only the extracellular domain has been solved. As this figure illustrates, the most noticeable difference between the structures is the distinct variation between their extracellular domains. It should be noted that to "solve" a structure, in the cases described in this text, refers to determining the relative coordinates of non-hydrogen atoms to sub-angstrom accuracy, such that specific residues are identifiable, reliable interatomic interaction distances can be measured, and atomic surface details revealed.

The Family A or Rhodopsin Family is the largest and most diverse of the GPCR families, comprised of several hundred members (3). Receptors from this family bind a variety of small molecule agonists such as small molecule ligands, neuropeptides and glycoproteins (16-19). These receptors commonly have a small extracellular domain (with the exception of glycoprotein hormone receptors) compared to other GPCR families (20). Binding sites for these ligands lies deep within the core of the receptor, interacting with TM3, 4, 5, 6 and 7 (16-19, 21). All but two of the 21 unique structures solved to date are of Family A receptors.

The Secretin or Family B GPCRs are composed of 15 different members and regulate important physiological functions such as controlling exocrine and endocrine functions (14, 15, 22-24). Unlike the Family A receptors, which includes a large variety of agonist types, the Family B GPCR bind extensively to endogenous polypeptide hormones approximately 30-40 amino acids in length (25). Such peptide hormones include secretin, vasoactive intestinal peptide, gastric inhibitory polypeptide, parathyroid hormone, and calcitonin (25). These receptors have common N-terminal ecto-domains approximately 120 amino acids in length, illustrated in the top portion of the Secretin Family GPCR example in **Figure 1**. Family B GPCRs and their ligands are thought to interact by a "two domain" model (26, 27). In this model, the C-terminal of the ligand first binds to the receptor's N-terminal ecto-domain. The ecto-domain of the receptor then orients the N-terminus of the polypeptide to the appropriate position for interacting with the extracellular loops and transmembrane helices of the GPCR (28).
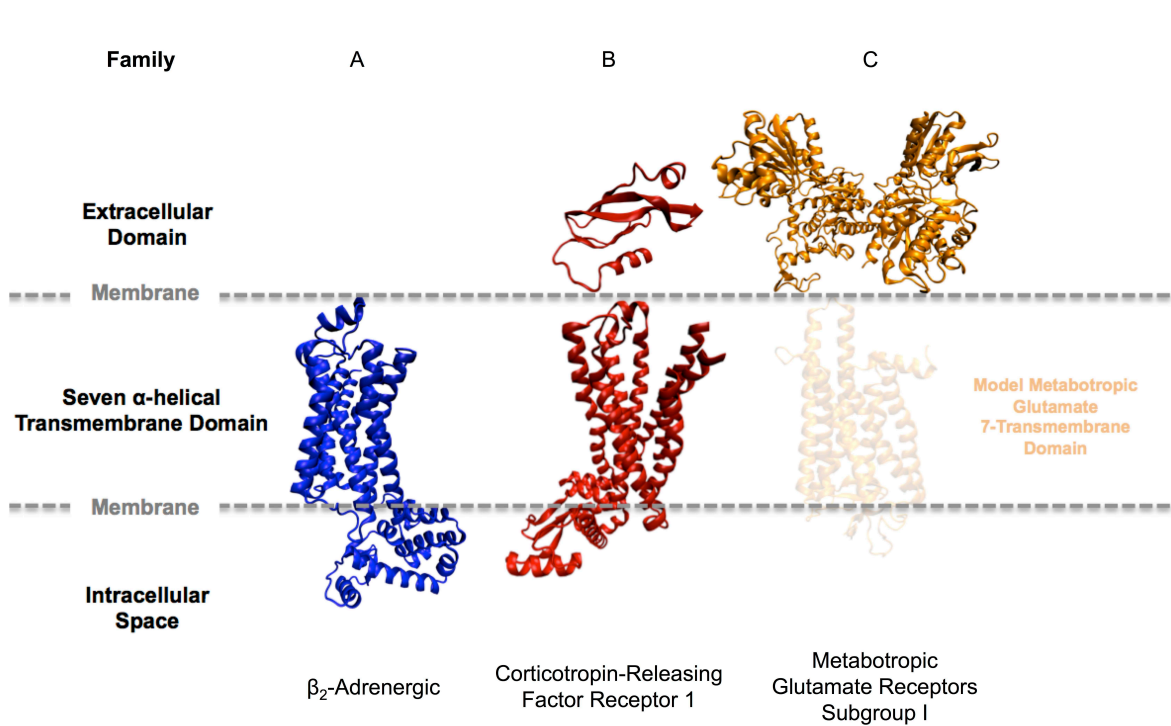
Figure 1. Crystallographically determined structures of the three main classes GPCR.

The Family C GPCRs, also known as the metabotropic glutamate receptor family, have a significantly larger extracellular domain then the other GPCR families, 500-600 amino acids in length (29, 30). The endogenous agonists of these receptors include sugar molecules, amino acids and ions (31, 32). No full-length structures of these receptors have been solved. Crystal structures of the extracellular domains of these receptors are reminiscent of a clamshell, with two lobes (33-35). This conformation oscillates between open and closed conformations with agonists being thought to bind in-between the cleft formed by the lobes (33-35). Another notable feature of these receptors is that they exist in a constitutively dimeric conformation within the cellular membrane, as both hetero and homo dimers (36-38).

1.1.2 GPCR Activation Cycle
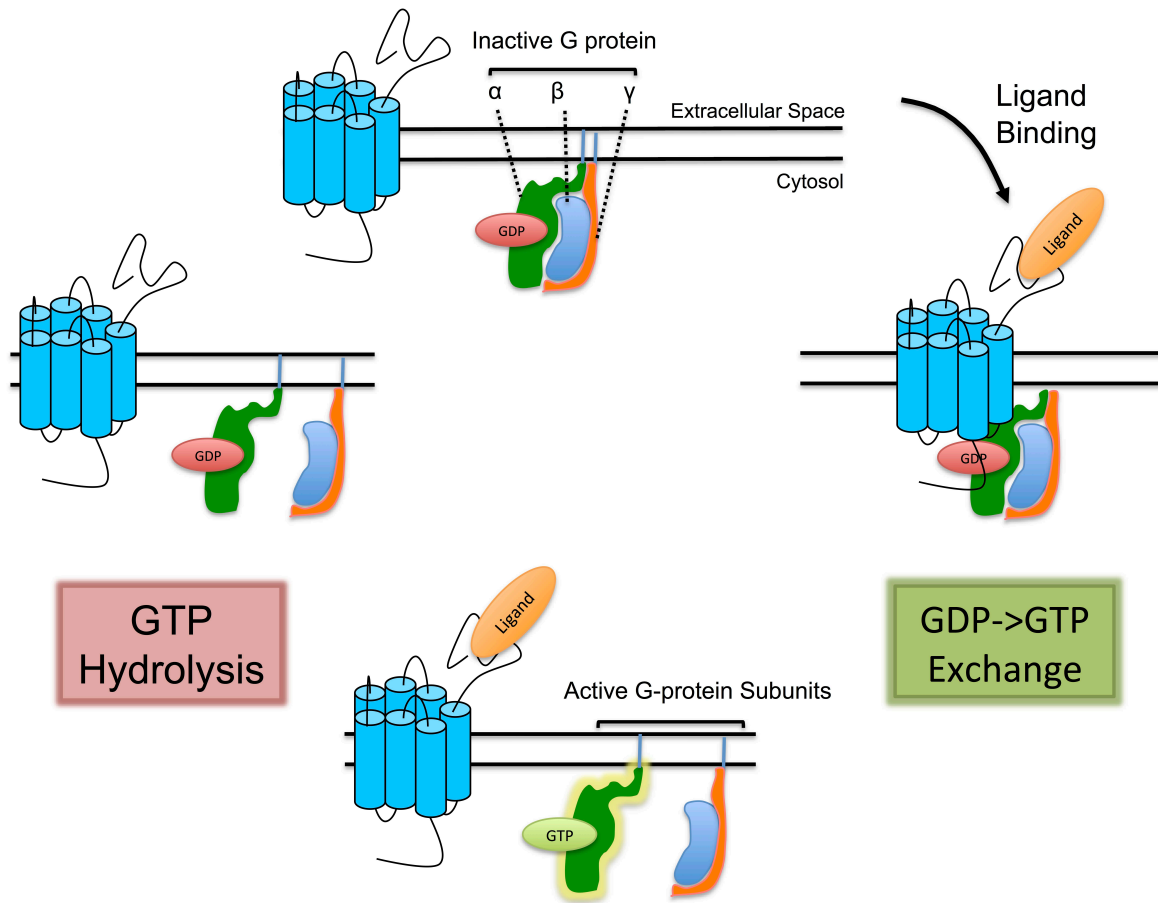
Figure 2. GPCR signaling.

In the classical GPCR model, the binding of an extracellular agonist to the receptor triggers an intracellular conformational change that leads to the binding and activation of heterotrimeric G proteins (HGP) as shown in **Figure 2**. Activation of the HGP is made possible by a ligand-activated GPCR acting as a guanine nucleotide exchange factor (GEF). In this role the GPCR acts to facilitate the exchange from GDP to GTP of the α-subunit of the HGP. The HGP separates into a GTP-bound α-subunit and βγ subunits. These separated subunits are free to participate in downstream signaling until GTP hydrolysis occurs. The inactive GDP bound α-

subunit then reassembles with its βγ counterparts and will remain inactive until the GPCR activates the HGP again. Activated HGP serves as the relays for the GPCR, linking the activation of the receptor to downstream cellular signaling. However, though GPCR GEF activity is stimulated by ligand binding, constitutive, low level GEF activity, is also a prevalent feature of these receptors (39-41). There are many Gα subunits, all of which contribute to different downstream signaling pathways (42, 43). The Gα subunit used for crystallographic examination of the interaction between GPCR and its HGP is $G\alpha_S$, as it binds most of the GPCRs crystallized to date (44, 45). $G\alpha_S$ plays many roles in downstream signaling events once activated by its GPCR. One major role is to activate adenylate cyclase, thus acting as a relay for the GPCR in the AMP-dependent pathway (46). The biological consequences of activation of this pathway can include: increase heart rate, stimulation of neuronal activity and induction of smooth muscle relaxation (46-48).

The common signaling behavior of all GPCRs across several structurally diverse families leads to questions of how such little sequence homology can result in universal signaling behavior. Obtaining high-resolution structures of multiple activation states of Family A GPCRs has shed light on the basic structure and function of the largest of the GPCR classes. However, in obtaining crystal structures of different activation states of the β_2AR for example, it became evident that the constitutive activity of GPCRs stems from the inherent flexibility of the receptor, the same flexibility that requires stabilization in order to achieve crystallization. These insights will likely be essential for the continued capture of the function and structure of other GPCR families by X-ray crystallography.

1.1.3 Strategies for the Crystallization of GPCRs

Crystallizing and solving high-resolution structures of GPCRs has been a long standing crystallographic challenge. As further elaborated upon in section 1.2, highly ordered crystals are essential to X-ray crystallography as they are the backbone for solving structures of large proteins such as GPCRs. The challenge in obtaining these crystals is made evident by the long gap between the first GPCR structure solved in 2000, Rhodopsin, and the second, active form of the receptor Opsin, solved in 2008 (49-51). Many hurdles are associated with the crystallization of these proteins. The first is obtaining a functional receptor, which is particularly challenging because these receptors are naturally stabilized by lipids, requiring specific detergents to extract and stabilize these receptors. Additionally, these large, seven transmembrane receptors have crystallization-averse flexible regions. As such, these receptors' disordered regions must be stabilized. The constitutive basal activity of GPCRs, a phenomenon consistently observed in the Family A receptors, also proves to be a crystallization challenge.

1.1.3.1 Protein Manipulation Strategies for Crystallizing GPCRs

Beyond obtaining an expression and purification protocol that produces adequate quantities of folded, functional protein, specific approaches to overcome the challenges associated with crystallizing these proteins have become essential. The primary barrier to crystallization of the receptor is a result of the inherent flexible domains of the protein. In order to overcome this challenge, crystallographers have focused on removing disordered regions of the protein that would interfere with crystallization. As shown in **Figure 3**, there are three main areas of predicted disorder that are evident in the Family A GPCRs structures that have already

been solved. The first two, the N and C terminus, always require truncation in order to grow diffractable crystals. The third, and most challenging target for stabilization is the unstable 3rd intracellular loop (ICL3). This region is, in a broadly simplistic view, the site of interaction of HGPs. Given the continuative activity of the receptor when not bound by ligand, stabilizing this region is required for crystallization (52).
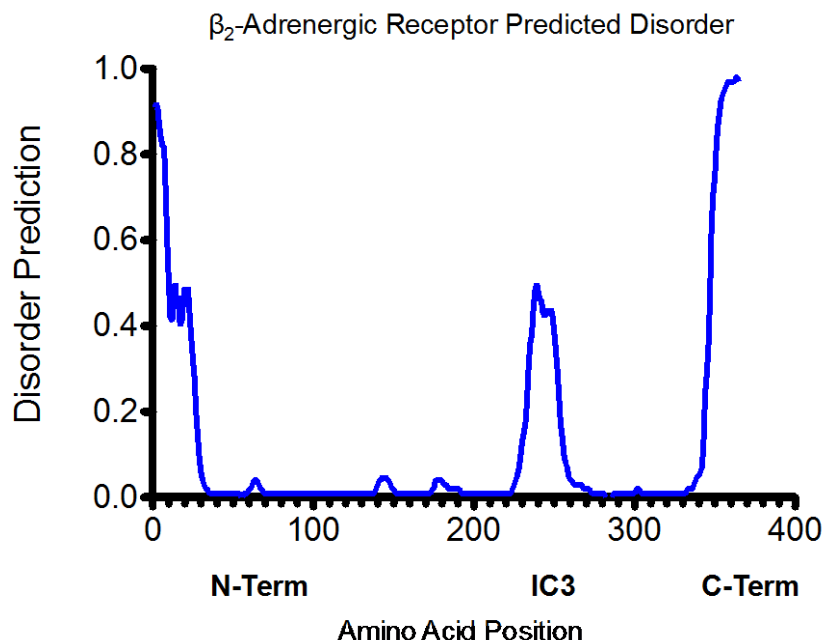
Figure 3. Predicted disorder for β$_2$AR, generated by DISOPRED2

One of the earliest approaches for stabilizing the ICL3, first successfully applied to the β$_2$AR in its inactive conformation, was an antigen-binding fragment (Fab) designed against the ICL3. The Fab binding improved crystal contacts and stabilized the ICL3 as illustrated in **Figure 4A** (52). The next successful technique applied to stabilize the ICL3, which is still widely used today, is to truncate the ICL3 and insert T4-lysozyme in its place. In addition to occupying the region previously filled by the ICL3, T4-lysozyme provides crystal contacts that enhance the likelihood of successful crystallization. This technique has been successfully utilized for 19

unique structures of Family A GPCRs (**Figure 4B)** (53-60). A third approach, illustrated in **Figure 4C,** was utilized to solve the inactive turkey β_1AR receptor structure (61). Of the three techniques described here for inactive conformations of the receptor, only this approach left the ICL3 mostly intact. Instead of using a Fab or a GPCR-T4-lysozyme construct, the ICL3 was mutated and thermostabilized to reduce the intrinsic flexibility of the loop. The resulting mutations locked the ICL3 into an inactive, antagonist bound conformation, thereby inhibiting the agonist-independent constitutional activity of the protein (61). All GPCR structures solved to date rely on truncating the N and C terminal, removing glycosylation in extracellular loops of the receptor and stabilizing the ICL3 through use of a Fab, T4-lysozyme or thermostabilization of the ICL3.
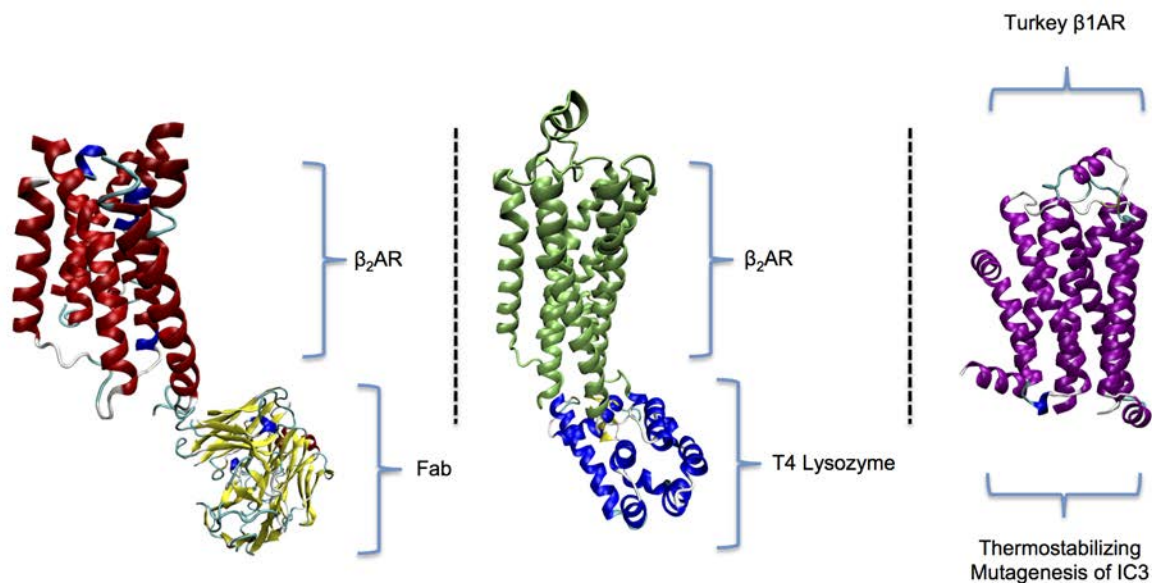
Figure 4. Successful Family A GPCR crystallization approaches.

Point mutations, aimed at thermostabilizing Family A GPCRs, have been performed alongside the modifications of the ICL3 for successfully crystallized receptors. One of the apparent challenges to crystallizing GPCRs is the destabilization that these receptors experience

as a result of the necessary extraction of these receptors from the lipid bilayer with detergents. Part of this destabilization occurs because of the loss of lateral pressure that the native membrane previously provided the receptor before detergent extraction. This loss results in unfolding and aggregation. Several approaches have historically been used to identify the mutations that have the greatest contribution to receptor stability. One approach, utilized for the stabilization for the turkey β_1AR and human adenosine A_{2A} receptors, is to measure the effect of mutations on the stability of the receptor in detergent (62, 63). The first step of the method is to pre-incubate the receptor with radioligand. After incubation, the temperature is increased so as to denature the protein, followed by quenching of the reaction on ice and separating out the remaining ligand-bound receptor by mini gel-filtration columns. The ^{3}H-labeled ligand signal is measured providing a means to identify which thermostabilization mutations have a positive effect on protein stability by quantifying the ligand binding activity of mutant constructs (64).

A method, more commonly used today, is to screen the consequence of mutations on the melting temperature of proteins using a fluorescent dye that binds to an unfolded protein. A temperature gradient can be used to identify the temperature at which the receptor unfolds. This method is high-throughput, as it is adaptable to a Real-Time PCR setup. Though the classical melting temperature assay for soluble proteins relied on sypro-orange (65-67) it could not be used for GPCRs due to the presence of detergents that increase background fluorescence to the point of masking the signal (68). However, the recent application of thiol-specific fluorochrome N-[4-(7-diethylamino- 4-methyl-3-coumarinyl)phenyl]maleimide (CPM) allows for the same thermo-gradient assay without the high background fluorescence (69). This assay can be used to screen for the effect of mutations geared at increasing the melting temperature of the protein, as

well as identifying, in a high throughput manner the consequence of crystallography conditions on receptor stability.

Conformation	Inactive	Active	HGP Bound
Challenge	Stabilize Flexible ICL3	Constitutive β_2AR Activity and ICL3 Flexibility	Stabilization of β_2AR-Gαs$\beta\gamma$ Complex
Ligand	Inverse Agonist or Irreversible Antagonist	High Affinity Agonist	High Affinity Agonist
Approach #1	Fab Against ICL3	Gαs Mimicking Nanobody	Cross-Linking β_2AR-Gαs$\beta\gamma$ Complex
Approach #2	Replace ICL3 with T4-Lysozyme		Nanobody Mediated Stabilization of Complex

Table 1. Approaches to crystallizing multiple activation states of GPCRs

1.1.3.2 Crystallization of Multiple GPCRs Conformations

As shown in Table 1, multiple conformations of the Rhodopsin Family have been crystallized. Crystallization approaches were initially focused on inactive conformations stabilized by the use of antagonists and inverse agonists. Use of ligands as well as modifications to the ICL3 were employed to inhibit the constitutive activity of the protein, which made crystallizing the receptor more difficult.

The first GPCR to be crystallized in an active conformation was the human β_2AR in complex with an irreversible agonist that was covalently tethered to the receptor through an engineered disulfide bond (70). The engineered agonist irreversibly blocks ligand binding. Furthermore, excess inverse agonist was not sufficient to affect the irreversible agonist coupling of β_2AR coupling to $G\alpha_S\beta\gamma$ (G_S). Despite the irreversible nature of the agonist, molecular dynamics simulations suggested that the agonist bound conformation would likely relax into an inactive-like conformation without an HGP present. As a result, the next crystal structure to be solved employed an approach similar to that of the Fab-ICL3 stabilization. Due to the challenges involved in stabilizing the active state of the receptor without HGP present, a nanobody (Nb80) (a camelid antibody fragment that lacks the heavy chain) was developed (44). This nanobody, which showed G protein like activity, stabilized an active conformation of the receptor in the presence of agonist (**Figure 5**). This results in small changes to the binding pocket, as well as a large 11Å movement away from the core of TM6. Changes similar to the active form of Opsin (49) were observed in this structure, showing rearrangement of TM5s and 7 as shown in **Figure 5**.
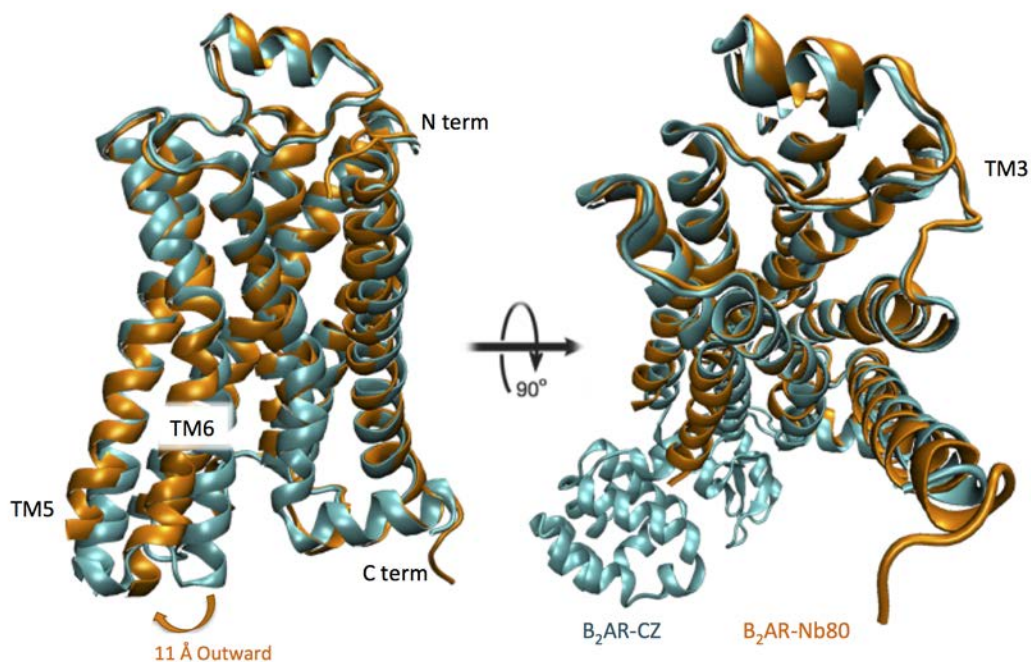
Figure 5. Comparison of the agonist Nb80 stabilized crystal structures of the β_2AR (orange) to the inverse agonist carazolol bound β_2AR (cyan).

Within the same year, the structure of agonist bound β_2AR in complex with nucleotide free $G\alpha_S\beta\gamma$ was solved. To stabilize this structure, llamas immunized with crosslinked β_2AR and $G\alpha_S\beta\gamma$ were used to isolate a nanobody that prevents dissociation of the complex (Nb35). The observed structural changes seen in the nanobody stabilized agonist bound β_2AR structure were highly homologous with those observed in the β_2AR-$G\alpha_S$ structure with the exception of a 3Å movement outward of the cytoplasmic end of TM6 where it interacts with $G\alpha_S$. $G\alpha_S$ is made up of two domains, the largest being the Ras-like GTPase domain, which is the site of interaction with subunits β and γ. The second subunit of G_S is the α-helical domain and the border between these two subunits of G_S makes up the nucleotide-binding pocket. As shown in **Figure 6**, the primary site of interaction between β_2AR and G_S is with the Ras-like GTPase domain. There is

no observed interaction of the β or γ subunits with the receptor. The $G\alpha_S$ subunit interacts with the ILC2, TM5 and TM6 of the receptor. These observations gave rise to a model of the interaction of β_2AR with $G\alpha_S\beta\gamma$. In this model, the release of GDP is facilitated by agonist bound β_2AR. This results from the binding of the receptor to the Ras-like GTPase domain. This interaction produces a downward movement of the α-helical domain, facilitating a nucleotide free state.

The three conformations of the β_2AR solved to date provide exciting insights into the functionality of the receptor and the effects of agonists and antagonist on structure and function. Furthermore, the surprising structural interface between β_2AR and G_S may inform further biochemical study. In addition to these findings, the development of the techniques that made these structures possible may ultimately prove to be as important as the insights the structures themselves provide. As illustrated in **Figure 1** a representative structure from only one of the other GPCRs has been solved, the Secretin family, and these structures are limited to their inactive conformations. Applying the successful Family A methods to the crystallography of other GPCR families may broaden the array of possible structures that can be solved. These techniques may also provide a means to solving structures representing multiple conformations of a Family B GPCR.
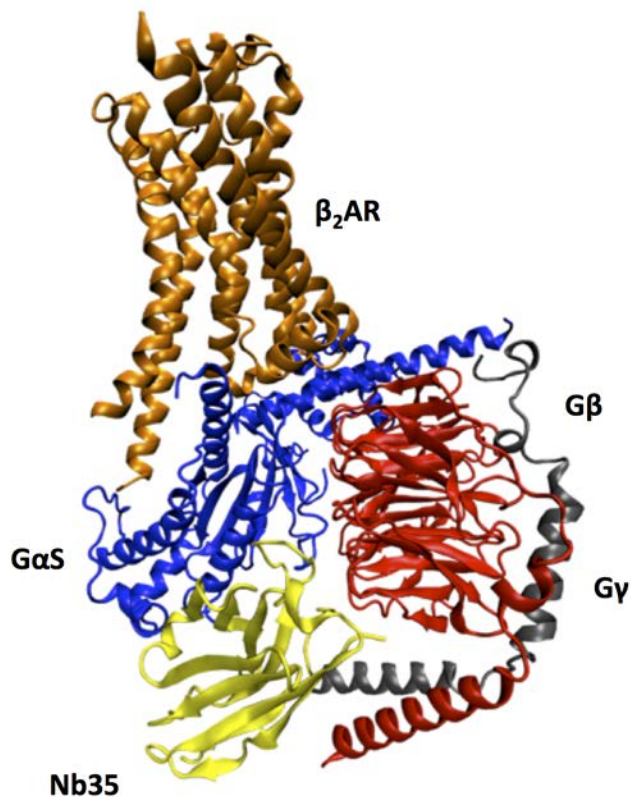
Figure 6. β_2AR bound to nucleotide free $G\alpha_S\beta\gamma$, stabilized by nanobody Nb35.

1.1.3.3 Parathyroid Hormone Receptor 1

The Parathyroid Hormone Receptor Type 1 (PTHR1) is a prototypical Family B GPCR with no full length structures yet solved. Applying the now routine approaches to obtaining crystals of GPCRs should provide a means to crystallize the PTHR1, a highly useful structure due to this protein's significant pharmacological relevance,

The PTHR1 binds Parathyroid Hormone (PTH), a key regulator of extracellular calcium and phosphate homeostasis, and is essential in the human body's management of bone healing and regeneration (71). When full length PTH (1-84) or its N-terminal fragment PTH (1-34) is administered intermediately to patients, bone density is increased, making it a useful

pharmacological agent for the treatment of osteoporosis (72). However, PTH administration is limited by the development of hypercalciuria in some patients. A high-resolution structure of the PTHR1 would serve to elucidate the working of this specific pharmacological target and also to expand our knowledge of GPCRs beyond the Rhodopsin-like class.

Major strides were made in understanding the structural-functional interactions of the PTHR with its ligand, PTH, in 2008 and 2010 with the publication of the extracellular domains structures of naïve and PTH bound PTHR1 (73, 74). However, with these publications came additional mysteries. For example, little was described regarding the interaction of the C-terminal region of PTH with the juxtamembrane domain of the receptor. The J domain, which includes the extracellular loops and ends of the seven transmembrane α-helices is crucial to PTH-PTHR1 activation (75-77). The J domain was not included in the construct used to resolve the ecto-domain structure, so the impact of PTH binding to these regions was not elucidated. Furthermore, the conformational shifts required to propagate PTH binding from the extracellular domain to the cytoplasmic domain could not be observed without the J domain, even if these loops were not essential for binding. Without a transmembrane version of the PTHR1 for structural studies, the function of the J Domain is impossible to extrapolate. Applying the well-established protein modification and crystallographic approaches for Family A GPCRs described here in 1.1.3 could provide a means to unravel the unknown structure-function behavior of the PTHR as well as further expanding knowledge of the Family B GPCRs.

1.2 STRUCTURAL BIOLOGY APPROACHES TO UTILIZING CRYSTALS FOR STRUCTURE DETERMINATION

1.2.1 Protein Crystals as the Backbone of High-Resolution Structures.

As proteins grow into a solid structure from purified protein in solution, a crystalline lattice made up of protein molecules in a specific and regular orientation, is constructed from the unit cell, or the fundamental unit of the crystal. The collection of symmetry operations that can generate the complete crystal lattice from the contents of the asymmetric unit is known as the space group. When crystals are grown to adequate size and quality they become useful for X-ray crystallography experiments. The electron clouds surrounding atoms in the crystal diffract X-rays according to Bragg's Law to produce a diffraction pattern. Analysis of the position and intensity of each diffracted wave (reflection), along with its phase, when the angle of the X-ray beam to the crystal is taken into account, can be used to obtain a map of the electron density within the crystal and, ultimately, a model of the protein structure that generated the diffraction pattern, provided sufficiently high resolution data are obtained.

There are several approaches to obtaining structural information from these well-ordered crystals. Classical, large crystal X-ray crystallography, which was used to solve the above-mentioned GPCRs, is currently the most commonly used approach to structural resolution of large proteins. However, there are two other methods that have been successfully applied to these difficult-to-obtain crystals. Nanocrystals of a GPCR have also been used to solve structures from X-FEL (78). Cryo-EM has also has been used to facilitate structure solution of bacteriorhodopsin by combining cryo-EM data with data obtained from crystals grown in the lipidic cubic phase

and analyzed by X-ray crystallography (79, 80). Each of these approaches provides different advantages and disadvantages for successful structural solution.

1.2.1.1 Identifying Conditions for Promoting Crystals Growth

The aim of crystallization methods is to obtain a slowly developing supersaturated protein solution such that protein nuclei are able to grow into large, well ordered, and usable crystals. To identify the conditions that promote supersaturation and stable crystal growth, crystallization trials aimed at systematically screening a myriad of conditions that include salt concentration and type, pH, temperature, cross-linking agents and chemical additives that will promote crystal growth are performed. Unfortunately, though a systematic approach to screening conditions is possible, the infinite combination of available selections requires human interpretation of subtle signs and symptoms of potentially favorable conditions.

There are many approaches that are commonly used to identify crystallization conditions for a given soluble protein. These same approaches are the initial starting point for the crystallization of detergent solubilized membrane proteins, though there are many other techniques available when those fail. The first line of attack to finding these conditions is to screen with commercially available kits. These screens provide pre-prepared concentrations and combinations of salts, pH, chemical additives, and different molecular weight PEG, to name a few. These matrix-screening approaches do not contain every possible crystallization condition, but they may give some clue as to the best approach for optimizing protein-specific crystallization conditions. The greatest utility of these commercially available screens is to enable rapid screening of a wide range of crystallization space with standardized and easily reproduced stock chemicals.

1.2.1.2 Methods for Optimization

The first stage of crystallization experiments aims to identify conditions that promote crystal nucleation and growth. However, in many, if not most cases, the initial conditions identified are not sufficient for the growth of high quality, large crystals. As a result, it is necessary to optimize crystallization conditions in order to grow the best possible crystals and thus maximize the diffraction by the crystals. The primary approach to optimization is to note all conditions that yield the initial crystal hit – salt type and concentration, pH, temperature, etc. as well as protein concentration. These hits refer to crystallization conditions that contain visible crystalline precipitate or large crystals. Then systematic and incremental modifications of these conditions must be made until changes in crystal growth can be identified, either in the positive or negative direction. Pursuit of those changes that favor increases in crystal quality and size is the first line approach to crystal optimization.

In some frustrating cases however, this approach does not rapidly yield helpful changes in crystal quality. In this case there are several other approaches that can be utilized. One is the use of libraries of highly concentrated additives that are used to supplement the initial (or optimized) crystallization condition hit. These additives impact crystal growth by changing protein solubility, modulating protein-protein interactions, and altering the thermodynamics of the precipitation process. One approach is to screen a small molecule library that is added to the crystallization condition being optimized. Detergent screening is performed in a similar manner and can be used to reduce non-specific aggregation that can limit crystal growth. Ionic liquids are organic salts that are highly soluble and can take part in ionic, hydrophobic and hydrogen bonding (81). These chaotropic liquids have been shown to reduce aggregation as well as enhance protein folding (82, 83). Ionic liquids can be screened as additives by the same method

mentioned above. In addition to studying the effects of these additives on crystal size and morphology, high throughput additive screening can also be coupled to the above mentioned (section 1.1.3.1) thermal shift assay. This approach will provide a quantitative means to compare the effect of the various additives on protein melting temperature.

Seeding is another long-standing optimization tool in the crystallographer's arsenal. This technique consists of three main approaches. Macroseeding traditionally refers to the process of transferring a small crystal or crystal fragment into a series of stabilizing wash solutions. After washing, the small crystal is transferred into a pre-equilibrated drop in order to grow the crystal larger (84, 85). Microseeding involves removing crystals from a drop, transferring them into a stabilizing solution, crushing them, and then creating various seed stocks by performing serial dilutions of the crushed crystal seeds (86, 87). Seed solutions are then introduced into new drops in the hope that the tiny crystal seeds will promote the growth of larger or more ordered crystals. In both instances the aim is to take microcrystals or fragments from large crystals and seed them into a metastable supersaturated protein drop to provide nucleation sites while controlling growth.

The third approach to seeding is microseed matrix screening (MMS), which is becoming a popular technique due to its adaptability to robot crystallization tray setup (88, 89). MMS is performed by first setting up traditional commercially available screens and then subsequently identifying crystals hits, likely of poor quality, to use as seeds. Low quality crystal hits are homogenized, pooled, and the resultant seeds are added to a new set of screening experiments, using the same screen from which the seeds were extracted. The challenge for this technique however is to adequately separate useful seeds from those that will have a deleterious effect on attempts to obtain higher quality crystals or are simply from a salt source that is indistinguishable

from protein. Furthermore, this technique has only been proven useful with visible crystals and does not utilize precipitates.

1.2.1.3 Special Considerations For Crystallizing GPCRs

The above-mentioned techniques can be used for crystallizing both soluble, membrane and multi-protein complexes. However, because of the unique difficulties in crystallizing large, seven transmembrane proteins, several different methods have been developed or expanded upon to crystallize these receptors. GPCRs can be crystallized from detergent (62). However, a far more effective technique for GPCR crystallization is crystallizing in lipidic cubic phase (LCP) (90). The development and application of this technique led to the first high-resolution structure of bacteriorhodopsin (91, 92). This viscous lipid solution forms a continuous bilayer in which protein can freely diffuse. The protein crystal nucleation sites that the three dimensional bilayer provides are fed by the freely diffusing protein (90). A similar technique that has been applied to GPCRs avoids some of the technical challenges of working with the viscous LCP medium is crystallization in bicelles (53). Bicelle crystallization provides a compromise between lipid and detergent by forming a lipid/amphiphile mixture, integrating detergent molecules into lipid bilayers (93). This technique provides several advantages including being amenable to different combinations of lipid types and detergent (94).

1.2.2 Methodological Approaches to Solving Structures from Protein Crystals

There are three main approaches to solving structures of ordered, three-dimensional crystals. X-ray crystallography is the most commonly applied and perhaps the most well-

developed approach to solving structures of proteins that can be coaxed into well-ordered crystals. A long-standing technique, this method requires, in most instances, micron sized crystals to solve structures. This field has contributed to the development of several areas of crystallography. It has provided a systematic approach to obtaining protein crystals described in previous sections, as well as establishing screening methods to identify cryoprotectants. The science of X-ray crystallography has also lead to the development of automated computerized techniques for translating a full data set into an electron density map suitable for building and refinement of high-resolution structural model. However, though X-ray crystallography is the primary approach to utilizing crystals, other techniques including X-ray free electron laser nanocrystallography and transmission electron microscopy can make use of crystals of much smaller size, thus overcoming some of the limitations of X-ray crystallography.

1.2.2.1 X-Ray Free Electron Laser Nanocrystallography

X-ray crystallography is a powerful tool to solve high-resolution structures of proteins; however, it comes with many disadvantages that limit its scope. The most apparent limitation is the unpredictable nature of finding conditions that yield large diffractable crystals. For many difficult targets, such as GPCRs, only microcrystals of these proteins can be obtained. The development of microfocused beamlines, however, have made it possible to solve structures from these smaller crystals (95). This development has been particularly essential for GPCR crystallography, as several notable GPCR structures could be solved solely using merged data sets from numerous microcrystals (96). In addition to being able to use smaller crystals that cannot be optimized to greater size and quality, collecting on microcrystals may provide benefits when twinning or mosaicity are a limiting factor (97). However, data collection on microcrystals

is not simple, and challenges such as high background and significant radiation damage may limit structure resolution (98).

However, the introduction of X-ray free electron lasers (X-FEL) overcame many of these challenges. X-FELs are up to ten times more brilliant than modern day synchrotrons (99). The diffract-before-destroy principle, applied at Linac Coherent Light Source's (LCLS) Coherent X-ray Imaging (CXI) beamline allows for the high energy XFEL to hit a single nanocrystal, under ideal conditions, to produce a single diffraction snapshot before the nanocrystal is destroyed. Theoretical and experimental results demonstrate that this diffract-before-destroy technique almost completely avoids radiation damage, solving the problems associated with collecting data on small crystals at a microfocus beamline (100).

The brilliant light source provided by LCLS yields opportunities for solving structures of challenging targets using small crystals. However, there were, and still are, many difficulties to be overcome in this field. The initial hurdle inherent to the diffract-before-destroy principle was sample delivery. Since only a single diffraction pattern could be collected per crystal, single crystals mounted on individual loops would not be practical for data collection. The first approach to overcome this challenge was a nanocrystal liquid injection system (101). This injection system directed a stream of nanocrystals of sufficient volume directly into the X-FEL beam, synchronized with the beam pulse.

Use of X-FEL technology provided a means to use nano and microcrystals too small for use even on a microfocused beamline or too vulnerable to radiation damage. Since many crystals, particularly GPCRs, have few crystal hits that can be optimized into large crystals appropriate for traditional X-ray crystallography, a new set of targets can now be studied. However this technique, though powerful for nano- and microcrystals, has only been applied to

samples that have previously been shown to grow to large sizes. Further investigation is necessary to develop techniques for identifying and testing nanocrystals that could not be optimized sufficiently for X-ray diffraction experiments by conventional synchrotron sources.

1.2.2.2 Electron Microscopy

Transmission electron microscopy (TEM) is a technique useful for obtaining structural details of biological macromolecules to a resolution of 0.1 to 0.2 nm. The TEM microscope is composed of a metal column under vacuum in which a linear beam of electrons is accelerated and focused by electromagnetic and electrostatic manipulation. Electrons are commonly generated by heating a tungsten filament, leading to evaporation of electrons from the filament. The voltage potential between the cathode emitter and the positively charged anode plate accelerates the electrons down the column. Electrons that pass through an aperture in the anode plate and the specimen are focused to form the image of the sample on a phosphorescent screen or CCD.

Examination of specimens by TEM has the advantage of requiring low concentrations of materials. In order to view samples such as protein or nanocrystals, these biological macromolecules must first be applied to a fine mesh grid, commonly made of copper with a carbon support film. These hydrophobic grids are glow discharged to make them hydrophilic before the sample is applied. To enhance the visualization of protein samples, a heavy metal salt such as uranyl acetate is used to stain sample-containing grids. The uranyl acetate will occupy hydrated regions in and around the protein sample, only staining the background and leaving protein looking white and unstained. A modified TEM approach, cryo-TEM, allows for the study of samples without the use of staining, dehydration, and fixation that the sample undergoes during negative stain TEM. Cryo-TEM samples are rapidly frozen to cryogenic temperatures

24

where water can exist in a vitrified state, keeping the sample hydrated. This allows for viewing of samples in a more native-like environment than traditional negative staining.

In addition to the visualization of samples, TEM provides a means to perform electron diffraction experiments to solve structures utilizing crystals much like X-ray crystallography. Cryo-TEM makes use of nanocrystals to solve structures by utilizing the advantages that electrons provide over X-rays. The advantage of electron diffraction for thin specimens over X-rays is that the damage per elastic event for X-rays is more than one hundred times greater than for electron diffraction, allowing for more data to be collected before the crystal is made unusable by radiation damage (102). Initially, this allowed for the resolution of structures using TEM initially performed on 2D crystals (103, 104). However, an extensive number of crystals must be used to provide sufficient data in order to solve structures. These large volumes are required because of the significant radiation damage that the crystal undergoes which only allows for a single diffraction pattern to be obtained per crystal (105). In response to these challenges there have been recent methodological advances that utilize a significantly lower quantity of 3D crystals for solving structures (106, 107). The new technique relies on using a particularly low electron dose to prevent radiation damage to 3D crystals, overcoming the challenges associated with 2D crystal data collection. This provides a means to use a much smaller volume of crystals for solving structures than was previously possible (107). This method has been demonstrated in a recent paper using lysozyme nanocrystals as a model system (107). Use of 3D crystals in diffraction experiments necessitated thin preparations of lysozyme crystals where only crystals between a thickness of 0.5-1 µm and 1-6 µm long were usable for data collection. Electron diffraction was used to collect data on these crystals using a tilt-series

that allowed for the collection of 90 different diffraction patterns per single crystal. Collecting in low dose mode enhanced the data set collected for a single crystal, minimizing radiation damage.

Although this technique expands the possibilities for solving structures from nanocrystals by cryo-TEM, it has yet to be used for proteins for which larger crystals could not be obtained or for proteins that require nanocrystal optimization in order to get the best possible diffraction data. Furthermore, as demonstrated in the recent tilt-series paper using lysozyme, growing and then subsequently identifying nanocrystals of ideal size can be difficult, requiring further work to make this approach more applicable to other protein nanocrystals.

1.3 CONCLUDING REMARKS

There are powerful tools available to structural biologists for solving structures of large, challenging targets. These tools include well-established, robust techniques, such as X-ray crystallography, as well as newer strategies such as X-FEL nanocrystallography. A group of targets that have long been considered classic examples of difficult targets are the GPCRs. Though 19 unique structures have been solved for the largest of the GPCR families, little is known of how to solve and resolve structural features of other GPCR families. It is expected that the classical protein modification and crystallography techniques developed for obtaining crystals and solving Family A GPCRs will be readily applicable to other families. However, given the low sequence homology amongst GPCR families, this may not be a foolproof way to obtain structures. The PTHR1 is an example of such a challenging target whose structure would elucidate a significant pharmacological target, highly useful for osteoporosis interventions. Family A protein modifications and crystallography optimization tools will be the first line of

attack applied in the work presented here to obtain usable crystals of the PTHR1. However, since the inherent difficulties of working with GPCRs are further complicated by the PTHR1 not being a member of Family A, other methods for growing, identifying, optimizing and utilizing crystals will be employed. In addition to the pharmacological significance that this target represents, it is also an ideal candidate for developing methods applicable to other previously unsolvable challenging targets. This work strives to compare and utilize X-ray crystallographic, TEM and nanocrystallography techniques for obtaining crystals of difficult targets using the PTHR1 as a suitably challenging test case.

1.4   AIM AND HYPOTHESIS

<u>**Central Hypothesis**</u>:

Protein nanocrystals can be identified in a variety of protein targets intended for crystallization experiments, including samples of soluble, membrane and multiprotein complexes.

Specific Aim 1:

Perform crystallization trials of the PTHR1 using previously established Family A GPCR strategies

Specific Aim 2:

Identify protein nanocrystals of PTHR1 and other challenging targets by TEM

Specific Aim 3:

Use TEM to evaluate the consequences of the X-FEL Gas Dynamic Virtual Nozzle injector on nanocrystals morphology

Specific Aim 4:

Compare the crystal optimization potential of conventional seeds to TEM visualized "nanoseeds"

2.0   PTHR1 CRYSTALLIZATION TRIALS

2.1   INTRODUCTION

Structural biologists have made exciting progress in the understanding of the structure and function of Family A GPCRs. This progress is mainly due to the ever-expanding catalogue of unique GPCR crystal structures as well as the recently solved multiple conformations of β_2AR. However, much is still unknown about the Family B GPCRs as a result of the lack of high-resolution structures. This challenge has only recently been overcome with the crystal structures of the glucagon and corticotrophin-releasing factor receptor 1 (108, 109). The recent crystal structures were not full-length constructs and were truncated to exclude their large N-terminal domains. The lack of information is significant, as some of the most important differences between GPCR families are traced to the variations in the type of extracellular domains that are found in the N-terminus.

Many of the soluble ECD domains of the Family B GPCRs have been crystallized individually (73, 74, 110-112). For example, the prototypical member of the Family B GPCRs, the parathyroid hormone receptor type 1 (PTHR1) is illustrated in **Figure 7** with the bound parathyroid hormone (PTH).   As seen in this figure, the parathyroid hormone (PTH) is sandwiched between the N-terminal helix and the C-terminal β-sheet of the PTHR1 extracellular domain (ECD). A comparison of the ligand bound (**Figure 7A**) and naive ECDs (**Figure 7B**)

suggest that when the ECD is without ligand, it dimerizes with itself. However, *in vivo* assays have yet to support this result and demonstrate the biological relevance of the dimerization. Further understanding of the PTHR1, *in vivo*, would be valuable in determining useful crystallographic approaches to solving the structure of full length PTHR1.
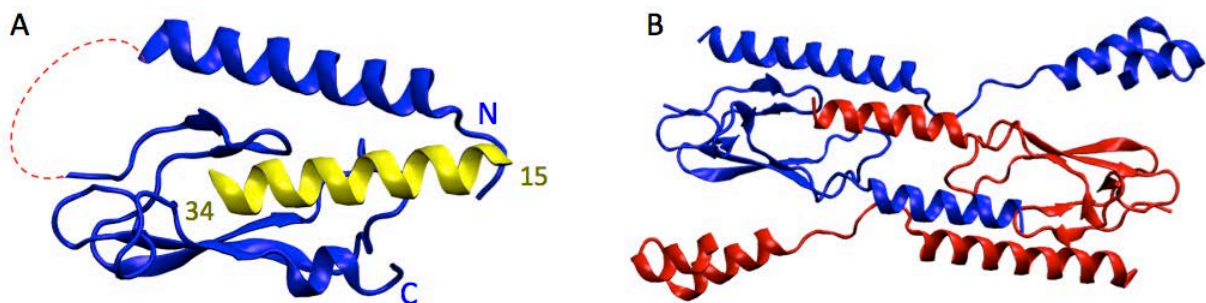
Figure 7. Crystallized extracellular domains of the PTHR1

A) Monomeric ligand bound ECD versus B) the apparent dimeric ECD structure without ligand.

As illustrated in **Figure 8**, the PTHR1 contains many of the same flexible domains that interfere with crystallization in the Family A GPCRs as illustrated with a predicted disorder plot of β_2AR. More disordered regions, with a greater degree of disorder, are predicted for the PTHR1 compared to the β_2AR. Specifically, both the N-term and C-term of the PTHR1 are longer and have greater disorder. One could presume, however, that similar regions of instability (e.g. the third intracellular loop (ICL3) and C-term tail), would be amenable to the same crystallographic strategy that has been successful for the Family A receptors.
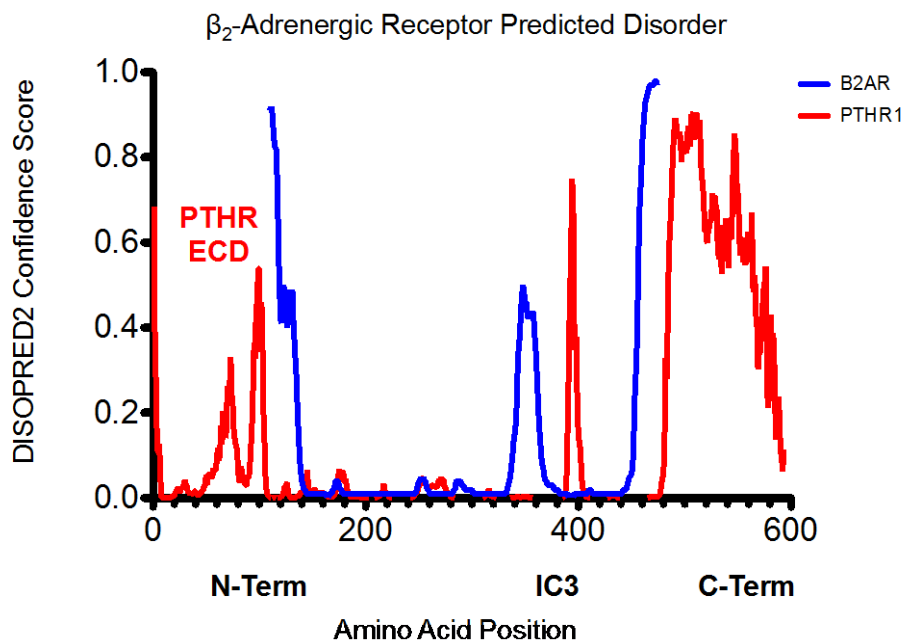
Figure 8. Predicted disorder of the PTHR1 versus β_2AR generated by DISOPRED2

In addition to the hurdles presented by stabilizing the numerous disordered regions of the receptor, the requirements unique to successful membrane protein crystallization also provide formidable challenges. This requires careful screening of conditions that best stabilize the extraction and monodispersity of a purified membrane receptor. Furthermore, these conditions need to be optimized to allow for maintaining the functional activity of the protein outside of its natural environment--the conditions of which may not be ideal for solubilization.

The aim of this work was to test the applicability of the successful Family A GPCR protein modifications and crystallization approaches to obtaining crystals of the PTHR1. Given the lack of full-length structures of the Family B GPCRs, crystallization constructs with the ECD were used for these trials. Furthermore, structural knowledge of the receptor, provided by the ECD structures with and without ligand, illustrates the presence of crystallization-adverse

flexible portions of the soluble ECD component of the receptor. This information was also used to guide the design of constructs.

2.2   RESULTS

2.2.1   Development of a Protein Purification Protocol for the PTHR1

An *E. coli* expression system was chosen for the PTHR1 due to its high yield, ease of expression of PTHR1 mutants and the comparative lack of post-translational modifications, which confer crystallographic complications. Since receptor glycosylation has been demonstrated to be unnecessary for ligand binding (113), post-translational modifications were deemed unnecessary. The human PTHR1 was cloned into a pET21a vector with a C-terminal 10xHis tag.

A 96 detergent dot blot screen (Hampton Research) was performed which included ionic, non-ionic and zwitterionic dispersing agents in order to extract the maximum amount of recombinant protein from the *E.coli* expression system. To perform this screen, the PTHR1 was expressed in large scale. Isolated cells were lysed by sonication and aliquoted into 0.5 mL fractions. The insoluble membrane pellet was isolated by centrifugation and each fraction was homogenized with a member of the detergent screen, excluding controls, at approximately 2.5 times the critical micelle concentration (CMC). Solubilized fractions were applied using a dot blot apparatus to a nitrocellulose membrane. The membrane was blotted with an anti-His probe. Promising solubilizing agents resulted in dense signals in the dot blot as shown in **Figure 9**. The darkest dots indicate well-extracted protein, while the bottom right dots mark the controls, with

barely any visible extracted protein. This assay indicated that a combination of Sarcosine and Fos-choline 14 were the best solubilization agents for the PTHR1.
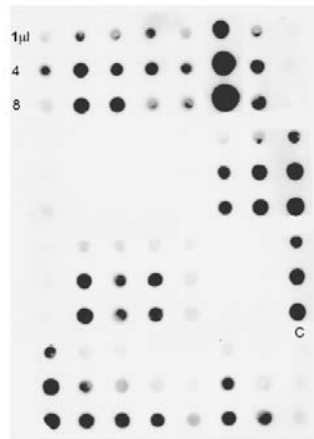
Figure 9. Nitrocellulose membrane exposed to PTHR1 extraction samples using a dot blot apparatus, probed with anti-His

To determine the most appropriate agent combination and concentration to promote a monodisperse sample, dynamic light scattering (DLS) experiments were performed. As illustrated in **Figure 10**, submicromolar concentration of Fos-choline 14 resulted primarily in a one species decay. Following these small-scale experiments, large-scale purification the PTHR1-His was performed using a Ni-affinity chromatography, followed by a desalting column to remove imidazole. Purification yielded 1.5 mg purified protein per 1 L of cells as shown in **Figure 11**.
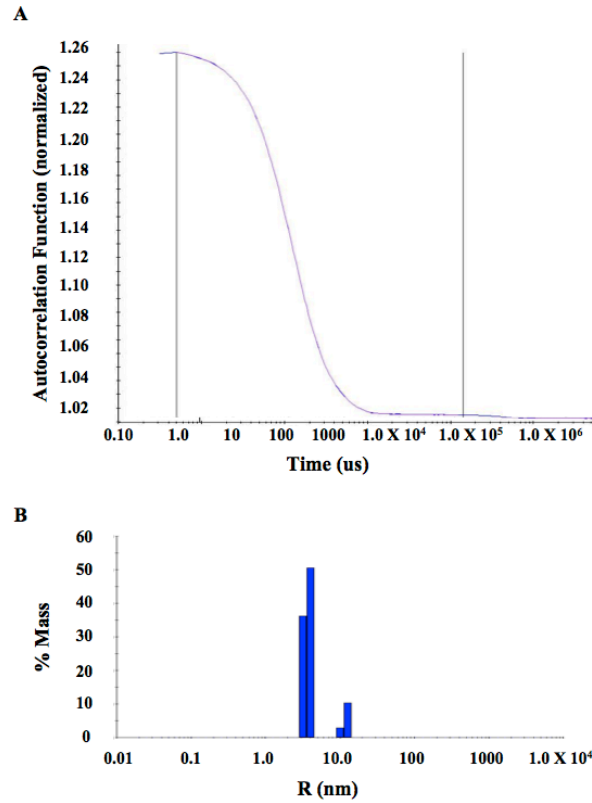
Figure 10. Autocorrelation function versus time of purified PTHR1 shows primarily one species

decay
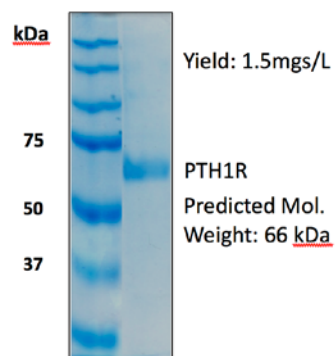
Figure 11. Purified PTHR1 with a predicted molecular weight of 66 kDas stained with Bradford

2.2.2 Interaction of purified PTHR with PTH 1-34 and G_S

To test the functional activity of purified PTHR1, the receptor's ability to interact both with its extracellular ligand and with its intracellular binding protein was investigated. To determine if purified protein was able to bind to both ligand and to its intracellular binding partner, $G\alpha_S\beta\gamma$, on-column binding experiments were performed. As illustrated in **Figure 12A,** a biotinylated PTH 1-34 analog was incubated with receptor and subsequently mixed with streptavidin beads. As shown in **Figure 12B**, the PTHR1 is able to bind to bio-PTH 1-34 and be retained on the beads, while PTHR1 not incubated with bio-PTH 1-34 was not retained.
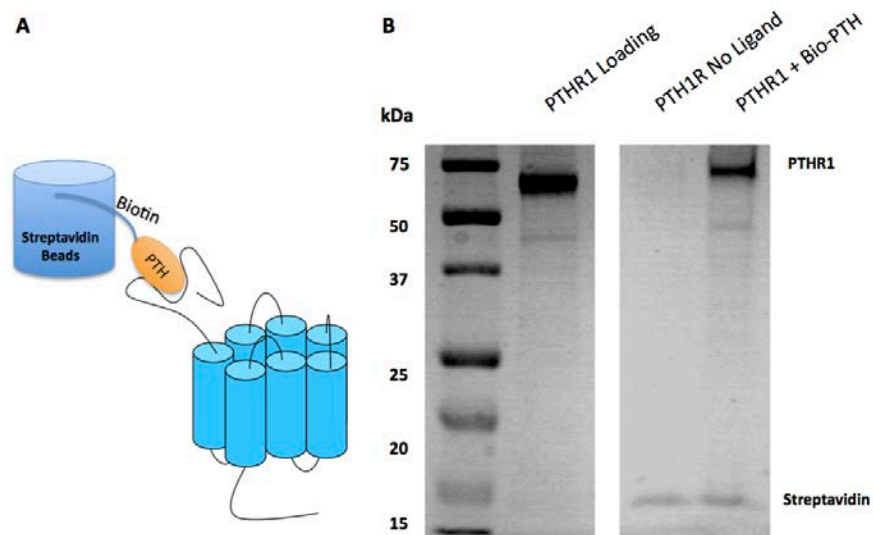
Figure 12. PTHR1 binding to biotinylated PTH 1-34

The second on-column experiment tested the ability of purified receptor, bound to PTH 1-34, to interact with its intracellular binding partner $G\alpha_S\beta\gamma$. His-PTHR1 was incubated with untagged $G\alpha_S\beta\gamma$ and passed over a Ni-resin column. As shown in **Figure 13A,** the PTHR1 receptor is retained, along with $G\alpha_S$, while very little $G\beta\gamma$ is still present ($G\gamma$ is not visible due to its small size). $G\beta\gamma$ washed out, as visible in the flow through lane. A model of this interaction is shown in **Figure 13B.** This model is very similar to that observed in the recently resolved β_2AR-

Gα complex structure (45). This structure shows that in the presence of ligand, the only crystal contacts with G_S are with $G\alpha_S$, while none are observed with $G\beta\gamma$. These on-column experiments show an interaction between purified receptor and extracellular ligand as well as with the intracellular binding partner, $G\alpha_S$. After optimization, these binding interactions were not inhibited by the detergent type or concentration used for solubilization of the receptor.
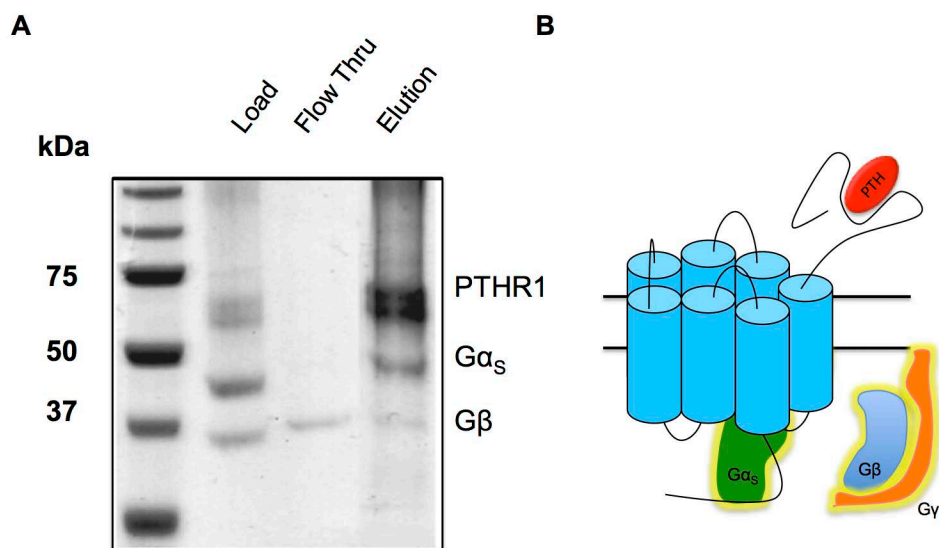
Figure 13. On column PTHR1-G_S binding experiments

His-Tagged PTHR1, $G\alpha_S\beta\gamma$ and PTH 1-34 were incubated together, shown in the "Load" lane. The "Load" was applied to a Ni-affinity column and "Flow thru" collected. The PTH 1-34-PTHR1-Gs complex was then eluted with imidazole

2.2.3   Crystallization Trials with Wild-Type PTHR1

Crystallization trials were performed with the purified, solubilized receptor. As described in section 1.1.3.2, the presence or absence of ligand has significant effects on the crystallization strategies required to obtain the Family A GPCR crystals. Therefore, crystallization trials of the PTHR1 were performed with PTH 1-34 and with PTH 1-15, the most readily available antagonist of the PTHR, as well as trials with no ligand present.

Crystallization experiments of the monodispersed receptor in the presence and absence of ligands were first approached using traditional, commercially available kits. Screens were obtained from a variety of manufactures including Hampton Research, Molecular Dimensions and Emerald Bio. These screening experiments were performed at 4°C, 16°C, 25°C. No visible hits were detected. Drops containing useful protein aggregates were identified by UV tryptophan fluorescence microscopy. Up to one third of drops screened had fluorescence.

Several different optimization strategies were pursued for the purpose of transforming UV positive precipitates into visible microcrystals. As a first step, conditions that yielded useful precipitates of wild type PTHR were set up using increments of the modified component of the crystallography experiment that were slightly (or dramatically) changed. For example, the concentrations, pHs, PEG types and temperature were modified. None of these efforts resulted in useful, visible crystals. Lipidic cubic phase (LCP) trials with crystallography screens specifically compatible with LCP were used in testing. Moline LCP and well as Moline + cholesterol LCP were setup for the receptor with and without ligands. Bicelle crystallization with different lipid combinations were also tested. Furthermore, 'in gel' agarose experiments were performed using the same commercially available screens employed in the original PTHR1 screening.

In addition to these efforts, modifications of seeding protocols were also performed using drops containing granular aggregates that were positive for UV tryptophan fluorescence (rather than the traditional use of low quality visible crystals). These experiments include collecting UV positive aggregates and performing streak microseeding and MMS experiments. A type of cross seeding was also applied, in which PTH 1-34 crystals were seeded into crystallography

experiments. Despite these attempts at crystallizing the full length PTHR, the receptor was not amenable to crystallization efforts in its native form.

Name	Mutation	Differences Compared to WT
PTHR-ProA	ProteinA inserted at end of C-term	None
480s (PTHR480S)	Stop inserted at AA 480, removing residues 480-565 of C-term tail	None
IC3D	No Ecto mutations, IC3L removed and replaced with 8SG linker	None
KC (KPTHR-480S)	Residues 52-104 replaced with 8 Ser-Gly Linker	Increase solubility and degradation resistance
Ki (KICL3D480S)	Residues 52-104 replaced with 8 Ser-Gly linker + IC3L removed and replaced with 8SG linker	Maintained features of KC
NoEctoPTHR	Removed residues 29 –187	Low expression, no cleavage
NoEctoICL3DSGPTHR	Removed Ecto domain and Mutated 3rd ICL	Low expression
Bloomstrand	Constitutively inactive mutation	None
Jansen's	Constitutively active mutation	None

Table 2. PTHR1 crystallography mutants

As a result of the lack of success with crystallization trials, crystallographic protein modifications, in line with those that have been successful with the Family A GPCRs, were tested. The goal was to create truncation fragments that reduced the effect of disordered regions in the PTHR. Table 2 summarizes the protein modifications that were applied to the PTHR1. The most nascent modification was to remove the flexible C-term tail to amino acid 480, a modification that retains the functional activity of the receptor. This modification was combined with replacement of the ICL3 flexible domain with a rigid Ser-Gly linker. A similar technique was used to stabilize the ICL3 of the turkey β_1AR construct used for crystallization of the

receptor (61). Crystallization trials with these modified proteins did not provide useful crystal hits, and no improvements were observed over time in crystal trays.

One potential source of the continued inability to obtain hits was the possible negative contribution of the large ECD of the receptor. The crystal structures of the ECD clearly show a 45 amino acid flexible loop, which though included in the construct, could not be resolved in either structure (**Figure 14A).** To mediate the impact of this loop on the crystallization trials, it was removed and replaced with a rigid serine glycine linker modeled to maintain the distance between the α-helix and β-sheet. These modified ECD constructs (referred to as K truncation mutants) were made with full-length C-term tail, 480 stop and 480 stop + ICL3D. Interestingly, despite a significant modification to the ECD region, the application of ligand to pure K-PTHR1 still resulted in the typical disruption of oligomerization previously observed in the ECD crystal structures (**Figure 15**) (74, 114). However, as in previous trials, no significant changes in crystalline hit number or quality were noted.

Green: 45 AA flexible loop, unresolved in crystal structure

Red: Artificial stabilizing Ser-Gly linker inserted to replace 45 AA loop

PDB ID: 3H3G
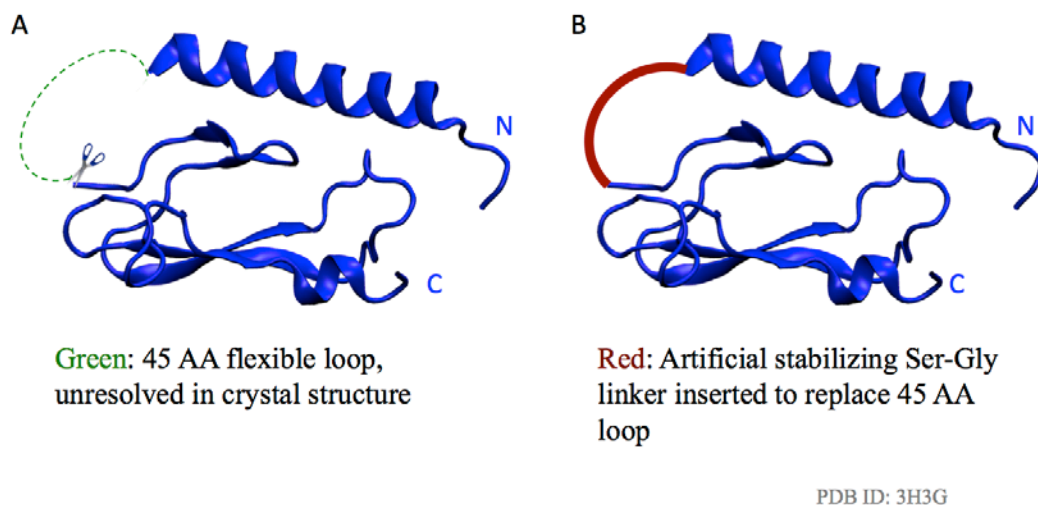
Figure 14. The PTHR1 extracellular domain structure, which reveals a 45 AA, disordered loop, replaced in tested crystallization constructs with a 8 AA stabilizing Ser-Gly linker

Other truncations were performed, such as complete removal of the ECD of the receptor and point mutations to obtain constitutively inactive and active PTHR1 mutations. Problems, however, such as low expression for crystallization trials or rapid protein degradation made such mutants unsuitable for crystallization trials. As a result, on the 480s, ICL3D and K mutants (as well as combinations of these truncations together) were tested.
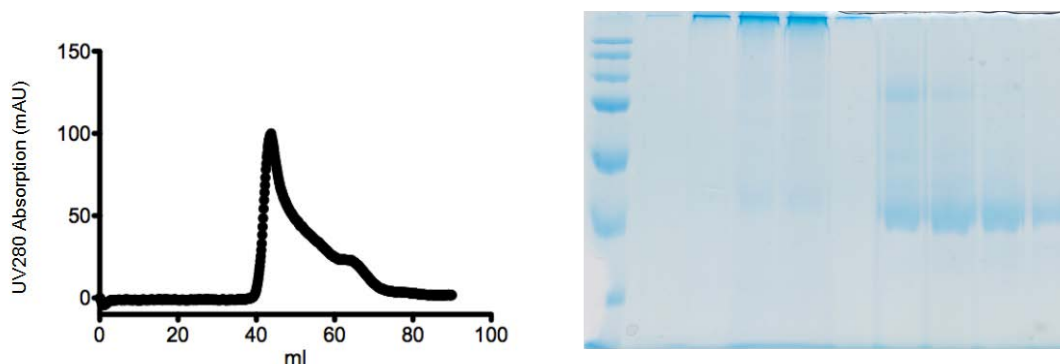
Figure 15. Effect of PTH (15-34) on KPTHR480S aggregation

Though the initial aim of this work was to obtain visible crystals of the PTHR1, the lack of positive effect of the previously successful GPCR crystallization modifications was curious. The contribution of these mutations to the overarching stability of the truncation mutant melting temperature (T_m) was evaluated by Microscale CPM Assays. This assay, described in section 1.1.3.1, relies on CPM, a fluorescent dye that is quenched in aqueous solution but fluoresces when bound to exposed cysteine residues. This dye can be used to screen the consequence of mutations on the melting temperature of the protein using a temperature gradient to identify the temperature at which the receptor unfolds, as indicated by an increase in fluorescence.

The first investigation using this Thermofluor assay was carried out with full length PTHR1 to compare the stability of the receptor in the presence and absence of ligand across

variations in pH typically present in crystallization experiments. As indicated in **Figure 16**, PTH 1-34 decreased melting temperature only slightly and did not modify the overall trend of PTHR1 stability over increasing pH. This correlates with the lack of observable improvement in crystal hits in initial screening with wild-type PTHR.
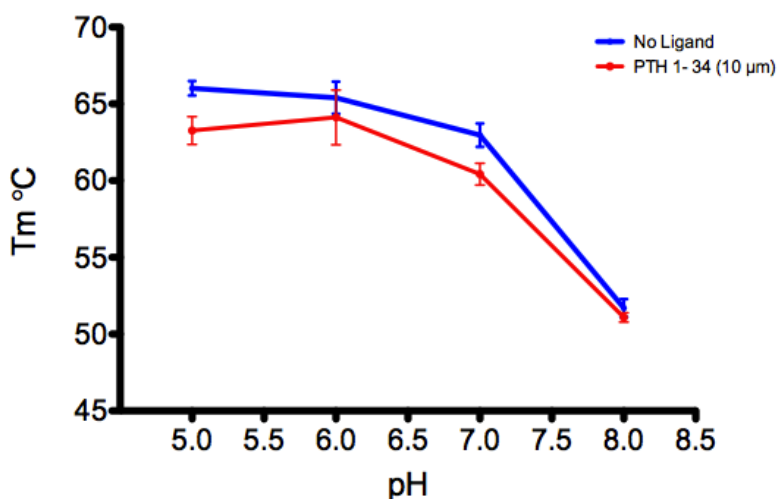
Figure 16. Melting temperature of full length PTHR1 when exposed to increasing pH

The Microscale CPM Assay was subsequently used to compare the PTHR1 constructs used for crystallography trials. As demonstrated in **Figure 17** the basic modifications that focused on the obvious disordered regions of the PTHR1 had surprisingly deleterious results, with only an insignificant increase in T_m by the ICL3 deletion construct. The effect of ligands on the T_m of the truncation mutants was also examined. Both agonist and antagonist were able to increase the T_m up to 7°C. However, even the ICL3 deletion construct with its increase in T_m gained by antagonist fell short of that conferred to full length PTHR1.
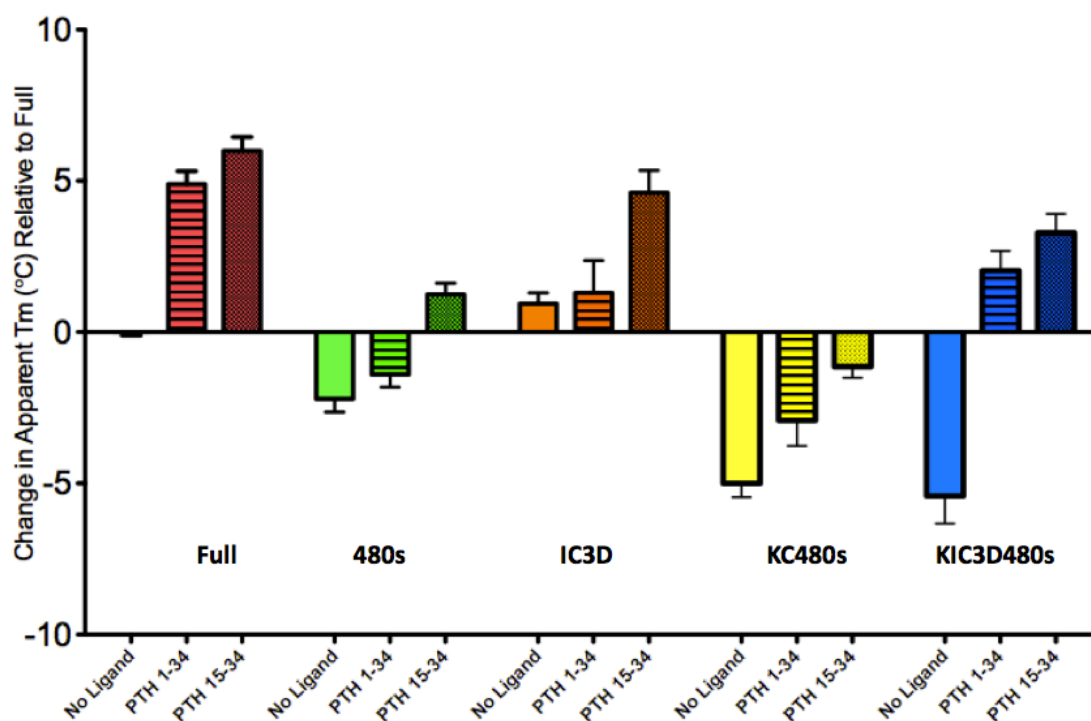
Figure 17. Change in relative T_m of PTHR1 mutants compared to full length in the presence of agonist, antagonist and in the absence of ligand.

2.3   DISCUSSION

A high yield of monodispersed PTHR1 was expressed and isolated from *E. coli*. The purified, recombinant protein was able to bind ligand as well as its intracellular binding partner, providing an excellent starting point for crystallization trials. $G\alpha_S\beta\gamma$ binding experiments showed interesting similarities to the binding interactions observed in the recently solved β_2AR-Gs complex (45). This structure showed that the only contacts between the receptor and Gs were with the $G\alpha$ subunit. Similarly, purified His-tagged PTHR1 retained, almost exclusively $G\alpha_S$

while Gβ was shown to dissociate from the complex and wash out in the flow through (**Figure 13).**

Crystallization trays of PTHR1 were set up with and without agonist and antagonist. These initial trials, at best, only produced UV positive granular aggregates with no visible crystal hits—an anticipated result given the difficulties associated with crystallizing GPCRs. Truncation mutants of the PTHR were cloned and purified in order to remove the predicted disordered regions. The results of both crystallography experiments and Microscale CPM experiments suggest that, unlike the Family A GPCRs, the PTHR1 melting temperature is actually reduced by the typical truncation approaches that were successful in the crystallization of previous GPCR structures.

There are several possibilities as to why removing the disordered regions of the receptor contributed to a reduction in melting temperatures. The first major modification was to the ECD, where the flexible loop of the ECD was removed and replaced by a rigid linker that was modeled to maintain the distance between the β-sheets and α-helix. This was the most deleterious of the truncations constructs (removing 45 number of amino acids), even though it displayed the same monomer/dimer behavior in the presence and absence of antagonist as the constructs used to successfully crystallize the PTHR1 ECD. Furthermore, PTH 1-34 and 15-34 both increased the melting temperature towards that of the full-length construct. It is of course possible that for unforeseen reasons, the removal of this loop actually increased the disorder of the ECD. The two-step model of PTH interaction with receptor may provide an explanation for how this disorder may have been alleviated by ligands (77). In this model the PTH 15-34 C-term segment interacts with the binding pocket of the ECD while the N-term portion (PTH 1-14) of the ligand interacts directly with the juxtamembrane region (J domain) of the receptor, comprised its

43

extracellular loops. Perhaps the disorder introduced by the removal of the ECD loop was partially stabilized by the ligand if the ligand could act to facilitate the interaction of the ECD with the body of the TMD.

Amongst all GPCRs solved to date, overcoming the challenges of intrinsic basal activity that are inherent to these receptors, required the use of specially engineered antagonists that forced the GPCR into a lower energy, inactive conformation. Crystallization of these receptors with agonists was impossible without other interventions such as nanobody stabilization of the active state of the receptor (44). However, in the case of the PTHR1, it was surprising to consider that both agonist and antagonist had similar effects on melting temperatures, and in both instances, the result was an increase melting temperature. It is possible that this similar effect on receptor stability, observed across all the truncation constructs tested, maybe a result of the two-step ligand binding model, which closes the ECD towards the receptor. No matter the contributing factors, this discovery may give tentative hope that PTHR1 may be more amenable to crystallization of both inactive and active conformation than previously encountered by GPCR crystallographers.

Given the lack of Family B crystal structures at the time of this work the truncation protein modifications used for this study followed the approaches that had been successful for the Family A GPCRs. However, all but one truncation construct, with a T_m change less than 1°C, lowered melting temperatures compared to full length PTHR1. This was quite unexpected given that the truncation of the C-term tail, for example, is a common necessity in Family A crystallization. Given these results, it is not surprising that the two recently solved Family B GPCRs show a significantly different approach to crystallizing these receptors than was used for the Family As. For example, in both the glucagon receptor (GCGR) and corticotropin releasing

factor receptor (CRHR1) efforts towards stabilizing intracellular loops were focused on the ICL2 and not on the ICL3 (108, 109). Furthermore, as the recently solved structures of GCGR and CRHR1 receptors indicate, there are momentous variations between structures within the Family Bs. Though the GCGR had the same basic 7 transmembrane α-helix domain orientation of the Family As, the CRHR1 has a distinct V shape orientation not observed for other GPCR structures. It was hypothesized that the open orientation of the extracellular facing side of the receptor accommodates its peptide ligands (109). The differing behavior of the PTHR1 upon the application of the Family A GPCR crystallization recipe may suggest that the PTHR1, like the GCGR and CRHR1, emulates the same variation that exemplifies the structural differences within this family as well as between the other families of GPCRs.

Given the newly available information provided by the GCGR and CRHR1 structures, the course of further crystallization experiments with the PTHR1 could be modified to include the successful approaches used for these Family B members. One example would be focusing on stabilizing the ICL2 rather than the ICL3 as was done in these two structures. Additionally, screening of large fusion proteins to the ECD domain of the receptor (or to a receptor with the ECD completely removed) could provide a means to obtain crystals. However, such an approach is not trivial and requires screening of large libraries of fusion proteins, as was the case in the GCGR. Another consideration brought to light by these new structures is the differences in the C-terminal truncations required for crystallization of CGCGR and CRHR1. Both truncated the C-terminal tail, but in the case of GCGR, the putative α-helix 8 was retained while CGCGR crystallization required complete removal of this helix. The C-terminal truncated PTHR1 constructs used in this study were truncated at residue 480, allowing for the inclusion of helix 8

(contained within residues 465-474). Deletion of this helix, given that it required complete removal in the case of CGCGR, may be another useful strategy for crystallization of the PTHR1.

Though visible crystal hits were not observed during PTHR1 crystallization, the receptor provided an abundance of UV positive granular aggregates. Such aggregates may be ideal candidates for nanocrystallography trials, if a way was devised to distinguish between granular aggregates that contained nanocrystals suitable for further optimization and X-FEL diffraction versus unusable amorphous protein aggregates. If such evaluation were possible, an alternative approach to solving structures of GPCRs, perhaps even one that would require less truncation of the receptor, would be a powerful crystallographic tool for resolving structures of challenging targets such as the PTHR1.

2.4   METHODS

2.4.1   PTHR1 Cloning and Expression

The full-length human PTHR1 sequence was amplified and subcloned into a modified pET21 bacterial expression vector (EMD Biosciences) with a N-terminal 10x His tag using EcoR1 and XhoI restriction sites. Truncation of the C-terminal PTHR tail was performed by inserting a stop codon into the sequence at residue 480. Site directed mutagenesis for the Jansen's metaphyseal chondrodysplasia, and chondrodysplasia Blomstrand type mutations was directed at H223R and P132L respectively, and performed per manufactures instructions with a QuikChange II Site-Directed Mutagenesis Kit. (Agilent Technologies). Round the Horn PCR was performed both to replace the ICL3 (residues 389-401) with a 8 residue rigid Ser-Gly linker as well as to do the

same so as to create the K construct, which replaced the extracellular domain flexible loop (59-105) with the rigid linker. N-Terminal MBP constructs were generated by inserting amplified PTHR1 into a MBP pET41 vector using EcoRI and XhoI restriction sites.

2.4.2   Dot Blot Detergent Screening

To determine ideal solubilization conditions for the PTHR1, dot blot detergent screening was performed. Bacterial lysates were obtained after brief sonication, cell lysates were aliquoted in 100 fractions containing 100 μL of cell lysate each, and spun down for 30 min. After centrifugation, the supernatant was removed and each pellet containing the insoluble target protein was re-suspended in 75 μL of buffer A plus 25 μL from each detergent in the 96-well format Hampton Research (HR) screen, leaving four control samples for re-suspension with buffer only. Since most detergents in the screen were 10□x CMC (for each detergent), aliquot detergent concentration was approximately 2.5 x CMC. Samples are incubated for 20 min at 4°C. After the detergent incubation period, detergent solubilized samples were centrifuged at 17,000 RCF for 30 min and the supernatants loaded on a dot blot apparatus for quantification using a His-tag. Three different volumes of sample are loaded 1, 4 and 8 μL. Analysis of the dot blot western provided the means to identify the best extracting detergent candidates compared to the control, ''buffer only'' aliquot.

2.4.3   Identifying Conditions for a Monodispersed PTHR1 Sample

After the best extracting agents had been identified the next step was to determine if the receptor was monodispersed in these detergents, and if so in what concentration. To determine

47

this dynamic light scattering (DLS) experiments were performed. Purified PTHR1 at a concentration 4 mg/mL was spun down at 17,000 RCF before being loaded into a 384-well Corning plate and analyzed in batch mode using a Wyatt DynaPro Plate Reader in the presences of different detergents in varying concentrations. 0.75 mM Fos-Choline 14 was found to facilitate the greatest monodispersity of the receptor.

2.4.4 Purification of PTHR1 and its Truncation Fragments

A single colony was used to inoculate TB medium containing 100 μg/ml ampicillin grown at 37°C until an OD_{600} of 1.0 was reached. Cells were then cooled to 25°C for 30 mins and induced with 125 μM isopropyl-β-D-thiogalactopyranoside (IPTG). Cells were harvested after 16 hrs, flash frozen in liquid N_2 and stored at -80°C.

All purification steps were performed rapidly at 4°C to prevent proteolysis. Cell pellets were homogenized in buffer A consisting of 150 mM NaCl, 25 mM Tris pH 8.0, and 1 X Protease Inhibitor Cocktail (10 μg/ml pepstatin, leupeptin, chymostatin) plus 100 μM phenylmethylsulfofluoride (PMSF) and 0.5 mM ethylenediaminetetraacetic acid (EDTA). Lysis was performed by sonication (Sonicator 3000, Misonix), power 7.5, 4 secs on 8 secs off for 6 mins total time. Lysate was cleared by centrifuged at 5,000 RCF for 15 mins. The membrane fraction was isolated by centrifugation at 100,000 RCF for 30 mins. Membrane pellets were extracted in 25 mM Sarcosine, 5 mM Fos-choline 14 for 2 hrs before being spun down at 100,000 RCF for 30 mins.

Supernatant was loaded at 0.1 mL/min onto 4 mLs of His-Select Fast Flow Resin (Sigma). Detergent exchanged was performed from 25 mM Sarcosine, 5 mM Fos-choline 14 to

0.75 mM Fos-choline 14. Resin was washed in stepwise gradients with 15 column volumes of

buffer A + 25, 40 and 60 mM imidazole and eluted with 90 mM imidazole in buffer A. Elutant

was pooled and loaded onto a HiPrep 26/10 desalting column (GE healthcare). Purified PTHR1

was incubated for 30 mins with PTH 1-34 or 15-34 monomer species was isolated from

oligomerized PTHR1 by separation with a Supderdex 200 16/60.

2.4.5   PTHR1 Interaction with Biotinylated-PTH 1-34

PTHR1 in PTHR1 buffer was incubated with and without 100 uM of N-terminally

labeled Biotinylated PTH 1-34 for 1 hr at 18°C. Samples were subsequently incubated with High

Capacity Streptavidin agarose beads (Thermo Sci). Sample with beads were loaded into empty

spin columns (Bio-Rad) and washed with PTHR1 buffer five times. Beads were boiled and

analyzed by SDS-PAGE gel.

2.4.6 $G\alpha_S\beta\gamma$ Purification

Sf9 cells were co-infected with a $G\alpha_S$ construct containing a C-terminal 10x His tag preceded by

a TEV cleavage site and a $G\beta_1$ $G\gamma_2$ construct via baculovirus. Harvested cells were diluted with

buffer A (250 mM KCl, 30 mM Hepes pH 7.5, 5 mM $MgCl_2$, 2x P.I.) with 0.6 mM $C_{12}E_8$. Cells

were lysed by sonication, power 3, 10 secs on, 45 secs off for 1.20 min total time. Lysate was

further diluted 1:1 with Buffer A and was cleared with a 100,000 RCF 30 mins centrifugation.

Supernatant was loaded onto a column packed with His-Select Fast Flow resin loaded with at a

speed of 0.1 mLs/min in Buffer A with a $C_{12}E_8$ conc of 2.5 mM. A detergent gradient was

performed to exchange into 0.5 mM Brij 58. Resin was washed in stepwise gradients with 15

column volumes of buffer A with 0.5 mM Brij 58 + 20, 40 and 60 mM imidazole and eluted with 200 mM imidazole in buffer A + Brij 58. In order to isolate a stoichiometric GαSβγ complex, sample was loaded onto a Q-column (GE Healthcare) and a gradient 150 mM to 450 mM KCl was performed. Pooled GαSβγ was incubated with TEV overnight and without His-tag was collected from the flow through of His-Select Fast Flow resin packed column.

2.4.7 PTH 1-34-PTHR1-Gα$_S$βγ Complex Formation

PTH 1-34-PTHR1-Gα$_S$βγ complex was assembled first by utilizing DLS in the manner described in section 2.4.3. The Brij 58 Gα$_S$βγ detergent was incrementally added to PTHR1 until the detergent caused aggregation. The same procedure was followed for Gα$_S$βγ to determine the maximal concentration of Fos-Choline 14 that it could endure. Once the tolerated concentrations of both detergents were determined, PTHR1 with 100 uM PTH 1-34 was left together for 1 hr. Subsequently PTH 1-34-PTHR1 was incubated for 1 hr with nucleotide free Gα$_S$βγ. The final buffer consisted of 50 mM KCl, 100 mM NaCl, 75 mM Hepes 7.5, 2 mM MgCl$_2$, and 15 mM imidazole. To isolate the complex, sample was loaded onto 2 mLs of His-Select Fast Flow Resin, washed with 5 x column volumes with buffer + 50 mM imidazole, before elution with 150 mM imidazole.

2.4.8 Crystallization Trials

Purified PTHR1 and truncation fragments crystallization trials were setup with or without 100 uM PTH 1-34 (Bachem) or 15-34 (SynBiosci). Commercially available kits from Hampton

Research, Molecular Dimensions and Emerald Bio were utilized for initial screening trials. In most instances 1-2 uL drops in a variety` of ratios were employed. Crystallization trials were performed, in most cases, across three temperatures, 4, 16 and 25°C. Potential hits were optimized along at least two variables including, salt concentration, PEG type and percentage, and pH. Crystallization trials were also performed using NeXtal CubicPhase monoolein and monoolein plus 8% cholesterol per manufacturers instructions. Agarose "in gel" screening experiments were performed as described in (115) for full length PTHR1 and K-480s. Bicelle crystallization experiments were also performed as described in (116). Seeding experiments were performed with the HR Teflon bead, per manufacture's instructions. Microseed Matrix Screening (MMS) was performed as described in (88).

2.4.9 Brightfield and UV Tryptophan Fluorescence Microscopy

Visual selection using an Olympus SZX16 brightfield microscope and corresponding 2XPFC objective were performed to identify crystallization drops that showed promising aggregates or near crystal hits for analysis by UV tryptophan fluorescence microscopy. Later rounds of experiments also utilized drops with visible precipitation with individual aggregates or a lawn of precipitate. Candidates selected visually were then subjected to UV fluorescence imaging with UV exposure from 1-5 s, using a Jan Scientific Jansi UVEX microscope. Images were analyzed using the Jan Scientific CrystalDetect software.

2.4.10 CPM Thermal Denaturation Assay

CPM thermal denaturation assays were adapted from the work of Alexandrov AI et al. (69). N-[4-(7diethylamino-4methyl-3 coumarinyl)phenyl]maleimide (CPM) and sample mixtures were protected from light at all stages to prevent photobleaching. CPM dye powder (Sigma) was dissolved in DMSO (Sigma) at a concentration of 4 mg/ml and aliquoted and stored at -80 °C. Stock solution was diluted 1:40 in DMSO immediately before use. Reactions were performed in sextuplicate with a total reaction volume of 20 µl. 10 µg of PTHR1 and mutants was used for each reaction in PTHR1 buffer with or without PTH 1-34 or PTH 15-34 with the addition of 6 µl of diluted CPM dye for each replicate. PTHR1-CPM reaction mixtures were prepared in MicroAmp Fast Optical 96-Well Reaction Plates (Applied Biosystems). Thermal melt curves were performed using a StepOnePlus (Applied Biosystems) using the protein melt curve program with a 25-95°C, 1% gradient. A custom dye calibration was performed to use CPM as a reporter. Melt curve data was processed in the Protein Thermal Shift Software (Applied Biosystems).

3.0   USE OF TRANSMISSION ELECTRON MICROSCOPY TO IDENTIFY

NANOCRYSTALS OF CHALLENGING PROTEIN TARGETS

3.1   INTRODUCTION

The emergence of x-ray free electron laser (X-FEL) based serial femtosecond crystallography

holds the promise of solving the three-dimensional structure of proteins that can only crystallize

as nanocrystals or are highly sensitive to radiation damage (117-121). "Nanocrystals" (NCs)

appropriate for X-FEL experiments are considered to be 200 nm to 2 µm (122). This size is

constrained primarily by the requirements of the NC delivery system to the X-FEL beam. In

addition to allowing for structure resolution of NCs by X-FEL experiments, they also provide the

advantage of requiring no crystal cryo-protection, as these experiments are performed at room

temperature (119, 123).   Given the new opportunities that X-FELs offer to the field of

crystallography, efficient methodologies to detect, from single crystallography drops, and

optimize these identified conditions yielding NCs, will be essential for future developments in

structural biology. Current methods to detect the presence of NCs include dynamic light

scattering (DLS), bright-field microscopy, birefringence microscopy, and intrinsic tryptophan ultraviolet (UV) fluoresce imaging, as well as technologies that rely upon Second Harmonic Generation such as Second Order Nonlinear Imaging of Chiral Crystals (SONICC) (124, 125) and X-ray powder diffraction. However, limitations of these imaging techniques include: 1) ineffective detection of crystals smaller than 5 μm (124, 126); 2) false positive conditions as a result of interference from precipitate backgrounds (124, 126); and 3) false negative conditions resulting from the lack of tryptophan residues in the case of UV fluorescence, and from the lack of chiral centers in the case of SONICC (127). Although DLS can accurately measure the size distribution of nanometer sized protein aggregates, it is unable to unambiguously distinguish between amorphous or crystalline (128). Finally, X-ray powder diffraction, a method that has been applied to evaluate samples for the presence and concentration of NCs, requires more material than is produced in a single crystallization screening drop; and the use of synchrotron radiation is usually required to produce measurable diffraction (100). In this study we use UV fluorescence microscopy and dynamic light scattering (DLS) to detect crystallization drops, of challenging proteins such as the PTHR1, containing NCs followed by TEM to accurately identify protein NCs and determine NC quality by evaluating the reciprocal lattice reflections in diffraction patterns calculated from images.
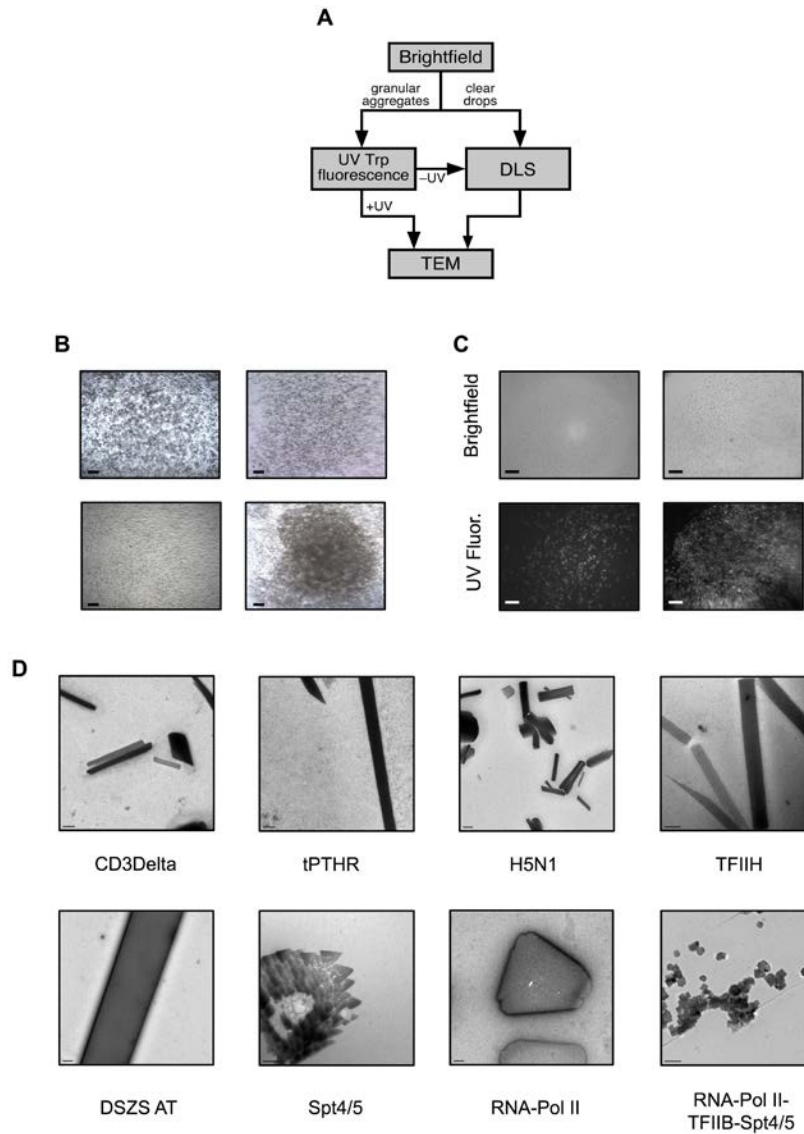
Figure 18. Four step pathway to the identification of protein nanocrystals

A) Flow chart of the protocol used to identify protein NCs from crystallization drops. B) Representative images of granular aggregates used for TEM. C) Brightfield and UV Fluorescence of granular aggregates, which can comprise UV-positive, well-differentiated nano-particles (left pair) or UV-positive, diffuse nano-aggregates (right pair). D) Examples of nanocrystals identified by TEM (Scale bars: CD3Delta 0.5 µm, tPTHR 0.5 µm, RNA-Pol II-TFIIB-Spt4/5 200 nm, TFIIH 200 nm, DSZS AT 0.5 µm, Spt4/5 200 nm, RNA-Pol II 0.2 µm, H5N1 0.2 µm).

In order to develop a comprehensive method for identifying NCs, a four-step pathway was devised (**Figure 18**). A variety of targets from three different systems were chosen as test cases, including soluble proteins, membrane proteins, and multi-protein complexes as shown in Table 3.
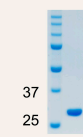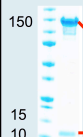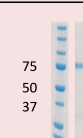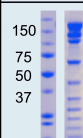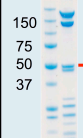
Soluble Protein Name, Expression system, Yield, Tray setup conc.	SDS-PAGE of Purified Protein	Multi-Protein Complexes Protein Name, Expression system, Yield, Tray setup conc.	SDS-PAGE of Purified Protein
The trans-acting acyl transferase from the disorazole synthase (DSZS AT) *E. coli* 50 mg/L 5 mg/mL		SPT4/5 *E. coli* 15 mg/20 g 8 mg/mL	
Membrane Protein Name, Expression system, Yield, Tray setup conc.	SDS-PAGE of Purified Protein	RNA Pol II+ SPT4/5 *S. Cerevisiae* & *E.coli* 25 mg/Kg & 15 mg/20 g 4-5 mg/mL	
H5N1 COBRA Influenza Virus Hemagglutinin protein (COBRA) *S. frugiperda* 8 mg/L 3.5 mg/ml		RNA Pol II + TFIIF *S. Cerevisiae* & *E. coli* 25 mg/Kg & 10 mg/Kg 8 mg/mL	
Parathyroid hormone receptor (PTHR1) *E. coli* 1.5 mg/L 1.5 mg/mL		RNA Pol II + GFP *S. cerevisiae* & *E.coli* 25 mg/Kg & 50 mg/L 5 mg/mL	
Thermostabilized PTHR1 (tPTHR) *E. coli* 1.5 mg/L 5 mg/mL			

Table 3. Proteins used in nanocrystallography screening

To the left of each SDS-PAGE gel showing the final purified protein is the full name of the protein, the expression system along with the protein yield and protein concentration used for setting up trays.

Crystallization of protein samples using commercially available screens typically yields a spectrum of morphologies including: 1) clear drops **Figure 19A**; 2) drops with granular aggregates (which can be amorphous or comprised of well-differentiated individual particles) (**Figure 19B**); 3) drops with large solid aggregates (probably associated with sample denaturation) (**Figure 19C**); and 4) drops with phase separation. Such morphologies depend on the protein sample and the chemical nature of the precipitant **Figure 19**. For this study, conditions yielding granular aggregates (**Figure 19B**) and clear drops were selected for further analysis.
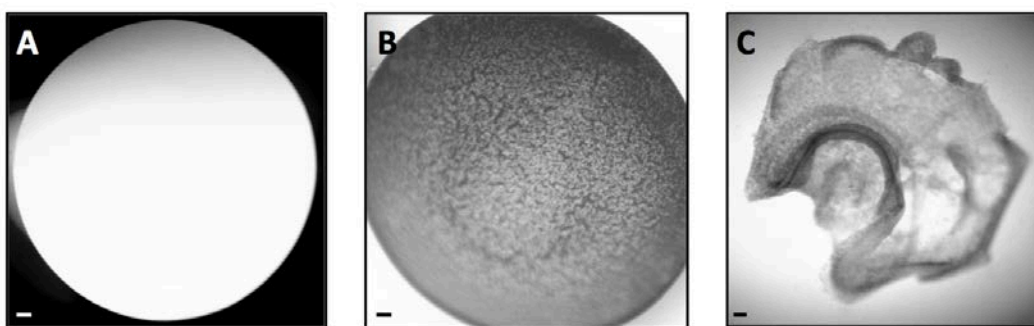
Figure 19. Representative brightfield microscopy images of typical crystallography screening experiment outcomes

A) clear drops, B) granular aggregates and C) denatured protein. Scale bar (A) 300 μm (B) 300 μm and (C) 160 μm.

To determine whether granular aggregates were proteinaceous in nature, UV tryptophan fluorescence microscopy was used (Jansi UVEX) (129). Drops with UV-positive granular aggregates were selected for direct TEM visualization (**Figure 18C**). Since clear drops have been shown to yield NCs (130), and UV tryptophan fluorescence microscopy can yield false negatives (16) (131) UV-negative granular aggregates and clear drops were further processed using DLS to

assess the presence of nanoparticles (**Figure 20**). DLS measurements were performed using a Wyatt DynaPro Plate Reader Plus in batch mode (ideal for screening large numbers of crystallization conditions). In order to accurately assess the size of the primary nano-species of the sample, calibration studies using nanospheres (Polysciences, Inc.) with particle radii of 50, 100 and 1000 nm were compared to the sample's autocorrelation function and decay time (**Figure 20A**). DLS measurements of clear drops and UV-negative granular aggregates allowed detection of particles with diameters of 50-1000 nm (**Figure 20B**). In order to determine whether these particles were crystalline or merely protein aggregates, further assessment using TEM was performed.

Microspheres Size (nm)	DLS Acquired Diameter (nm)
50	62.36
100	103.06
1000	1093.8

Protein	1° Species Diameter (nm)
PTHR	873.16
Salt	459.06
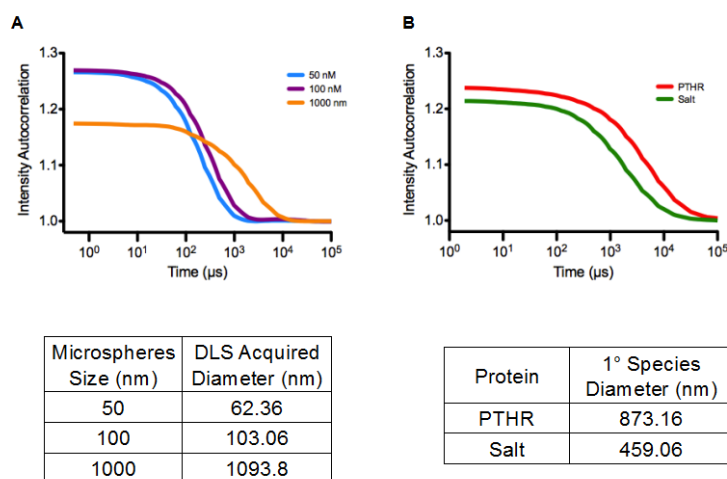
Figure 20. Comparison of correlograms of commercially available nanospheres, PTHR1 and salt

UV- and DLS-positive samples were applied to a copper grid with continuous carbon film, stained with a 2% solution of uranyl acetate and imaged using an FEI Tecnai T12 transmission electron microscope. Samples were taken directly from the crystal tray before transferring to a grid. In most circumstances, a single crystal drop containing thick aggregates was of sufficient concentration for imaging. For the majority of samples tested, TEM visualization (**Figure 21**)

provided an efficient method to reveal whether samples contained NCs or large protein aggregates. In addition, the presence of detergents in crystallization buffers did not appear to have a negative impact on visualization, and we were able to detect NCs for three membrane proteins, T-cell surface glycoprotein CD3 delta chain (CD3Delta), thermostabilized Parathyroid Hormone Receptor (tPTHR) and Influenza Virus Hemagglutinin protein (H5N1) (**Figure 18D**). Since TEM allows visualization of crystal lattices, protein NCs could be discriminated from salt crystals, including those coated with protein aggregates that generated false-positive UV-signals (**Figure 22A**).
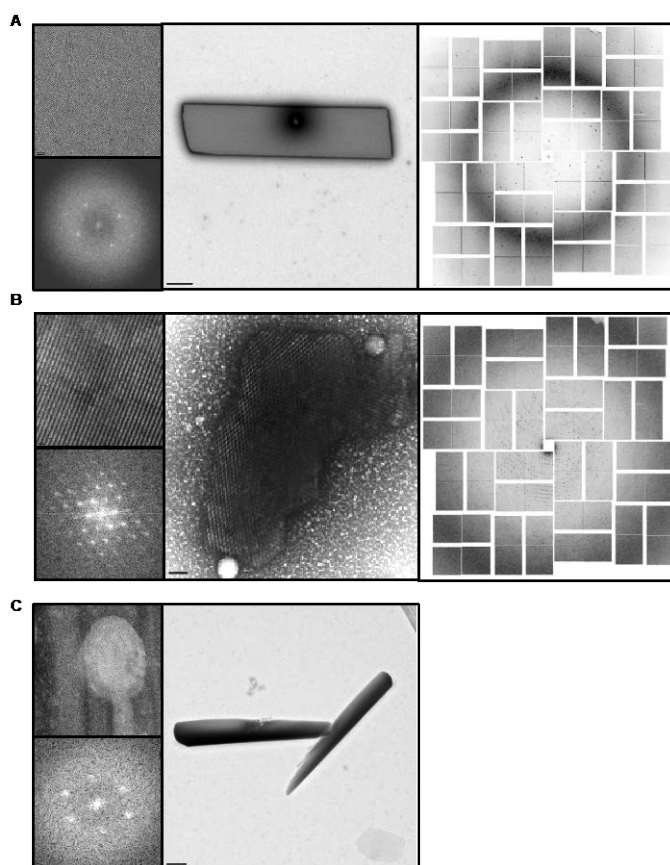
Figure 21. TEM images of NCs (center), accompanying lattice and FFT (left) and X-FEL

diffraction pattern (right)

A) DSZS AT diffraction up to 1.8 Å resolution. B) RPBII -GFP with diffraction up to 4 Å acquired at LCLS. Scale bar from top left to larger image (A) 20 nm and 1 μm, (B) 50 nm and 100 nm

X-FEL experiments were used to test diffraction of NCs with high quality lattices. Both, the *trans*-acting acyl transferase from the disorazole synthase DSZS AT (**Figure 21A**) and RBPII-GFP (**Figure 21B**) yielded significant diffraction. On the other hand, NCs of PTHR1 with poorly ordered lattices showed no diffraction. Lattice visualization of thick NC was performed by fragmentation using 0.5 mm glass beads. This was a highly successful means of expanding the size range of NCs examined by TEM as shown in **Figure 23**.
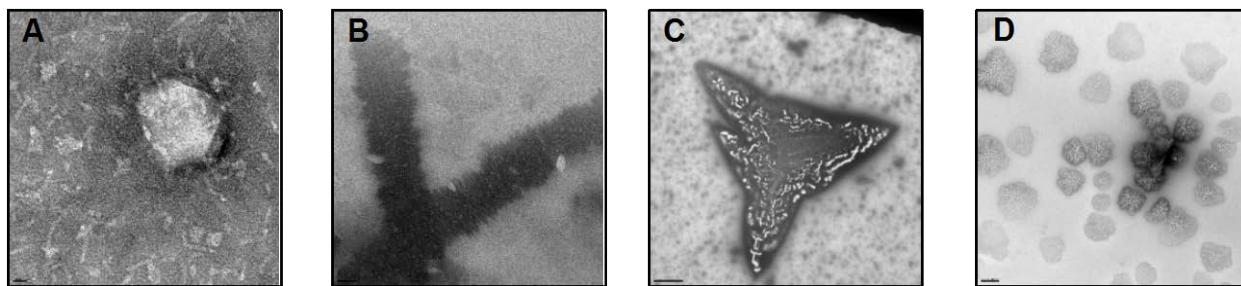
Figure 22. Commonly observed salt nanocrystals

A) Calcium chloride NCs coated in protein filaments, B) Bis-tris pH 6.5 & PEG MME 2000, C) Sodium chloride D) Tacsimate (Hampton Research). Scale bars (A) 20 nm, (B) 50 nm, (C) 2 μm and (D) 0.5 μm.

UV- and DLS-positive samples were applied to a copper grid with continuous carbon film, While most NCs identified by TEM came from crystallization drops with UV-positive granular aggregates, a few were identified from UV-negative granular drops using DLS. We were unable to find protein NCs in clear drops that were preselected via DLS – most particles observed by TEM corresponded to large protein aggregates and salt crystals. However, since our observations were performed in a relatively small number of samples (around one hundred crystal drops), thorough DLS evaluation of all conditions may provide hits when UV positive conditions are scarce.
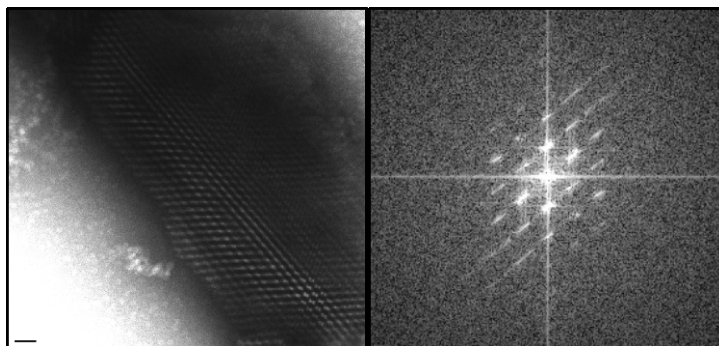
Figure 23. Lattice visualization of thick RPBII-II NC after fragmentation using 0.5 mm glass beads

3.3   DISCUSSION

Crystallization screening of protein samples involves setting up hundreds and sometimes thousands of crystallization drops often without a single macro-crystal 'hit'. However, the emergence of X-FEL based serial femtosecond crystallography demonstrates that the field of X-ray crystallography can be expanded to solve three-dimensional structures of protein samples from NCs (117-121, 129, 132). To this end, an efficient method to detect the presence of protein NCs in UV-positive granular aggregates from crystallization drops using classic negative-stain transmission electron microscopy was developed.

This investigation demonstrates that crystallization trials of most protein samples can potentially yield NCs even for challenging systems such as membrane proteins like the PTHR1 as well as multi-protein complexes. In addition to NC identification, the use of TEM may provide additional insights including: 1) the possibility of finding NCs with different crystals forms; and 2) the evaluation of NC diffraction quality. Since crystalline lattices can be directly visualized with TEM, calculating Fourier transforms from the images allows qualitative

evaluation of electron diffraction patterns (Bragg spots). Three examples of clear lattices with two or higher order spots are evident in the reciprocal lattice reflections obtained by Fourier transform **Figure 24**. However due to the limitations of negative stain techniques using uranyl acetate –including room temperature diffraction, sample dehydration and possibly crystal cracking due to interference of the dye with the crystal lattice– restricted electron diffraction to low resolution (approximately 20 Å resolution). In spite of these limitations these experiments suggest that selection of crystals with higher order diffraction spots could potentially yield higher resolution X-ray diffraction data.
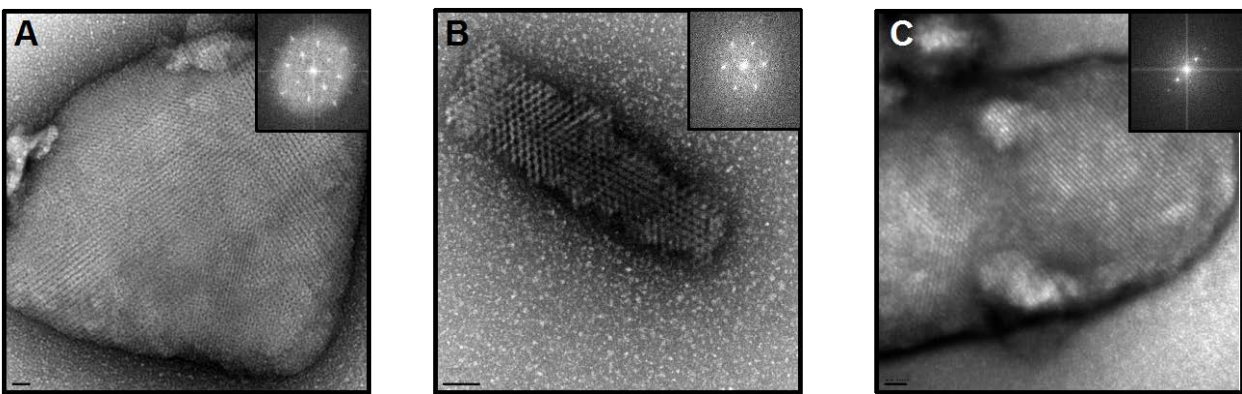
Figure 24. High quality lattices of NCs visualized by TEM

A) Lysozyme B) RPBlI-GFP, C) Pol-TFIIF. Scale bar (A) 50 nm, (B) 100 nm and (C) 20 nm.

This is not the first characterization of NCs by TEM, but rather shows that NCs are commonly observed in crystallization drops of proteins of high biological interest; and that evaluation of the crystal lattices of negatively-stained NCs can provide preliminary qualitative information of their diffraction potential. Recent efforts have provided detailed characterization of lysozyme NCs electron diffraction by calculating FFT from their highly ordered lattices (107). Moreover, electron diffraction experiments where three lysozyme NCs were used to collect a full tilt-series allowed lysozyme structure determination by molecular replacement and refinement to 2.9 Å resolution (101). Given these new advances, the work presented here offers the possibility

to expand electron crystallography studies to proteins of high biological relevance. Moreover electron crystallography techniques could supplement X-FEL experiments for those proteins that cannot yield the high crystal volumes required. Electron crystallography is a field under development and further experiments will be required to prove its feasibility on NCs of other biological samples and ultimately the diffraction resolution that can be achieved using this technique (since lysozyme dataset was refined to a final resolution of 2.9 Å (20)), while conventional X-ray diffraction experiments of lysozyme crystals can reach atomic resolution.

This chapter presents a method for pre-screening NCs with no previous large crystal hits for use at an X-FEL. This work demonstrates the potential of TEM to serve as a fundamental tool for evaluating NCs, as essential as brightfield microscopy is for evaluating and optimizing traditional, large crystals.

3.4   MATERIALS AND METHODS

3.4.1   Protein Production and Crystallography Condition Screening

Eight proteins were used for nanocrystallography screening, as shown in Table 3 along with the expression system, protein yield and maximal concentration (while maintaining monodispersity) that was used to set up trays. The expression and purification of PTHR, CD3-Delta and RNA Polymerase (RPBII) and complex formation with RPBII were performed as described (133) while DSZS AT expression and purification are described separately (134). Thermostabilized PTHR (tPTHR) was purified following the same protocol as described for full length PTHR. TFIIF was purified as previously described (135). GFP was expressed and purified

by standard methods (136). RPBII-TFIIF and RPBII-GFP complexes were assembled by adding 2.5 molar excess of TFIIF or GFP to RPBII. RPBII-TFIIF was purified using calmodulin-affinity chromatography. The RPBII-GFP complex was isolated using a Superdex 200 10/300 GL (50 mM Hepes pH 7.5, 100 mM KCl, 4 mM DTT, 2 mM $CaCl_2$ and 10 μM $ZnCl_2$). Spt4 and Spt5, as well as TFIIB and H5N1 were purified as described in (137). Lysozyme NCs were grown with protein purchased from Sigma and was crystallized in the presences of 10% NaCl and 100 mM sodium acetate.

A variety of commercially available crystallography screens were utilized for nanocrystallography screening including the Hampton Research screens Crystal Screen 1 and 2, Index, PEG/Ion, SaltRx, Silver Bullets and MembFac as well as Qiagen JCSG. Both hanging (Hampton Research VDX™ Plates) and sitting drop (Hampton Research Cryschem Plates) methods were used for screening 4 µl drops, they were set up in a 1:1 ratio of protein to precipitant so as to have sufficient volume for further DLS and TEM experiments. 350 µl of commercial screening solution was used in the well for each condition.

3.4.2 Generating Crushed Crystals of Thick Nanocrystals

0.5 mm glass beads (Research Products International) were used to crush NCs too thick for lattice visualization by TEM. 20 mg of beads were placed in a 1.5 µl microcentrifuge with the addition of the NC sample directly from the crystal plate along with 5 µl of reservoir solution. Samples were vortexed for 10 sec, twice, before being used for TEM grid preparation.

3.4.3 Generating Crushed crystals of the DSZS AT for X-FEL analysis

The DSZS AT was purified and crystallized as previously described (134), by mixing 10 μl well solution with 10 μl of purified protein at 5 mg/ml, and allowing crystals to grow at room temperature for up to one week. The crystallization solution contained 18-24% PEG 3350, 100 mM Na-HEPES pH 7.5, and 40 mM ammonium acetate. Approximately 900 μl of drops containing crystals were collected. When the crystals had settled to the bottom of the tube, we estimated that the mixture contained approximately 50% crystals. The crystals were held at room temperature until crushing and exposure to the LCLS X-FEL. The tube was inverted several times to re-suspend the crystals, and the samples were crushed in 90 μL aliquots by vortexing at high speed for 3 min with a Teflon seed bead (Hampton Research HR2-320). Examination of crystal samples under a standard light microscope revealed large crystal fragments (edges >10 μm). Therefore, samples were further processed through a 10 μm^3 filter prior to exposure with the LCLS using the Coherent X-ray imaging (CXI) instrument.

3.4.4 X-FEL Analysis of Nanocrystals

Diffraction experiments were carried out at the CXI endstation of the LCLS (138) using 10.5 keV x-ray pulses of 40 fs duration for measurements of RPBII-GFP and PTHR and 8.5 keV x-rays pulses of 50 fs duration for DSZS. Crystal delivery was performed using the gas dynamic virtual nozzle (GDVN) (101) using an injection rate of 20 μL/min and a pressure of 750 PSI nitrogen, 300 PSI shield. Data were analyzed using the CCTBX.XFEL software package (139). The RPBII-GFP sample yielded a hit rate of approximately 2.5%, and an indexing rate of 0.6%, 25% of hits (using a threshold of 16 spots above 450 ADUs per image). Resolution of the best

images was up to 4 Å. The DSZS sample yielded a hit rate of approximately 2.7%, and an indexing rate of 0.07%, 29% of hits (using a threshold of 16 spots above 450 ADUs per image). Resolution of the best images was up to 1.8 Å.

3.4.5   Nanocrystals Candidate Identification and UV Tryptophan Screening

Visual selection using an Olympus SZX16 brightfield microscope and corresponding 2XPFC objective was performed to identify nanocrystal candidates. Drops that either had visible precipitation with individual aggregates or a lawn of precipitate were selected for UV-fluorescence imaging, as shown in the examples of Figure 1B and Supplemental Figure 1. Candidates selected visually were then subjected to UV fluorescence imaging with UV exposure from 1-5 s, using a Jan Scientific Jansi UVEX microscope. Images were analyzed using the Jan Scientific CrystalDetect software. Once UV-positive conditions were identified, drops were harvested and high quality images were taken of each drop using an Infinity 2-3C camera and Infinity Capture software from Lumenera Scientific. Harvested drops were subsequently used for DLS and TEM experiments.

3.4.6   Dynamic Light Scattering

To test the limits of the Wyatt DynaPro plate reader for detecting nanoparticles of various radii, silica spheres (PolySciences, Inc) experiments were performed in a 384 Corning clear bottom plate using beads diluted 1:1000 with Millipore water with 15 µl of diluted beads deposited in the well. DLS data was acquired by performing 20 acquisitions, 6 sec each acquisition, at 18 °C.

To determine the uniformity as well as the range of the precipitate size of selected nanocrystal candidates, samples were taken directly from the drop of the crystallization plate and put into a Greiner Sensoplate (glass bottom) 1536 well plate and DLS data was collected for 20 acquisitions, 6s each acquisition, at 18°C. These plates allowed a low working volume for screening (3 µl) as well as enhanced data clarity due to their glass bottoms. Samples were diluted with precipitant up to a volume of 3 µl when necessary. If low intensity was observed and sufficient protein was available, additional drops were set up using the same conditions and combined to increase intensity.

3.4.7 Transmission Electron Microscopy

400 square mesh copper grids with continuous carbon film (Electron Microscopy Sciences) were freshly glow-discharged for 1 min, 25 mV (EmiTech KX100) before incubation with samples. Selected samples were applied to grids by two methods depending on the concentration of nanoparticles. When a sufficiently high concentration of particles was present (i.e., when particles were visible, dense and gave a DLS intensity signal above 1.25), 5-8 µl of sample was applied and incubated for 30 sec on a grid before blotting and staining with 2% uranyl acetate. Lower density samples were applied to the grid by placing a drop of the sample in a parafilm-lined petri dish along with at least 300 µl of precipitant from the sample's origin in close proximity to the sample drop. A grid was put on top of the drop of sample, carbon side down, and the petri dish was sealed and the sample was allowed to incubate for 10-60 min before staining with uranyl acetate. TEM images were acquired using an FEI Tecnai T12 electron microscope operating at 120 kV using a single-tilt specimen holder. Images were collected with a 2 k x 2 k Gatan UltraScan 1000 CCD camera.

4.0 TRANSMISSION ELECTRON MICROSCOPY AS A TOOL FOR NANOCRYSTAL CHARACTERIZATION PRE- AND POST- INJECTOR

4.1   INTRODUCTION

As described in sections 1.2.2.1 and 3.0 the intense, ultra-short pulses produced by the Linac Coherent Light Source (LCLS) at SLAC have expanded the boundaries of structural biology research, enabling the collection of atomic resolution X-ray diffraction patterns from protein crystals that are too small or too radiation sensitive for conventional data collection at synchrotrons. In less than 50 fs, a pulse delivered by the LCLS X-FEL can expose a crystal to as many X-ray photons as a typical synchrotron beam produces in about a second. This has enabled a 'diffraction before destruction' (140) approach to overcoming radiation damage, where a single diffraction image is produced by a single LCLS pulse before a crystal succumbs to the damaging effects of X-ray exposure; and to obtain a complete dataset, single shot diffraction patterns from thousands of individual crystals are combined (122). These experiments are carried out in vacuum (to reduce background scatter) at the Coherent X-ray Imaging endstation (CXI) at the LCLS (138). Injectors are used to deliver crystals of submicrometer dimensions (or up to 5μm)

suspended in small diameter jets or drops of aqueous solutions (101) to a series of LCLS X-ray pulses, produced at a repetition rate of up to 120 Hz. These innovations have enabled serial femtosecond crystallography (SFX) experiments to solve crystal structures using diffraction data from nano-meter sized crystals (117-121, 141) opening the door to obtain atomic information from proteins whose intrinsic disorder prevented formation of micro-meter sized crystals such as many membrane proteins and large multi-protein complexes (MPCs).

The first SFX experiments used a Gas Dynamic Virtual Nozzle injector (GDVN) (101, 142) for crystal delivery. The GDVN (117, 118, 120, 122, 143-147) is currently the primary injector supported at CXI for crystal screening experiments. Other sample delivery systems, such as the nanoflow electrospinning injector (147), have subsequently been developed and offer advantages such as reduced flow rate and thereby lower sample consumption by minimizing sample loss between X-ray pulses. Acoustic and micro-piezo activated drop-on-demand technologies are also in development.

The high demand for LCLS beamtime necessitates careful sample pre-characterization and injector compatibility testing to ensure efficient use of this limited resource. It is standard practice to test the crystal containing solutions with an offline sample injector prior to beam time to detect problems with jet formation due to solution bubbling, clogging from crystal clumping, or the solution drying out as it exits the injector nozzle and enters the vacuum chamber. These issues may often be eliminated by modifying the carrier solution, for example by minimizing the use of detergents or reducing salt concentration. For crystal and solution optimization, an offline setup of the GDVN injectors is available to users through the sample-delivery group at the LCLS. These flow tests however do not detect the presence of diffraction quality crystals in the injector reservoir, or exiting the injector nozzle.

Nanometer sized crystals (NCs) of membrane proteins and large MPCs are often mechanically fragile. This fragility maybe further aggravated during the sample delivery process by exposure to high pressure and shear forces. Furthermore, injector efficiency may be reduced by NC clumping and aggregation in fittings such as those connecting the sample reservoir to the nozzle capillary. Therefore, methodologies to detect the presence and quality of NCs within the injector reservoir, and exiting the injector nozzle are essential to test the applicability of injector technologies to specific NC types, and to optimize the carrier solutions.

The work presented here demonstrates the potential of transmission electron microscopy (TEM) to serve as a tool for detecting and evaluating NCs both before and after the injection process. NC diffraction quality may be assessed by calculating the electron diffraction pattern of the NC lattice by Fast Fourier Transform (FFT).

4.2   RESULTS

Three types of NCs were tested. The PTHR1 was selected as a representative membrane protein. The PTHR1 is an example of a protein where only NCs, 200-500 nm in size, have been produced. The second type, a construct comprising a calmodulin-green fluorescent protein (GFP) chimera bound to calmodulin-binding peptide (CBP) tagged Rpb4 subunit of RNA polymerase II (RPBII-GFP) serves as a representative MPC. This is a green-colored protein with a large crystal lattice readily identifiable by transmission electron microscopy with crystal sizes ranging from 1-5 µm. The crystallization conditions for these systems were determined through direct examination of commercial crystallization screening drops using a novel selection protocol that combines 1) brightfield microscopy, UV fluorescence microscopy and dynamic light scattering

71

(DLS) as screening methods to detect crystallization drops containing NCs; and 2) transmission electron microscopy to accurately identify protein NCs and determine NC quality (133). Lysozyme NCs were also tested as a soluble protein control.
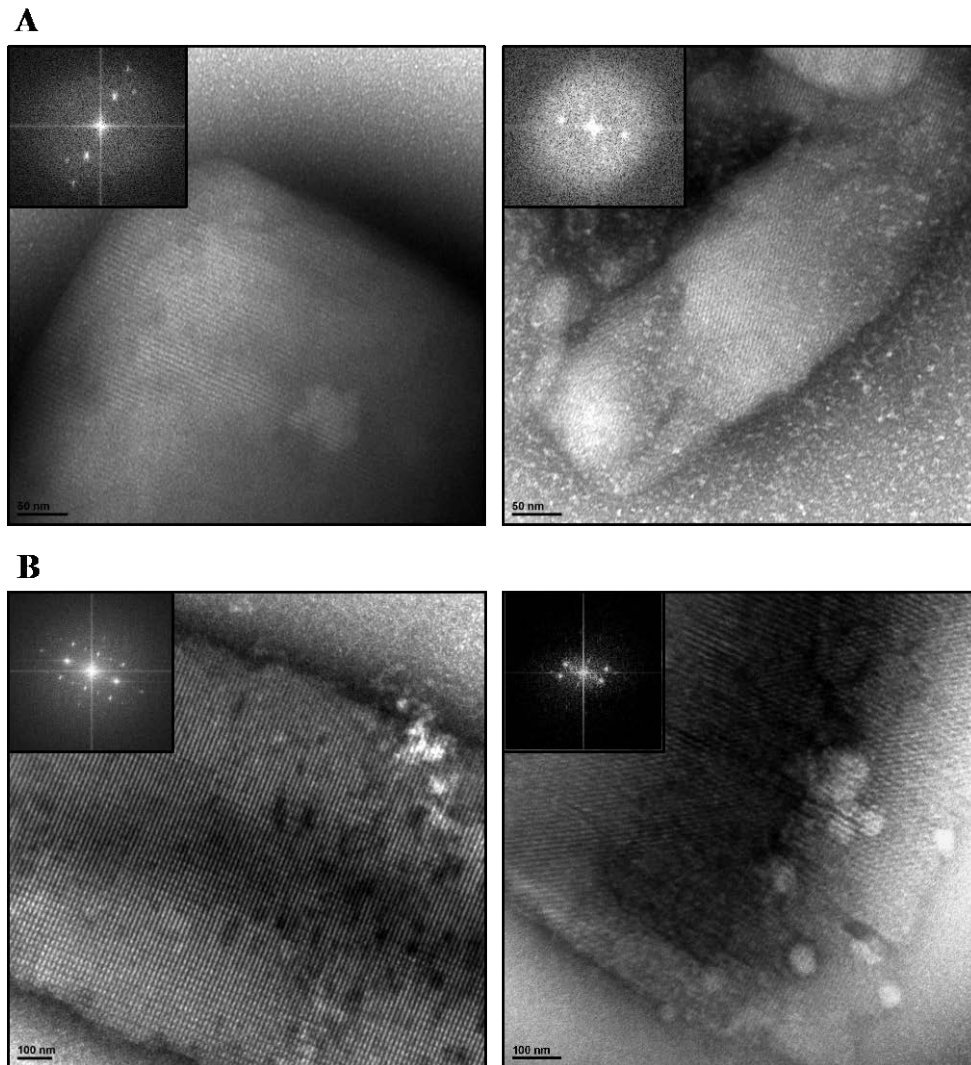
Figure 25. TEM images of pre- and post- jet nanocrystals

A) Lysozyme pre- and post- jet, left to right, b) RPBII-GFP

As shown in **Figure 25A** and **B** both lysozyme and RPBII-GFP survived the injector. Both pre-injector and post-injector NCs show clear identifiable lattices and at least third order evenly distributed Bragg spots obtained by Fast Fourier Transform (FFT) of the TEM images.

The lattices for lysozyme were observed to be of similar quality both pre- and post-injector. As shown in **Figure 25B**, the quality of the post-injector RPBII-GFP NC lattices was slightly decreased, as indicated by a reduction of Bragg spots from the FFT. As expected from our TEM pre-screening results, during X-ray screening at LCLS CXI the RPBII-GFP NCs produced a number of quality diffraction patterns to 4 Å resolutions, as shown in **Figure 26**.
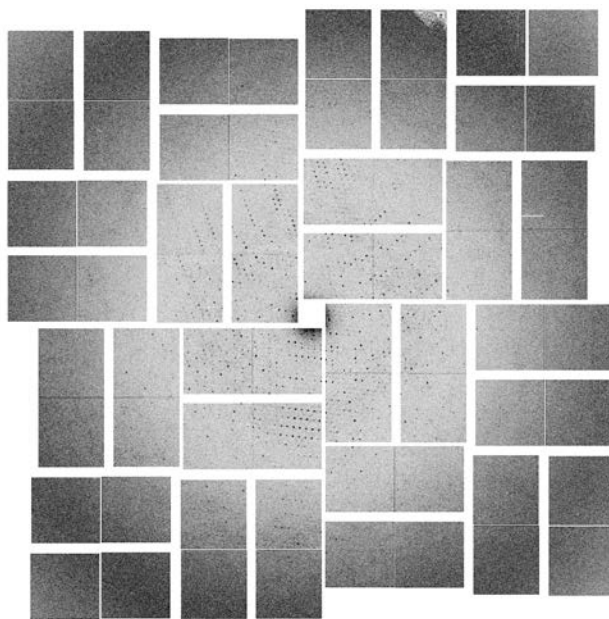
Figure 26. X-ray diffraction image from RPBII-GFP collected at LCLS in Nov 2013

For PTHR1 the overall NC concentration was reduced post-injector. A few examples of crystals with a more distinct lattice **Figure 27** were found in the post-injector grids that were more sparsely populated; however the overall change in lattice quality was modest, and did not differ pre- and post-injector. A significant contributor to the lower post-injector NC concentration observed in this case is the tendency of these NCs to clump together and gather in the fitting located just prior to the GDVN nozzle capillary. Modification of the internal form

factor of the tubing-to-capillary connection may help resolve these problems. To reduce clumping during the experiment at CXI, crystallization conditions were optimized by adjusting PEG and salt concentrations. No diffraction was observed from PTHR1 during SFX experiments at CXI. However, a distinct low resolution powder ring (40 Å) was observed when a loop of this NC containing reservoir solution was tested at the Stanford Synchrotron Radiation Lightsource BL12-2 at RT using a 20 x 20 µm X-ray beam at 12.5 keV. While the lack of diffraction observed during SFX experiments may be due to a low concentration of NC in the post-injector solution, resulting in zero diffraction 'hits', we attribute this negative outcome to crystal disorder. The FFT obtained from the TEM images of PTHR1, even for the more ordered lattice **Figure 27**, shows only low order electron diffraction and predominantly in just one lattice direction. While initial results for this protein have been discouraging, we expect that successful SFX experiments using PTHR1 and the GDVN may be feasible through careful optimization of crystallization conditions with NC examination pre- and eventually post-injector using TEM.
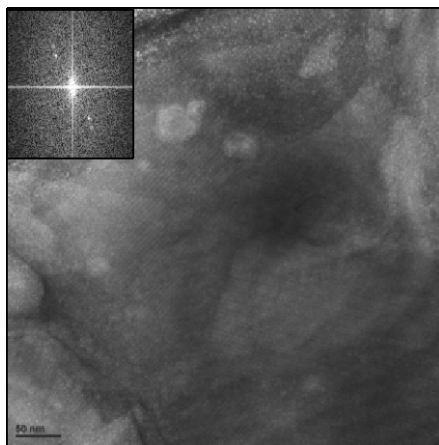
Figure 27. PTHR1 lattice and FFT (insert) observed in the post-injector sample

4.3   DISCUSSION

X-ray free electron lasers offer the possibility to solve 3-dimensional structures of proteins that can only crystallize as NCs, and methods to distinguish NCs, optimize NC quality, and evaluate ideal sample delivery options prior to beamtime are essential components for efficient use (and in some cases successful experiments) of these high demand facilities. This study demonstrates the utility of negatively stained transmission electron microscopy as a straightforward tool for distinguishing NCs with edges shorter than 5 µm, and for evaluating the NC lattice both prior to and post injector. X-ray diffraction quality of NCs may be assessed through examination of the NC lattice in TEM images both visually and by calculating the FFT of the image. While more work is necessary, these results indicate that evenly distributed 3rd order or higher Bragg spots in the FFT of negative stained lattice images could be a prerequisite for obtaining measureable X-ray diffraction patterns at X-FEL sources. Since cryo-electron microscopy does not rely on the use of harsh stains, (potentially damaging NCs) and can provide higher resolution images, this method could constitute a more accurate method to evaluate NC quality. A future study to correlate electron diffraction with X-FEL diffraction could assist the experimenter to select the best possible samples to be tested at X-FEL.

The effects that the injection process in itself could have on diffraction quality have not been previously investigated using TEM. These effects could be of great consequence for fragile crystals with high solvent contents or for membrane proteins solubilized in detergents such as the PTHR1. The initial results using the GDVN show that: 1) crystal concentration pre- and post-injector may vary significantly and 2) analysis of post-injector crystals using TEM shows that diffraction quality of NCs could potentially be adversely affected by the delivery process. As indicated by the examination of RPBII-GFP crystals that have 75-80% solvent content, these

effects could be of particular relevance for samples with high solvent content. The success of SFX experiments may be appreciably improved through careful optimization of the carrier solutions and injector configuration for particular nano-crystal types through the use of TEM to assess diffraction quality both pre- and post-injector.

4.4   METHODS

4.4.1   Protein Expression and Purification

PTHR1 and RPBII were expressed and purified as described previously (133). GFP was expressed and purified by standard methods (136). RPBII-GFP complex was assembled by adding 2.5 molar excess of GFP in the presence of 1 mM $CaCl_2$ to promote calmodulin-CBP binding followed by isolation using a Superdex 200 10/300 GL (50mM Hepes pH 7.5, 100 mM KCl, 4 mM DTT, 2 mM $CaCl_2$ and 10 μM $ZnCl_2$).

4.4.2   Protein Crystallization

Lysozyme NCs were grown with protein purchased from Sigma and were crystallized in the presences of 10% NaCl and 100 mM sodium acetate. Crystallography conditions for PTHR1 NCs were 200 mM NaCl, 100 mM Bis-Tris pH 5.5, 25% Polyethylene Glycol (PEG) 3350. RPBII-GFP nanocrystals were grown under 4-6% PEG 8000, 200 mM MgCl2, 1 mM $CaCl_2$, 100 mM Tris pH 7.5 and 10 mM dithiothreitol (DTT).

4.4.3   GDVN Injector

An offline GDVN injector was setup on the laboratory bench and an optical microscope was used to observe the nozzle and appearance of the ejected NC containing solution. The GDVN nozzle consists of two coaxial capillaries; a smaller diameter capillary (40 μm ID) that transports the crystal containing solution is centered inside a larger capillary that delivers a pressurized gas stream (typically helium) that surrounds and focuses the liquid stream as it exits the nozzle. The same nozzle was used to eject the PTHR1 and the RPBII-GFP solutions and a comparable nozzle was used with the lysozyme solution. For each tested solution the gas and liquid pressure (on the order of 200 to 2000 psi) were varied to produce a continuous stream of liquid extending at least a few mm outside of the nozzle. (The X-ray interaction region is around 100 μm from the end of the nozzle.) Table 1 lists the gas and liquid pressures used for each NC type. While the GDVN normally delivers solution into a vacuum chamber, for these experiments it was operated in air to facilitate collection of the post-injector solutions. The liquid stream from the GDVN is about 5 μm in diameter, travels at a velocity of about 10 m/s and may transport suspended crystals with edges of 10 μm or less. To prevent clogging, the crystal containing solutions may be first filtered, typically by a 10 μm porosity filter, before flowing through a 1/16" outer diameter tubing reservoir connected to the central capillary of the GDVN nozzle. Solutions exiting the GDVN nozzle were collected onto an upper portion of an inside wall of a centrifuge tube which was immediately sealed. To help prevent dehydration, the bottom of the centrifuge tube contained a small amount of crystallization precipitant solution (protein free).

Crystal Type	Crystallization / Carrier Solution	Crystal Volume (%)	Liquid Pressure (psi)	Shield Gas Pressure (psi)
Lysozyme	10% NaCl, 100 mM Na Acetate	80	500	550
PTHR1	200 mM NaCl, 100 mM Bis-Tris pH 5.5, 25% PEG 3350	30	1200	932
RPBII-GFP	4-6% PEG 8K, 200 mM MgCl2, 1 mM CaCl2, 100 mM Tris pH 7.5 and 10 mM DTT	60	750	300

Table 4. Nanocrystal conditions used with the benchtop GDVN injector

4.4.4 Transmission Electron Microscopy

NC samples were harvested both pre- and post-injector, then stored on ice until needed for grid preparation. Copper grids with carbon film (Electron Microscopy Sciences) were made hydrophilic in a glow discharge for 1 minute at 25 mV (EmiTech KX100). The samples were incubated on a hydrophilic grid for 1 minute, blotted and twice incubated in 2% uranyl acetate solution for 30 seconds. The resulting crystal confluence was approximately 70% pre-injector and 45% post-injector for the lysozyme samples, 45% pre-injector and 10% post-injector for the RPBII-GFP samples and 15% pre-injector and very low post-injector for the PTHR1 samples. A FEI Tecani T12 electron microscope operating at 120 kV, using a single-tilt specimen holder, equipped with a 2 k x 2 k Gatan UltraScan 1000 CCD camera for acquiring images, was used to visualize sample grids. Using the FEI T12 User Interface program, images were acquired using auto-exposure and low dose mode. The focus of the images was adjusted by minimal contrast and by live FFT. The images were defocused by -500 to -1500 nm in order to obtain more

distinct lattice fringes. A select region of the NC lattice underwent a fast Fourier transform using DigitalMicrograph (Gatan, Inc).

4.4.5 Diffraction Screening at CXI

SFX experiments using solutions of RPBII-GFP and PTHR1 receptor were carried out at the LCLS CXI instrument (138) using 10 keV X-ray pulses of 40 fs duration with focus size of 200 nm at the X-ray interaction region. The GDVN injector was used for sample delivery using solutions with crystal concentrations of approximately 30% NCs w/v. Diffraction patterns were recorded at 120 Hz using a Cornell-SLAC Pixel Array detector (148) and analyzed in real time using cctbx.xfel (139). Only RPBII-GFP yielded diffraction patterns, and a 2.5% hit rate was obtained with 25% of hits producing indexable images. Hits were determined with a threshold of 200 ADU (determined from light averages of the data) and indexing was performed using the mod_hitfind module of cctbx.xfel with a target cell determined from previously acquired synchrotron datasets.

5.0 NANOSEEDING: A NEW METHOD TO GROW CRYSTALS OF SPECIFIC SIZE FROM A VARIETY OF SEED SOURCES

5.1 INTRODUCTION

X-ray crystallography remains the most successful method to obtain structural information from biological targets, and structures solved by this method comprise 80% of the current protein data base entries. Advances in molecular biology and biochemical techniques have allowed expression and purification of a significant number of new protein targets including pharmacologically relevant proteins (149-151). Similarly, innovations in synchrotron science including development of micro-focused x-ray beams and advances in detector technologies as well as development of user-friendly crystallography software packages have expedited crystal-to-structure time frames. However, in spite of the abundance of targets and the increasingly faster crystal-to-structure pipeline, crystallization of protein targets remains the most significant bottleneck in structure determination by X-ray crystallography. These challenges have persisted despite the significant advances in protein modifications to enhance the crystallizability of challenging targets. These novel efforts include target manipulations such as alanine-scanning mutagenesis (152-156), thermo-stabilization (156, 157), chimeric proteins favoring crystal contacts (53, 56) or stabilizing Fab (158, 159), and nano-bodies (44, 160). Though these techniques have led to successful three-dimensional structures of an increasing

number of pharmacologically relevant proteins, challenges still remain in crystallizing a variety of protein targets of interest.

Seeding is another long-standing optimization tool in the crystallographer's arsenal. This technique refers to three main approaches. Macroseeding is a technique that traditionally refers to the process of transferring small crystals or crystal fragments into a series of stabilizing wash solutions. After washing the small crystal it is transferred into a pre-equilibrated drop in order to grow the crystal larger (85, 161). Microseeding involves removing crystals from a drop, transferring them into a stabilizing solution and then crushing them and performing a dilution series of the crushed crystal seeds (86, 87). Seed solutions are then introduced into new crystallization drops using a probe in the hopes of growing larger or more ordered crystals. In both instances the aim is to take microcrystals or fragments from large crystals and seed them into a metastable supersaturated protein drop to provide nucleation sites while controlling growth.

Another approach to seeding is microseed matrix screening (MMS) which is becoming a popular technique due to its adaptability to robot crystallization tray setup (88, 89). MMS is performed first by setting up traditional commercially available screens and subsequently identifying crystals hits, likely of poor quality, to use as seeds. Low quality crystal hits are homogenized, pooled, and the resultant seeds are added to a new set of screening experiments, using the same screen from which the seeds were extracted. The challenge for this technique, however, is to adequately separate useful seeds from those that will have a deleterious effect on attempts to obtain higher quality crystals or are simply from a salt source that is indistinguishable from protein. Furthermore, this technique has only been proven useful with visible crystals and does not utilize precipitates.

In this work I present a method to generate nanometer-size seeds (nanoseeds) obtained from crystals or nanocrystals (NC) from granular aggregates; evaluate their quality by examining crystal lattices using TEM; and perform nanoseeding experiments to obtain large, high quality crystals for conventional X-ray diffraction experiments, or crystal catalogs, i.e., homogeneous sets of crystals of varying sizes for X-FEL and X-PP experiments.

5.2   RESULTS

5.2.1   Transmission Electron Microscopy of Protein Nanoseeds

Crystals of two macromolecular complexes refractory to conventional optimization protocols including precipitant and protein concentration, pH, temperature and additives were selected for micro-seeding experiments. Characteristically, crystals were small (<150 µm for PB-15 and <20 µm for PB-25 two unique RPBII complexes), lacked defined edges, diffracted to 8 Å and were highly mosaic. Brightfield microscopy analysis of crushed crystals using a 4 mm Teflon ball (Hampton Research) used for micro-seeding experiments revealed minimal and highly irregular crystal fragmentation (**Figure 28A**). Moreover, no lysis was observed for crystals in the low micrometer range (10-20 µm).
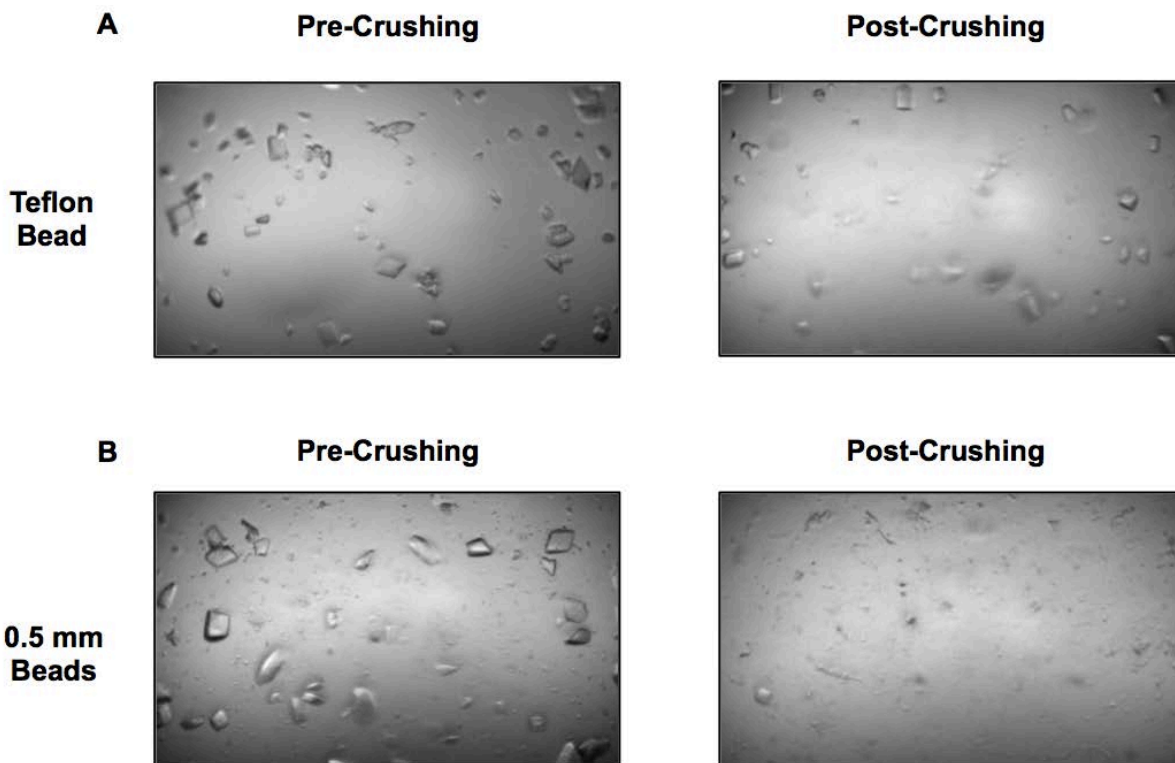
Figure 28. NCs before and after crushing with beads

A) Post crushing by the Teflon bead resulted in significantly less shearing than those crushed by B) the 0.5 mm beads.

In order to achieve better fragmentation we turned to lysis beads with lower diameters (0.5-1.0 mm) –routinely used for yeast lysis– and made of stainless steel –for easy removal with the use of a magnet. A single crystallization drop (2 µl volume) with over 30-50 crystals (ranging from 20-100 µm) was diluted 1:10 with 20 µl mother liquor and loaded into 1.5 ml Eppendorf tubes. Approximately 10 magnetic balls of 0.5 mm diameter were added to the crystal-mother liquor mixture and the tube was vortexed twice for 10 seconds; 2 µl of the resulting material were observed under brightfield microscopy (**Figure 28B, right panel**). This crystalline material (heretofore referred as nanoseeds) was homogeneous lysed and consisted of a large number of sub-micrometer particles with no identifiable faces or edges.
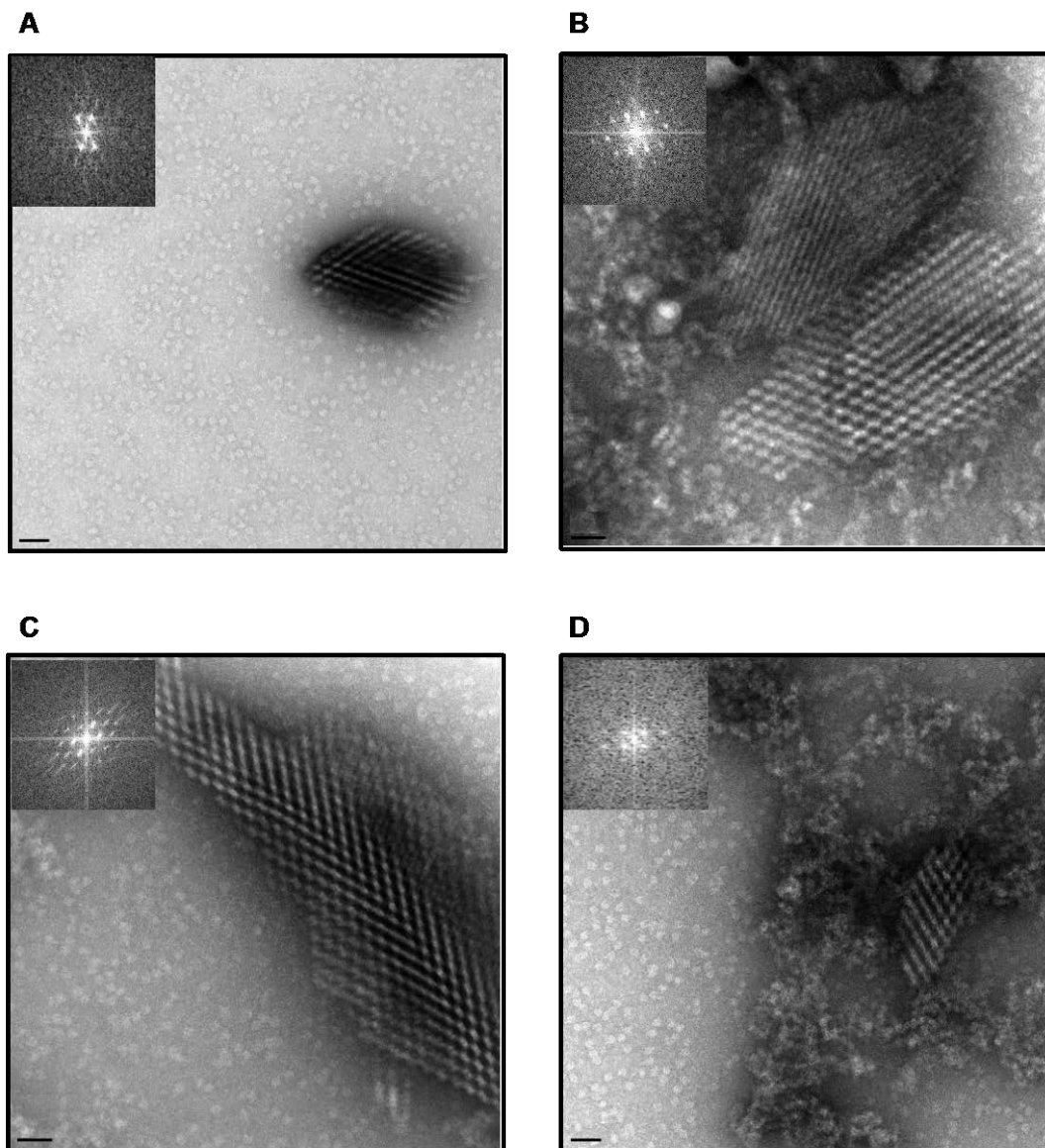
Figure 29. TEM images of RPBII-GFP nanocrystals crushed with 0.5 mm beads

A) Example of small nanoseed on top of a background of polymerase particles. B) Individual sheered lattices of RPBII -GFP. C) Nanoseed with clearly visible fracture lines (bottom right). D) Individual polymerase particles (left), protein filaments (middle) feeding into a small nanoseed (right).

Lastly, in order to verify that nanoseeds were not damaged during lysis, we set out to identify the presence of ordered lattices using transmission electron microscopy (TEM). Approximately 3-4 µl of nanoseed material were loaded onto carbon film copper grids (Electron Microscopy Sciences), blotted, negatively stained with 2% uranyl acetate (30 sec incubations) and air dried.

84

Sample grids were visualized using a T12 Tecnai electron microscope. Fragmented NCs were easily identified under TEM. Size and thickness of nanoseeds range from 70-2000 nm and from one to several layers respectively (**Figure 29**). By using slightly larger 1.0 mm beads, we were able to control the size of the seeds generated (**Figure 30**).
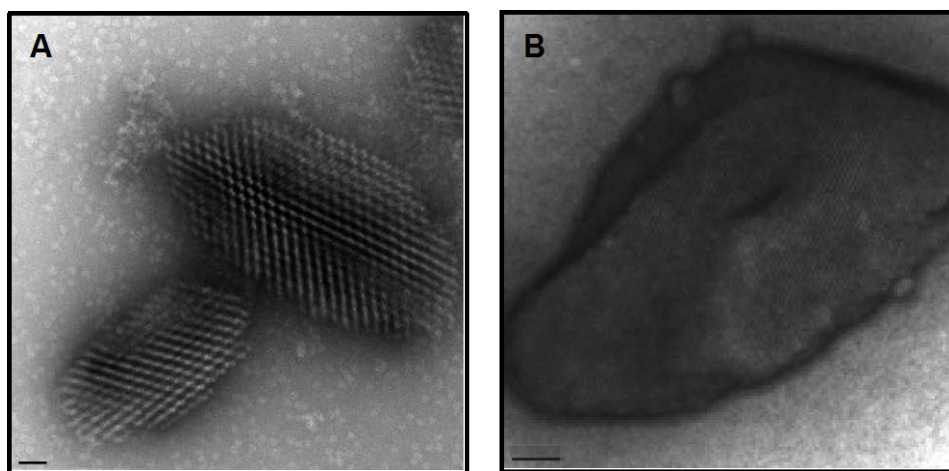
Figure 30. Evaluation of nanoseeds thickness by TEM

A) Nanoseeds with single planes of lattice generated by 0.5 mm beads. B) A nanoseed several layers thick generated by 1 mm beads.

Since crystalline lattices were clearly visualized with TEM, calculating Fourier transforms from the images allowed quantitative evaluation of electron diffraction patterns (Bragg spots) by selecting areas of the lattice. High quality lattices with two or higher order spots are evident in the reciprocal lattice reflections obtained by Fourier transform (**Figure 29, insets**). These results illustrate the potential use of TEM analysis of nanoseeds as a screening method to determine crystal quality.
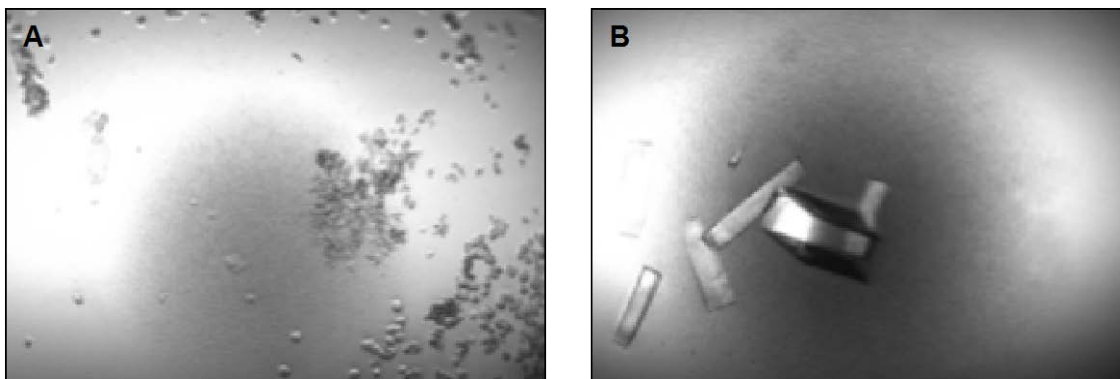
Figure 31. Comparison seeding optimization experiment set up with seeds produced by A) the Teflon bead verses B) 0.5 mm beads.

In addition to studying the shearing capacity of the Teflon beads vs. the 0.5 mm beads by brightfield and TEM, streak microseeding experiments were performed to compare the effectiveness of both types of seeds in generating crystals. Seeds were generated from the same source, which were relatively low quality crystals. As shown in **Figure 31**, significantly higher quality and larger size crystals were obtained from the 0.5 mm beads compared to the Teflon bead.

5.2.2 Nanoseeding Experiments Utilizing Visible Crystals

Once the high quality nature of the nanoseeds was confirmed, we set out to perform micro-seeding experiments using a nanoseed stock generated as described above. As shown in **Figure 32A**, small visible crystals were used to generate nanoseeds for this experiment. For nanoseeding experiments, conventional serial dilutions of the nanoseed stock (1:5, 1:25 and 1:125) were performed in order to fine-tune crystal size and quality. Nanoseeds were deposited on crystallization drops using a 0.3-0.4 millimeter cryo-loops (Hampton Research).

"Nanoseeded" crystal drops generated high quality crystals **(Figure 32).** X-ray diffraction experiments showed overall improvement of resolution and crystal mosaicity (**Figure 32, right panels**) as expected.
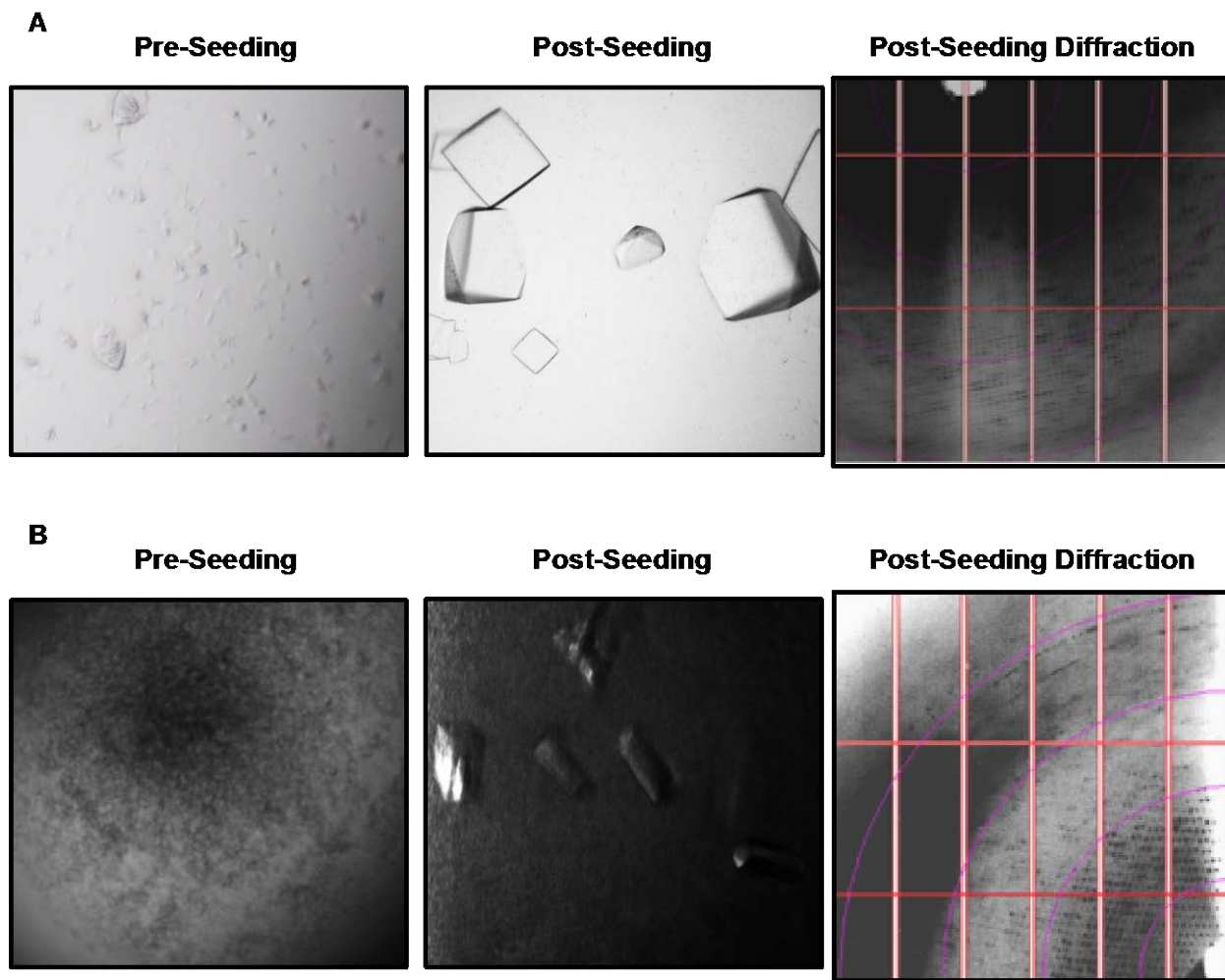
Figure 32. Brightfield images of pre and post seeding crystals, as well as post seeding diffraction

A) pb 15 visible crystals were used to generate nanoseeds. pb15 nanoseeded optimized crystals with diffraction of 3.6 Å. B) RPBII -CD3Delta nanocrystals optimized into visible crystals by nanoseeding. Diffraction up to 4.8Å

Since all samples in our study yielded large crystals by nanoseeding methods, TEM evaluation of seeds may not be necessary in all cases. As an alternative, in order to evaluate NC lysis efficiency, homogeneity and concentration, 2 µl of sample can be sealed between cover-slides

for bright- and UV-microscopy inspection. Examples of nanoseeds imaged using a Jansi UVEX microscope with a 40X objective are shown in **Figure 33.**
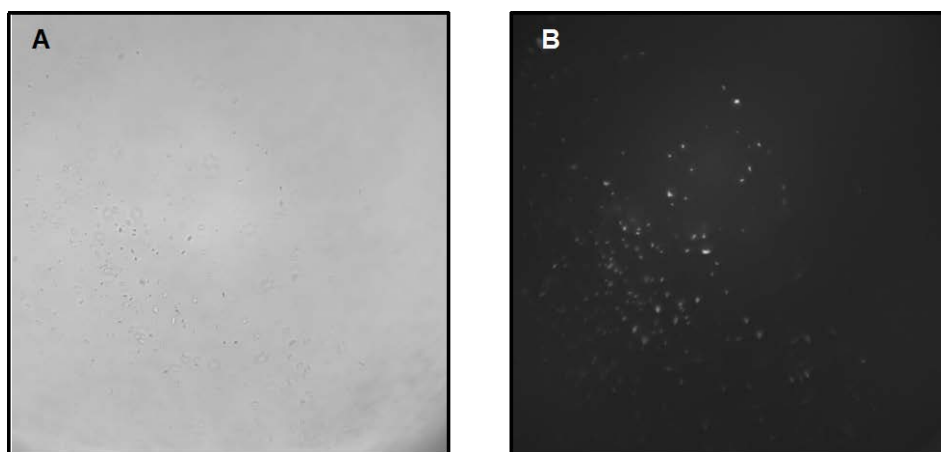
Figure 33. Nanoseeds, which required a 40X objective to detect by UV Tryptophan fluorescence

A) Brightfield and B) UV fluorescence image.

5.2.3 Nanoseeding Experiments Utilizing Nanocrystals

To detect the presence of NC in crystallization drops we followed the protocol described (137). Ultraviolet (UV) positive granular aggregates were selected for TEM imaging to confirm the presence of NCs. Crystallization conditions bearing NCs were subject to one round of optimization to improve NC size and/or quality and to generate larger amount of NCs for nanoseeding experiments. After the initial round of optimization, individual crystallization drops (1-2 µl) containing NCs were diluted 4X with mother liquor to a final volume of 10 µl and loaded into 200 µl PCR tubes containing 8-10 magnetic steel balls (0.5 mm diameter). Samples were vortexed twice for 10 sec. To allow use of all seeding material, magnetic balls were by removed by holding a magnet against the side of the tube. To corroborate proper fragmentation

and size homogeneity, samples were evaluated with brightfield and UV microscopy before and after being lysed (**Figure 34**).
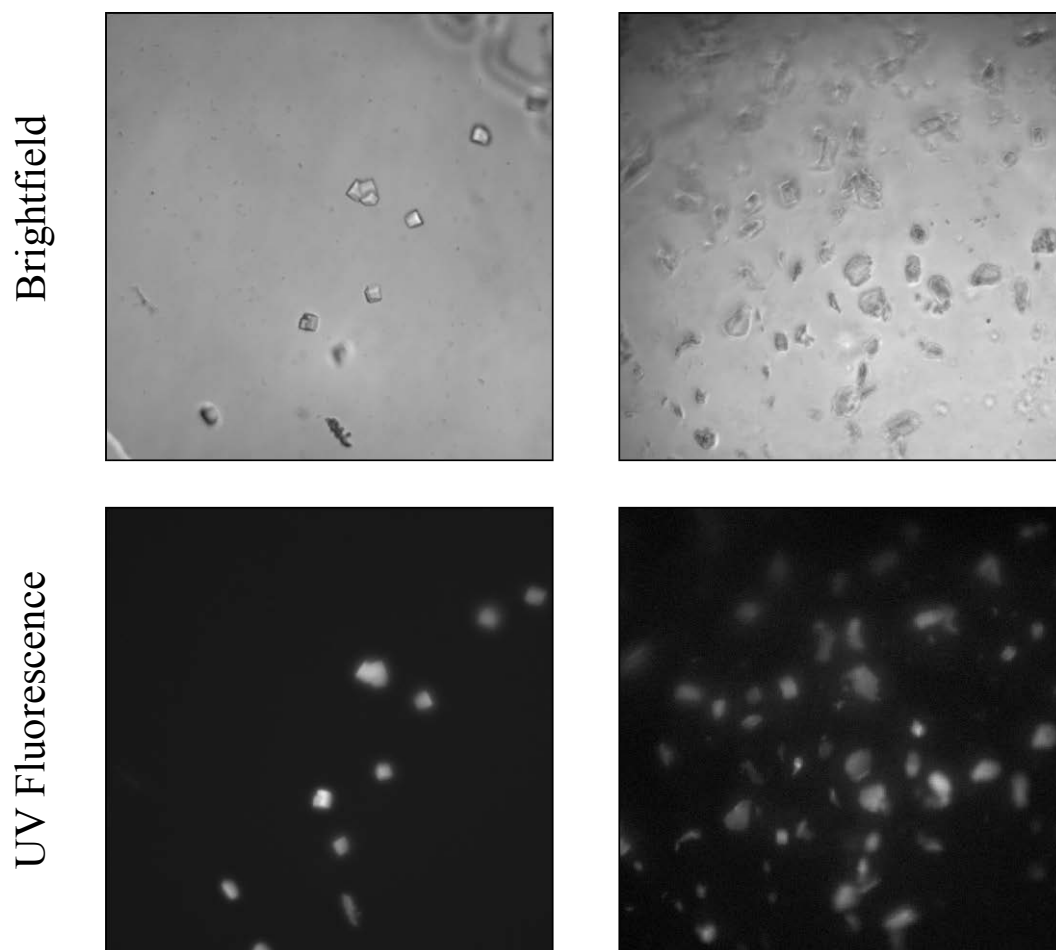
Figure 34. 40X objective images of brightfield UV tryptophan fluorescence of pb25 nanocrystals before A) and after B) 0.5 mm bead nanoseeds generation

Due to the presence of aggregates in the sample, observation of a UV signal was of paramount importance to allow qualitative estimate of nanoseed concentration**.** Seeding experiments were performed using nanoseeds slurries, and no serial dilutions were made for these samples since concentration of nanoseeds is typically low. Nanoseeded crystal drops generated high quality

crystals from granular precipitates (**Figure 32B**). X-ray diffraction experiments showed overall improvement of resolution and crystal mosaicity (**Figure 32B right panel**).

In addition to nanoseeding being a useful initial step for obtaining higher quality crystals or simply optimizing NC into visible crystals, this technique is useful for a sequential seeding optimization approach. As shown in **Figure 35** nanoseeding was an excellent technique for generating large diffractable crystals of this candidate from crystals that were previously to small and low quality for x-ray diffraction.
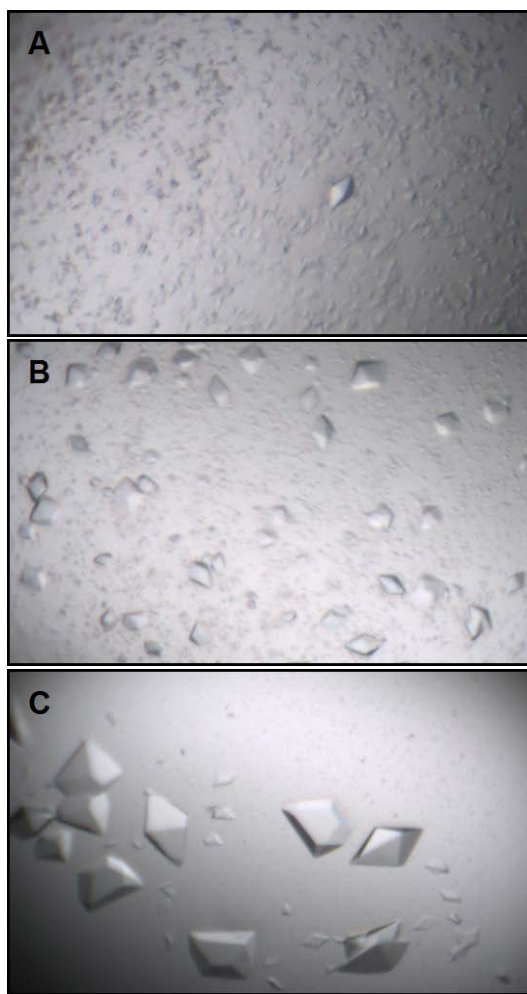
Figure 35. Optimization of PolF by nanoseeding optimization experiments.

A) Starting material used for crushing by 0.5 mm beads. B) Initial round of optimization using the seeds generated using the 0.5 mm beads. C) Large visible crystals generated by B as starting material.

This optimization almost exclusively relied on multiple rounds of nanoseeding to obtain significantly higher quality crystals that could be used for diffraction experiments (**Figure 36**). Nanoseeding may provide a reliable shortcut for arduous optimization steps for many protein crystallographic targets or at the very least significantly enhance traditional optimization approaches.
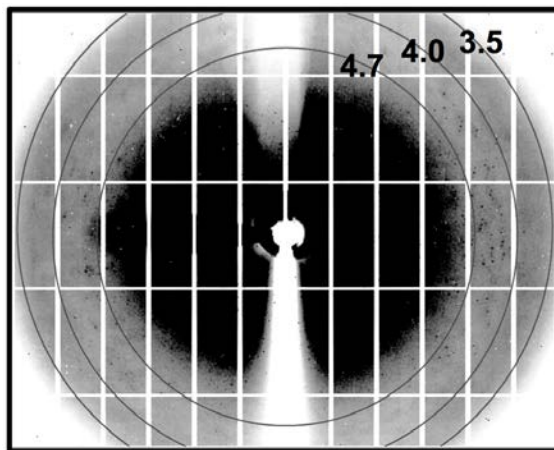
Figure 36. Diffraction up to 3.6 Å of pb25 after optimization by nanoseeding.

5.2.4   Generation of Crystal Catalogues for X-FEL Experiments

Given the advances provided by X-ray diffraction experiments using free electron lasers, it is very desirable to generate high quality and homogeneous population of NCs (heretofore referred as crystal catalogues) to be used for experiments at the Coherent X-ray Imaging (CXI) or X-ray Pump Probe (XPP) (>20 micrometers) facilities available at LCLS. Initially, we wished to explore the effects of using specifically quantified seed dilutions on crystal growth, seeded into varying precipitant to sample dilutions. Seeds were quantified by injecting the seed sample into the counting chamber of a hemocytometer and taking 40X UV images. Seeds were manually

counted in imageJ. As shown in **Figure 37**, there was a distinct correlation between both the precipitant to sample dilution and the quantity of seeds used dilution.

Sample Conc to Precipitant
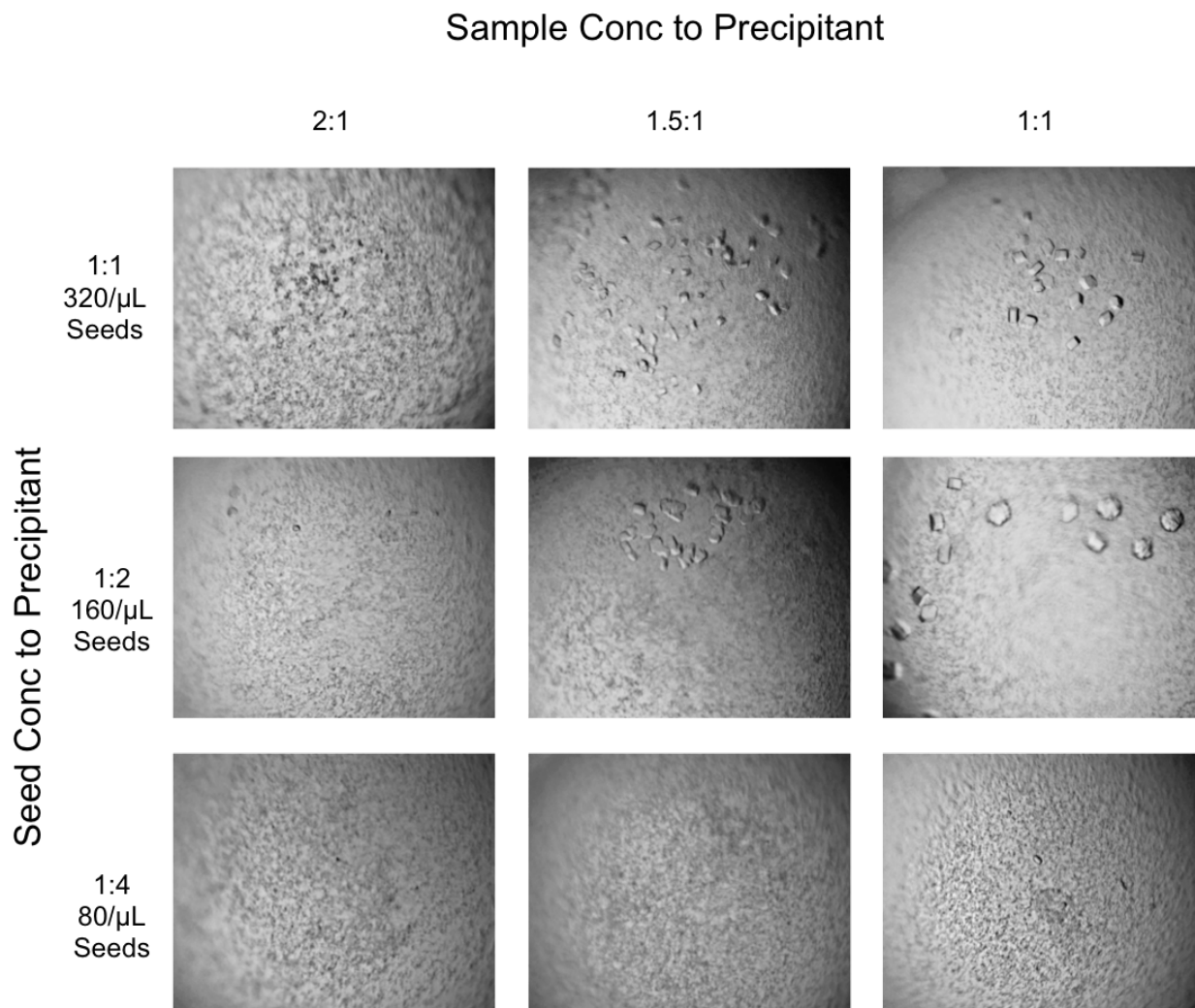
Figure 37. Effect of varying the precipitant to sample ratio with a decrease in seed concentration

With this in mind a protocol to generate crystal catalogues consisting of finely tuned crystal sizes was developed using nanoseeds. One to two drops with large numbers of crystals with sizes varying from 10-30 µm are diluted 30X with mother liquor and loaded into a 1.5 ml Eppendorf tube. Approximately 10 magnetic balls of 1.0 mm diameter are loaded into the tube and vortexed twice for 10 seconds followed by brightfield and UV inspection to corroborate lysis

efficiency and size of nanoseeds. A 1:3 dilution with mother liquor was performed with the

seeding stock. Crystal drops were set with different ratios of volumes of protein to precipitant

and seeded with equal amounts of nanoseeds from the seeding stock using a 0.3-0.4 millimeter

cryo-loops (Hampton Research). As expected, all seeded drops generated collections of

homogeneous crystal sizes (**Figure 7A**), while patterns were absent for non-seeded drops.
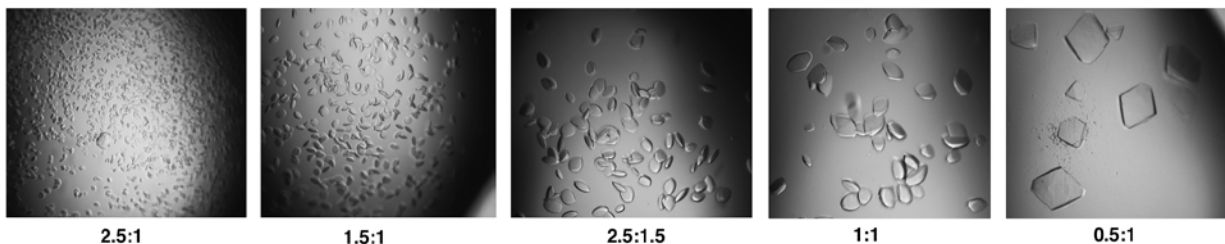
Figure 38. Crystal catalog showing crystals of homogenously size.

Refinement of crystal size was performed by varying the precipitant to protein ratio. In all cases the same
amount nanoseed slurry was added to the crystallization drop.

5.3   DISCUSSION

Crystal seeding has been traditionally part art, part science. Here we present the first study using

transmission electron microscopy of crystal seeds to develop a consistent methodology to

generate nanoseeds from nanocrystal slurries. The high quality of these nanoseeds was

corroborated using negative-stain TEM. Here we show that different sizes of seed lysis beads can

be used to produce different sized seeds that have significant consequences on the growth of

crystals by streak micro-seeding experiments. Nanoseeds were visualized directly by TEM. In all

instances examined, nanoseeds produced by 0.5 mm beads were of high quality, as indicated by

the evaluation of the FFT of the lattice. Use of nanoseeds were novel in four applications: 1) to produce improvements in crystal quality that could not be obtained through crystal condition optimization or traditional seeding. This was corroborated by x-ray diffraction data. 2) Nanoseeding of nanocrystals, not visible by brightfield microscopy and only identifiable by TEM, could be used in seeding experiments to produce visible crystals useful for traditional x-ray crystallography. 3) To produce higher quality nanocrystals, as in traditional seeding results, improvements of which were observed by TEM. 4) Nanoseed slurries of large crystals could be used to produce homogenous sized crystals of differing sizes. These results have important and useful applications for traditional and nanocrystallography, but also serves as a probe into the mechanism of seeding, a technique which, though powerful, is not fully understood.

The techniques presented here offer an essential understanding of the working of seeding as well as a means to obtain high quality crystals. However, it also provides a means to dictate the size of crystals. As the uses of nanocrystals with X-FEL to determine protein structure becomes more common, the ability to solve structures of crystals with a low threshold of radiation sensitivity becomes a significant benefit of this technique. This often means that large crystals must be "optimized down" to obtain high quality nanocrystals comparable with the current setups as CXI or XPP. This can be a tedious and unpredictable process, much like optimizing small crystals into larger ones. By applying the nanoseeding method, crystal size can be fine-tuned using a standardized amount of nanoseeds, seeded into varying ratios of protein to precipitant. Our results show that these experiments, when combined with nanoseed slurries, produce drops with homogenously sized crystals, which vary in size with the protein to precipitant ratio used.

5.4 METHODS

5.4.1 Protein Purification and Crystallography Condition Screening

RNA Polymerase (RPBII) and complex formation with RPBII was performed as described in (133) as was CD3Delta. TFIIF was purified as described in (135). Expression and purification of GFP was performed by standard methods (136). 2.5 M GFP or TFIIF was incubated with RPBII to assemble RPBII-GFP or RPBII-TFIIF. A Superdex 200 10/300 GL (50mM Hepes pH 7.5, 100mM KCl, 4mM DTT, 2mM $CaCl_2$ and 10μM $ZnCl_2$) was used to isolate the RPBII-GFP complex. Calmodulin-affinity chromatography was used to isolate RPBII-TFIIF.

Purification of CD3Delta and RPB 4-7 tagged with CBP were purified from *E. coli* as described in (133). CD3delta-CBP was stored in Buffer A (50 mM Tris-HCl pH 7.5, 600 mM NaCl, 0.5 mM C12E8), while RPB 4-7-CBP was stored in Buffer B (50 mM Tris-HCl pH 7.5, 150 mM KCl, 2 mM BME, 0.1 mM C12E8, and 2.5 mM $CaCl_2$)

In preparation of complex formation, both CD3delta and RBP 4-7 were incubated for 15 mins with after the addition of 2.5 mM CaCl2. All steps were performed at 4C. RBP 4-7 was then diluted 10X with buffer B before being combined with CD3delta and was incubated for 15 mins. The complex was then isolated on a Q-HP GE column in which the column was washed with 5 column volumes of Buffer A + 200 mM KCl. The complex was eluted in Buffer C (30 mM Tris-HCl pH 7.5, 600 mM KCl, 2 mM BME, 0.1 mM C12E8, and 2.5 mM CaCl2).

2.5 mM CaCl2 was added to Delta 4-7 Buffer D (30 mM Tris-HCl pH 7.5, 100 mM NaCl, 0.2X TEZ, 5 mM DTT, 0.1 mM C12E8, and 2.5 mM CaCl2) and incubated for 15 mins

before being mixed in an 1:0.6 ratio of Delta 4-7 to CD3delta-RBP 4-7 for 15 mins. This new complex was captured in the same way as the first and was dialyzed overnight in Buffer D.

To assemble an elongation complex (EC) for the purification of wild-type RPBII-nucleotide DNA/RNA scaffold-TFIIB complex (PB-25), 54-nts oligonucleotides containing a single stretch of 25 non-complimentary bases and a 5-mer RNA (complimentary to the template strand) were annealed above their melting temperatures and allowed to cool down slowly to 4 °C over a period of 5 hours. The resulting EC was incubated with *S. cerevisiae* 12-subunit RPBII (3:1 molar ratio) and excess EC was removed using size exclusion chromatography. TF2B was mixed with a RPBII-EC complex (3:1 molar ratio) in high salt buffer, removal of excess TF2B was carried out using a second size exclusion step in low salt buffer (50-100 mM).

Crystallization conditions for these proteins are as follows: RPBII-GFP: 6% PEG 8000, 0.1mM $MgCl_2$, 100mM Tris pH 8.0, 10mM DTT, 2mM $CaCl_2$. TFIIF: 8-12% PEG 400, 100mM NaMalonate, 50 mM HEPES pH 7.0 and 10 mM DTT**.** RPBII-CD3Delta: 1.4 M NaMalonate, 10mM DTT, pH 6.0. PB25: 30-35% Tact mate, 100mM Hepes pH 7.0, 15mM DTT.

5.4.2 Brightfield and UV Tryptophan Screening

An Olympus SZX16 brightfield microscope fitted with a 2XPFC objective was used to screen crystallization drops for granular aggregates and visible crystals to be used for nanoseeding experiments. Granular aggregates and visible crystals that maybe used for nanoseeding experiments were screened with a Jansi UVEX microscope to determine if the sample was proteinaceous in nature. Image analysis was performed using the Jan Scientific CrystalDetect software.

5.4.3   Seed Bead Experiments

HR Teflon bead fragmentation was performed according to the manufacture's protocol. 1.0 and 0.5 mm bead fragmentation was performed using 10 beads of stainless steel (Jinan Hawaii Industry Manufacturing And Trading Co. Limited) in a 1.5 mL microcentrifuge tube. Sample from 1-5 crystallization drops were combined and diluted with precipitant solution sufficient to cover just about the glass beads. Beads and sample were vortexed on high two times and stored on ice until grid preparation

5.4.4   Seed Counting

To determine seed concentration, seeds were injected into the counting chamber of a glass hemocytometer covered by a thin, UB transparent cover slip (HR). UV tryptophan fluorescent images were acquired for 1-4 sec. Images were counted using the Cell Counter ImageJ plugin after the image threshold was adjusted.

6.0   DISCUSSION

This work seeks to determine whether elusive targets, such as the PTHR1, produce identifiable protein NCs in conventional crystallization trials. Chapter 2.0 demonstrates the challenges associated with crystallizing the PTHR1. However, as Chapter 3.0 clearly shows, NCs of elusive targets such as the PTHR1, along with seven other samples tested can be identified by TEM. Furthermore, by calculating the fast Fourier transform of the lattice, crystal quality can be evaluated. Chapter 4 takes the first look at what is occurring to NCs before they are delivered to the X-FEL beam. This chapter illustrates the need to optimize protein conditions in order to reduce fragility and provides a means for further optimization of the jet itself. In Chapter 5.0 I show that not only do fragmented seeds hold a great deal of crystal optimization potential, they can also serve as the link between NCs and large crystals. Together, the work presented in these chapters demonstrates that TEM visualization of representative NCs from all protein types can be identified, optimized, and used to produce structures of proteins of which no large crystal could be obtained previously.

I hypothesized that protein NCs can be identified in a variety of protein targets intended for crystallization experiments, including samples of soluble, membrane, and multiprotein complexes. To demonstrate the usefulness of this strategy, the difficult Family B GPCR target, the PTHR1, was purified and used in crystallization trials to generate potential NCs. These trials revealed that alternative strategies to those employed for the Family A GPCRs would be

necessary to obtain large crystals of the PTHR1. The experiments presented in Chapter 3.0 sought to determine a means to identify NCs, assess their prevalence within a sample, and evaluate NC quality. This study relied upon samples from a variety of challenging targets as test cases, including the PTHR1. Chapter 4.0 sought to look at the next step, in which NCs are actually utilized in nanocrystallography diffraction experiments. Specifically, I wished to study the effects of the gas dynamic virtual nozzle (GDVN) on NC morphology before they reached the laser beam, after they are ejected from the injector. To this end, the visualization power of TEM was employed to examine NCs pre- and post- jet. This was performed using three different protein types to determine if any of the morphological changes that occurred when NCs go through the injector were protein type dependent. Furthermore in Chapter 5.0 , the fragmentation protocol used in the original Chapter 3 study to identify protein lattices of thick NCs (as well as judge their quality) led to the discovery that these "nanoseeds" were much more effective in yielding large crystals than were traditional seeding methods. Experiments comparing the effectiveness of traditional seeding and nanoseeding were performed. These experiments showed that crystals from nanoseeds were visibly larger and produced higher resolution structures. This study also showed that nanocrystals themselves could be used as a source to produce nanoseeds and could actually generate visible crystals where only nanocrystals could be grown before. Additionally, trials were performed to determine if nanoseeds could be utilized to create finely tuned, homogenous crystals useful for nanocrystallography experiments. These experiments clearly demonstrate the utility of nanoseeds in modulating crystal size, providing a means to use both the GDVN and fixed goniometer setup at LCLS' X-ray Pump Probe facility that uses larger crystals.

In Chapter 2.0 conventional crystallization approaches were applied to crystallization trials of the PTHR1. However, despite applying crystallography techniques specific to GPCR, crystallization, trials did not yield large crystals. Included in these trials were protein modifications aimed at stabilizing the receptor, based on successful strategies used for crystallizing other GPCRs. Though no large crystals were obtained, these trials did produce protein NCs, as Chapter 3.0 reveals. Though these crystals are not yet of sufficient quality or concentration for X-FEL diffraction experiments, as illustrated in Chapter 4.0 they represent an exciting step forward for large protein crystallography. The obtained PTHR1 NCs represent the first full-length GPCR crystals described to date besides Rhodopsin/Opsin, which had small extracellular domains (49, 50). This development has exciting implications for the advantages of nanocrystallography over conventional crystallography. It suggests that in addition to being able to solve structures of challenging targets that were otherwise not of useful size, it is possible that more daring crystallization constructs could be used to obtain NCs (which otherwise could not grow large crystals) and subsequently use them to solve more complete structures by X-FEL.

To successfully obtain crystals of the PTHR1, however, strategies need to focus on PTHR1 optimization that precedes the crystallization effort altogether. The PTHR1 was expressed in bacteria. This is an uncommon means to protein production for GPCR crystallography (162). One concern that has been reported is that GPCRs expressed in *E. coli* may sometimes produce several different populations of the receptor. These range from low to high affinity ligand binding receptors (163-166). As a result it may be advantageous to more thoroughly screen potential expression systems and weigh protein expression against the functionality of the receptor. One possible approach is to perform a radioligand competition-binding assay to determine the Kd of PTHR1 expressed from various expression systems.

Furthermore, comparative melting temperature estimates could also be determined. To carry out the latter, radioligand binding assays could be performed after heating receptors produced from different expression systems. The amount of receptor still able to bind ligand can then be compared, following a similar protocol to that described in (64). This may be a useful approach to identify the best expression system for obtaining folded, functional PTHR1.

However, since NCs of the PTHR1 have already been obtained for the receptor, it may be of greatest utility to begin optimization with the NCs themselves. The trials in Chapter 4.0 suggest several necessary areas of improvement for PTHR1 NCs: 1) increase the abundance of NCs to obtain large volumes of NC slurry that are necessary to collect data; 2) follow the improvement of the NCs by optimizing conditions to overcome the low quality nature of the NC lattice; 3) reduce clogging, most likely caused by high surfactant levels in the NC slurry buffer; and 4) optimize NCs to reduce their fragility.

In the instance when only low concentration of crystals can be obtained, results shown in **Figure 38** and **Figure 37** demonstrate the power of utilizing nanocrystals as nanoseeds to obtain a higher concentration of crystals, and in many cases obtain visible crystals. This technique in combination with traditional crystallography optimization approaches may ultimately provide a means to increase NC concentration. These figures also show the utility of seed dilutions with protein to precipitant modifications, and may prove to be experiments that are useful for increasing concentrations of NCs. Additionally, the standard crystallographic approaches, which include increase protein concentration, precipitating agent and salt, will likely also be useful. The results of these trials may be followed by TEM to determine the value of these changes, if not visible by brightfield microscopy. This approach may also be practical for overcoming the poor quality of the PTHR1 lattices shown in Chapters 3.0 and 4.0 Furthermore, given the "disordered"

nature of the PTHR1 lattices focusing further on thermostabilizing and truncating the receptor may be a practical next step.

In Chapter 4.0 PTHR1 NCs were shown to be not yet useful for X-FEL diffraction experiments. In addition to the low concentration of the receptor's NCs, these crystals, and RPBII-GPF NCs to a lesser extent, demonstrated fragility of NCs in the face of the harsh conditions of the jet. Though jet optimization may prove to be the defining factor in NC survival, there are several possible approaches to overcome the above-mentioned challenges. In the case of the PTHR1 pure protein, further detergent minded DLS experiments could be performed to determine the absolute lowest detergent concentration that is necessary to keep the receptor monodispersed. Furthermore, it may be useful to screen surfactants themselves with the jet to determine the best candidates for use with membrane protein NCs to prevent clogging and destructive bubbling.

The fragility of NCs also decreases their probability of survival while going through the jet, and subsequently, the quality of the resolution that can be obtained. This inherent fragility of the crystals could be optimized in several ways. One of the most commonly applied methods to overcome crystal fragility is cross-linking. A cross-linking agent, such as 0.1% glutaraldehyde can be added directly to the drop or reservoir. Cross-linking has also been shown to be useful for preventing lattice disorder, such as the lattice disorder observed in PTHR1 NCs (167-169). Dehydration is another post-crystallization treatment that is thought to circumvent the problems associated with crystals with large solvent content and loosely packed molecules (169, 170). This technique may also be a potential approach to overcome the low threshold of fragility required by current nanocrystallography approaches.

The investigation into the damage caused by the jet to NCs was assessed for the first time in Chapter 4.0 . However, despite the novelty of this study it must be extended further to obtain more conclusive results of how the jet impacts different crystal types. Furthermore, only NC samples that can be obtained at the same concentration (and can subsequently be diluted in the same manner) should be compared in future work. This method will help to distinguish between damage, loss in concentration, and clogging that result from the interaction of the GDVN, on one hand, and the properties of the crystals and buffers themselves on the other.

The approach followed in Chapter 4.0 could also be used as a powerful method to optimize the technique of GDVN itself. Representative proteins could be tested in the same way as described above to evaluate the pre- and post- TEM images of NCs. This may be important, as loss of concentration can already be estimated, but the damage done to crystal cannot presently be evaluated, without the application of the TEM visualization method presented here, which limits the optimization of the jet delivery system. TEM may even reveal an association of NC disruption depending on the morphology of the crystal along with its protein type.

In Chapter 3.0 I sought to develop a method for rapidly identifying protein nanocrystals as well as a means to characterize and evaluate the identified NCs. This method is meant to be broadly applicable to many laboratory environments. However, in some instances, use of this technique maybe limited by the equipment available to a particular lab. For example, without UV tryptophan fluorescence microscopy in conjunction with brightfield microscopy it would be extremely difficult to distinguish between protein and salt precipitate. There are, however, other possible routes to pare down the number of samples used for TEM analysis. One laborious option would be to setup, in parallel, two drops for each condition and label one drop with Izit dye to distinguish between protein which would turn blue or non-labeled salt. As described in

Chapter 3.0 DLS can also be utilized as a pre-screening method to determine if precipitates contain species with appropriate NC diameter. However, another application of DLS could be utilized when equipment resources are scarce but a DLS instrument is readily available. Dierks et al. (171) adapted DLS to monitor protein nucleation and growth, and, in the process to distinguish between amorphous and crystalline species. This method could be useful when other pre-screening TEM approaches are not possible. However, this experiment follows newly setup crystallography drops over time in order to distinguish between aggregates and crystalline species. As such, this method may not be ideal for screening an exhaustive number of trays and may likely only be used for screening long after the crystallographer has given up hope of obtaining large crystal hits from these experiments.

Another means of increasing the high-throughput nature of the method presented in Chapter 3.0 is to focus on TEM itself. The FEI Tecnai T12 microscope that was used in these studies has a single tilt, side loader sample setup. Changing between samples can take up to 7 minutes, including microscope adjustment time. This can significantly inhibit the number of samples that can be screened per protein. There are advances in sample holder technology, however, that may increase the speed at which samples can be assessed. One example, which is still uncommon amongst non-cryo- TEM microscopes, includes multi-sample holders that reduce sample-changing time. Automated sample screening and image acquisition when paired with image recognition geared at lattice recognition may be also employed in the future. These improvements will allow crystallographers to screen samples rapidly to identify more quickly those hits worthy of further optimization.

The NC fragmentation protocol developed in Chapter 5.0 has implications beyond the advances it provides as an excellent source of seeds. In **Figure 30** there is a comparison of the

resultant seeds by 0.5 and 1 mm lysis beads. The size of the 1 mm bead generated seeds is an ideal size for solving structure of 3D NCs by cryo-EM. Only one such structure has been reported, that of lysozyme to 2.9Å (107). One of the challenges that the authors faced was isolating crystals of the necessary size, which they found to be no thicker than 0.5 μm. And indeed, it is expected that this will be a challenge in future structure resolution by this same method with other protein NCs. The nanoseed protocol presented in Chapter 5.0 then, may provide an exciting route to increase the number of such structures by crushing crystals to the appropriate size for electron diffraction.

X-FEL nanocrystallography provides a new avenue to solve crystal structures by X-ray diffraction of nano-meter sized crystals. These innovations open the door to obtaining atomic information from samples whose intrinsic disorder prevents the formation of large crystals. However, approaches to identify protein NCs suitable for diffraction by a X-FEL were not available prior to this work. Moreover, X-FEL structures solved to date were comprised mainly of NCs that had been previously solved by conventional X-ray crystallography methods. As a result, X-FEL experiments had yet to be employed to solve structures of challenging targets that only yield NCs. By examining crystallization drops with negative stain transmission electron microscopy (TEM), I have shown that NCs can be identified from all samples tested, which include representative proteins from a diverse population of challenging targets. In addition to this discovery, the application of TEM to NC visualization led to other novel findings. This method provided the first means to study the damage inflicted on NCs by the X-FEL NC delivery system, the GDVN. These studies showed that the GDVN produced different degrees of damage depending on the protein NC type. An additional investigation using TEM allowed for the first visualization of crystallographic seeds. These seed studies demonstrate that fragmented

NCs are powerful tools for optimizing and growing crystals. Taken together, the sum of this work provides a way not only to solve structures from challenging targets where large crystals could not be obtained, but also test whether these NCs could even survive X-FEL diffraction experiments prior to testing during expensive LCLS time. Furthermore this work provides a means to turn the NCs identified in Chapter 3.0 into nanoseeds, which can be used to grow large crystals from NCs.

ABBREVIATIONS

GPCR	G-Protein Coupled Receptor
HGP	Heterotrimeric G protein
ECD	Extracellular domain
ILC	Intracellular loop
βAR	β adrenergic receptor
PTHR1	Parathyroid hormone receptor type 1
NC	Nanocrystal
CRHR1	Corticotropin releasing factor receptor type 1
GCGR	Glucagon receptor
PTHR-480s	C-term PTHR truncation at residue 480s
K-PTHR	Replaced flexible ECD loop with Ser-Gly linker
PTHR-ICL3	Replaced ICL3 of PTHR1 with Ser-Gly linker
RPBII	RNA polymerase II
CPM	N-[4-(7diethylamino-4methyl-3 coumarinyl)phenyl]maleimide
TEM	Transmission electron microscopy
FFT	Fast Fourier transform
DLS	Dynamic light scattering

BIBLIOGRAPHY

1. Overington JP, Al-Lazikani B, Hopkins AL. How many drug targets are there? Nat Rev Drug Discov. 2006;5(12):993-6.
2. Drews J. Drug discovery: a historical perspective. Science. 2000;287(5460):1960-4.
3. Gether U. Uncovering molecular mechanisms involved in activation of G protein-coupled receptors. Endocr Rev. 2000;21(1):90-113.
4. Pierce KL, Premont RT, Lefkowitz RJ. Seven-transmembrane receptors. Nat Rev Mol Cell Biol. 2002;3(9):639-50.
5. Ames RS, Sarau HM, Chambers JK, Willette RN, Aiyar NV, Romanic AM, et al. Human urotensin-II is a potent vasoconstrictor and agonist for the orphan receptor GPR14. Nature. 1999;401(6750):282-6.
6. Kehrl JH. Heterotrimeric G protein signaling: roles in immune function and fine-tuning by RGS proteins. Immunity. 1998;8(1):1-10.
7. Rothenberg ME, Zimmermann N, Mishra A, Brandt E, Birkenberger LA, Hogan SP, et al. Chemokines and chemokine receptors: their role in allergic airway disease. J Clin Immunol. 1999;19(5):250-65.
8. Banerjee SP, Kung LS, Riggi SJ, Chanda SK. Development of beta-adrenergic receptor subsensitivity by antidepressants. Nature. 1977;268(5619):455-6.
9. Pandey GN, Dysken MW, Garver DL, Davis JM. Beta-adrenergic receptor function in affective illness. Am J Psychiatry. 1979;136(5):675-8.
10. Araneda RC, Kini AD, Firestein S. The molecular receptive range of an odorant receptor. Nat Neurosci. 2000;3(12):1248-55.
11. Abe K, Kusakabe Y, Tanemura K, Emori Y, Arai S. Primary structure and cell-type specific expression of a gustatory G protein-coupled receptor related to olfactory receptors. J Biol Chem. 1993;268(16):12033-9.
12. Yudkin AM. The Presence of Vitamin A in the Retina. Trans Am Ophthalmol Soc. 1931;29:263-72. PMCID: 1316806.
13. Towner P, Gaertner W, Walckhoff B, Oesterhelt D, Hopf H. Regeneration of rhodopsin and bacteriorhodopsin. The role of retinal analogues as inhibitors. Eur J Biochem. 1981;117(2):353-9.
14. Lagerstrom MC, Schioth HB. Structural diversity of G protein-coupled receptors and significance for drug discovery. Nat Rev Drug Discov. 2008;7(4):339-57.
15. Venkatakrishnan AJ, Deupi X, Lebon G, Tate CG, Schertler GF, Babu MM. Molecular signatures of G-protein-coupled receptors. Nature. 2013;494(7436):185-94.
16. Strader CD, Sigal IS, Register RB, Candelore MR, Rands E, Dixon RA. Identification of residues required for ligand binding to the beta-adrenergic receptor. Proc Natl Acad Sci U S A. 1987;84(13):4384-8. PMCID: 305093.

17.   Strader CD, Candelore MR, Hill WS, Sigal IS, Dixon RA. Identification of two serine residues involved in agonist activation of the beta-adrenergic receptor. J Biol Chem. 1989;264(23):13572-8.
18.   Liapakis G, Ballesteros JA, Papachristou S, Chan WC, Chen X, Javitch JA. The forgotten serine. A critical role for Ser-2035.42 in ligand binding to and activation of the beta 2-adrenergic receptor. J Biol Chem. 2000;275(48):37779-88.
19.   Jiang Q, Guo D, Lee BX, Van Rhee AM, Kim YC, Nicholas RA, et al. A mutational analysis of residues essential for ligand recognition at the human P2Y1 receptor. Mol Pharmacol. 1997;52(3):499-507. PMCID: 3425637.
20.   Laburthe M, Couvineau A, Marie JC. VPAC receptors for VIP and PACAP. Receptors Channels. 2002;8(3-4):137-53.
21.   Gether U, Asmar F, Meinild AK, Rasmussen SG. Structural basis for activation of G-protein-coupled receptors. Pharmacol Toxicol. 2002;91(6):304-12.
22.   Graul RC, Sadee W. Evolutionary relationships among G protein-coupled receptors using a clustered database approach. Aaps Pharmsci. 2001;3(2).
23.   Harmar AJ. Family-B G-protein-coupled receptors. Genome Biol. 2001;2(12):REVIEWS3013. PMCID: 138994.
24.   Josefsson LG. Evidence for kinship between diverse G-protein coupled receptors. Gene. 1999;239(2):333-40.
25.   Laburthe M, Couvineau A, Gaudin P, Maoret JJ, Rouyer-Fessard C, Nicole P. Receptors for VIP, PACAP, secretin, GRF, glucagon, GLP-1, and other members of their new family of G protein-linked receptors: structure-function relationship with special reference to the human VIP-1 receptor. Ann N Y Acad Sci. 1996;805:94-109; discussion 10-1.
26.   Hoare SR. Mechanisms of peptide and nonpeptide ligand binding to Class B G-protein-coupled receptors. Drug Discov Today. 2005;10(6):417-27.
27.   Horn F, Bywater R, Krause G, Kuipers W, Oliveira L, Paiva AC, et al. The interaction of class B G protein-coupled receptors with their hormones. Receptors Channels. 1998;5(5):305-14.
28.   Laburthe M, Couvineau A, Tan V. Class II G protein-coupled receptors for VIP and PACAP: structure, models of activation and pharmacology. Peptides. 2007;28(9):1631-9.
29.   Brauner-Osborne H, Jensen AA, Sheppard PO, O'Hara P, Krogsgaard-Larsen P. The agonist-binding domain of the calcium-sensing receptor is located at the amino-terminal domain. J Biol Chem. 1999;274(26):18382-6.
30.   Hammerland LG, Krapcho KJ, Garrett JE, Alasti N, Hung BC, Simin RT, et al. Domains determining ligand specificity for Ca2+ receptors. Mol Pharmacol. 1999;55(4):642-8.
31.   Bettler B, Kaupmann K, Mosbacher J, Gassmann M. Molecular structure and physiological functions of GABA(B) receptors. Physiol Rev. 2004;84(3):835-67.
32.   Cheng Y, Lotan R. Molecular cloning and characterization of a novel retinoic acid-inducible gene that encodes a putative G protein-coupled receptor. J Biol Chem. 1998;273(52):35008-15.
33.   Ray K, Hauschild BC, Steinbach PJ, Goldsmith PK, Hauache O, Spiegel AM. Identification of the cysteine residues in the amino-terminal extracellular domain of the human Ca(2+) receptor critical for dimerization. Implications for function of monomeric Ca(2+) receptor. J Biol Chem. 1999;274(39):27642-50.
34.   O'Hara PJ, Sheppard PO, Thogersen H, Venezia D, Haldeman BA, McGrane V, et al. The ligand-binding domain in metabotropic glutamate receptors is related to bacterial periplasmic binding proteins. Neuron. 1993;11(1):41-52.

35.   Costantino G, Pellicciari R. Homology modeling of metabotropic glutamate receptors. (mGluRs) structural motifs affecting binding modes and pharmacological profile of mGluR1 agonists and competitive antagonists. J Med Chem. 1996;39(20):3998-4006.

36.   Kunishima N, Shimada Y, Tsuji Y, Sato T, Yamamoto M, Kumasaka T, et al. Structural basis of glutamate recognition by a dimeric metabotropic glutamate receptor. Nature. 2000;407(6807):971-7.

37.   Tsuchiya D, Kunishima N, Kamiya N, Jingami H, Morikawa K. Structural views of the ligand-binding cores of a metabotropic glutamate receptor complexed with an antagonist and both glutamate and Gd3+. Proc Natl Acad Sci U S A. 2002;99(5):2660-5. PMCID: 122404.

38.   Romano C, Yang WL, O'Malley KL. Metabotropic glutamate receptor 5 is a disulfide-linked dimer. J Biol Chem. 1996;271(45):28612-6.

39.   Gether U, Ballesteros JA, Seifert R, Sanders-Bush E, Weinstein H, Kobilka BK. Structural instability of a constitutively active G protein-coupled receptor. Agonist-independent activation due to conformational flexibility. J Biol Chem. 1997;272(5):2587-90.

40.   Leurs R, Smit MJ, Alewijnse AE, Timmerman H. Agonist-independent regulation of constitutively active G-protein-coupled receptors. Trends Biochem Sci. 1998;23(11):418-22.

41.   Ango F, Prezeau L, Muller T, Tu JC, Xiao B, Worley PF, et al. Agonist-independent activation of metabotropic glutamate receptors by the intracellular protein Homer. Nature. 2001;411(6840):962-5.

42.   Hurowitz EH, Melnyk JM, Chen YJ, Kouros-Mehr H, Simon MI, Shizuya H. Genomic characterization of the human heterotrimeric G protein alpha, beta, and gamma subunit genes. DNA Res. 2000;7(2):111-20.

43.   Strathmann MP, Simon MI. G alpha 12 and G alpha 13 subunits define a fourth class of G protein alpha subunits. Proc Natl Acad Sci U S A. 1991;88(13):5582-6. PMCID: 51921.

44.   Rasmussen SG, Choi HJ, Fung JJ, Pardon E, Casarosa P, Chae PS, et al. Structure of a nanobody-stabilized active state of the beta(2) adrenoceptor. Nature. 2011;469(7329):175-80. PMCID: 3058308.

45.   Rasmussen SG, DeVree BT, Zou Y, Kruse AC, Chung KY, Kobilka TS, et al. Crystal structure of the beta2 adrenergic receptor-Gs protein complex. Nature. 2011;477(7366):549-55. PMCID: 3184188.

46.   Neves SR, Ram PT, Iyengar R. G protein pathways. Science. 2002;296(5573):1636-9.

47.   Di Marzo V, Vial D, Sokoloff P, Schwartz JC, Piomelli D. Selection of alternative G-mediated signaling pathways at the dopamine D2 receptor by protein kinase C. J Neurosci. 1993;13(11):4846-53.

48.   Asrih M, Mach F, Nencioni A, Dallegri F, Quercioli A, Montecucco F. Role of mitogen-activated protein kinase pathways in multifactorial adverse cardiac remodeling associated with metabolic syndrome. Mediators Inflamm. 2013;2013:367245. PMCID: 3556856.

49.   Scheerer P, Park JH, Hildebrand PW, Kim YJ, Krauss N, Choe HW, et al. Crystal structure of opsin in its G-protein-interacting conformation. Nature. 2008;455(7212):497-502.

50.   Palczewski K, Kumasaka T, Hori T, Behnke CA, Motoshima H, Fox BA, et al. Crystal structure of rhodopsin: A G protein-coupled receptor. Science. 2000;289(5480):739-45.

51.   Park JH, Scheerer P, Hofmann KP, Choe HW, Ernst OP. Crystal structure of the ligand-free G-protein-coupled receptor opsin. Nature. 2008;454(7201):183-7.

52.   Rasmussen SG, Choi HJ, Rosenbaum DM, Kobilka TS, Thian FS, Edwards PC, et al. Crystal structure of the human beta2 adrenergic G-protein-coupled receptor. Nature. 2007;450(7168):383-7.

53.   Cherezov V, Rosenbaum DM, Hanson MA, Rasmussen SG, Thian FS, Kobilka TS, et al. High-resolution crystal structure of an engineered human beta2-adrenergic G protein-coupled receptor. Science. 2007;318(5854):1258-65. PMCID: 2583103.

54.   Haga K, Kruse AC, Asada H, Yurugi-Kobayashi T, Shiroishi M, Zhang C, et al. Structure of the human M2 muscarinic acetylcholine receptor bound to an antagonist. Nature. 2012;482(7386):547-51. PMCID: 3345277.

55.   Shimamura T, Shiroishi M, Weyand S, Tsujimoto H, Winter G, Katritch V, et al. Structure of the human histamine H1 receptor complex with doxepin. Nature. 2011;475(7354):65-70. PMCID: 3131495.

56.   Chien EY, Liu W, Zhao Q, Katritch V, Han GW, Hanson MA, et al. Structure of the human dopamine D3 receptor in complex with a D2/D3 selective antagonist. Science. 2010;330(6007):1091-5. PMCID: 3058422.

57.   Xu F, Wu H, Katritch V, Han GW, Jacobson KA, Gao ZG, et al. Structure of an agonist-bound human A2A adenosine receptor. Science. 2011;332(6027):322-7. PMCID: 3086811.

58.   Wu B, Chien EY, Mol CD, Fenalti G, Liu W, Katritch V, et al. Structures of the CXCR4 chemokine GPCR with small-molecule and cyclic peptide antagonists. Science. 2010;330(6007):1066-71. PMCID: 3074590.

59.   Wu H, Wacker D, Mileni M, Katritch V, Han GW, Vardy E, et al. Structure of the human kappa-opioid receptor in complex with JDTic. Nature. 2012;485(7398):327-32. PMCID: 3356457.

60.   Hanson MA, Roth CB, Jo E, Griffith MT, Scott FL, Reinhart G, et al. Crystal structure of a lipid G protein-coupled receptor. Science. 2012;335(6070):851-5. PMCID: 3338336.

61.   Warne T, Serrano-Vega MJ, Baker JG, Moukhametzianov R, Edwards PC, Henderson R, et al. Structure of a beta1-adrenergic G-protein-coupled receptor. Nature. 2008;454(7203):486-91. PMCID: 2923055.

62.   Serrano-Vega MJ, Magnani F, Shibata Y, Tate CG. Conformational thermostabilization of the beta1-adrenergic receptor in a detergent-resistant form. Proc Natl Acad Sci U S A. 2008;105(3):877-82. PMCID: 2242685.

63.   Magnani F, Shibata Y, Serrano-Vega MJ, Tate CG. Co-evolving stability and conformational homogeneity of the human adenosine A2a receptor. Proc Natl Acad Sci U S A. 2008;105(31):10744-9. PMCID: 2504806.

64.   Lebon G, Bennett K, Jazayeri A, Tate CG. Thermostabilisation of an agonist-bound conformation of the human adenosine A(2A) receptor. J Mol Biol. 2011;409(3):298-310. PMCID: 3145977.

65.   Ericsson UB, Hallberg BM, Detitta GT, Dekker N, Nordlund P. Thermofluor-based high-throughput stability optimization of proteins for structural studies. Anal Biochem. 2006;357(2):289-98.

66.   Pantoliano MW, Petrella EC, Kwasnoski JD, Lobanov VS, Myslik J, Graf E, et al. High-density miniaturized thermal shift assays as a general strategy for drug discovery. J Biomol Screen. 2001;6(6):429-40.

67.   Vedadi M, Niesen FH, Allali-Hassani A, Fedorov OY, Finerty PJ, Jr., Wasney GA, et al. Chemical screening methods to identify ligands that promote protein stability, protein crystallization, and structure determination. Proc Natl Acad Sci U S A. 2006;103(43):15835-40. PMCID: 1595307.

68.   Yeh AP, McMillan A, Stowell MH. Rapid and simple protein-stability screens: application to membrane proteins. Acta Crystallogr D Biol Crystallogr. 2006;62(Pt 4):451-7.

69.   Alexandrov AI, Mileni M, Chien EY, Hanson MA, Stevens RC. Microscale fluorescent thermal stability assay for membrane proteins. Structure. 2008;16(3):351-9.
70.   Rosenbaum DM, Zhang C, Lyons JA, Holl R, Aragao D, Arlow DH, et al. Structure and function of an irreversible agonist-beta(2) adrenoceptor complex. Nature. 2011;469(7329):236-40. PMCID: 3074335.
71.   Juppner H, Abou-Samra AB, Freeman M, Kong XF, Schipani E, Richards J, et al. A G protein-linked receptor for parathyroid hormone and parathyroid hormone-related peptide. Science. 1991;254(5034):1024-6.
72.   Tregear GW, Van Rietschoten J, Greene E, Keutmann HT, Niall HD, Reit B, et al. Bovine parathyroid hormone: minimum chain length of synthetic peptide required for biological activity. Endocrinology. 1973;93(6):1349-53.
73.   Pioszak AA, Xu HE. Molecular recognition of parathyroid hormone by its G protein-coupled receptor. Proc Natl Acad Sci U S A. 2008;105(13):5034-9. PMCID: 2278174.
74.   Pioszak AA, Harikumar KG, Parker NR, Miller LJ, Xu HE. Dimeric arrangement of the parathyroid hormone receptor and a structural mechanism for ligand-induced dissociation. J Biol Chem. 2010;285(16):12435-44. PMCID: 2852981.
75.   Bisello A, Adams AE, Mierke DF, Pellegrini M, Rosenblatt M, Suva LJ, et al. Parathyroid hormone-receptor interactions identified directly by photocross-linking and molecular modeling studies. J Biol Chem. 1998;273(35):22498-505.
76.   Bergwitz C, Gardella TJ, Flannery MR, Potts JT, Jr., Kronenberg HM, Goldring SR, et al. Full activation of chimeric receptors by hybrids between parathyroid hormone and calcitonin. Evidence for a common pattern of ligand-receptor interaction. J Biol Chem. 1996;271(43):26469-72.
77.   Hoare SR, Gardella TJ, Usdin TB. Evaluating the signal transduction mechanism of the parathyroid hormone 1 receptor. Effect of receptor-G-protein interaction on the ligand binding mechanism and receptor conformation. J Biol Chem. 2001;276(11):7741-53.
78.   Liu W, Wacker D, Gati C, Han GW, James D, Wang D, et al. Serial femtosecond crystallography of G protein-coupled receptors. Science. 2013;342(6165):1521-4. PMCID: 3902108.
79.   Grigorieff N, Ceska TA, Downing KH, Baldwin JM, Henderson R. Electron-crystallographic refinement of the structure of bacteriorhodopsin. J Mol Biol. 1996;259(3):393-421.
80.   Henderson R, Baldwin JM, Ceska TA, Zemlin F, Beckmann E, Downing KH. Model for the structure of bacteriorhodopsin based on high-resolution electron cryo-microscopy. J Mol Biol. 1990;213(4):899-929.
81.   Pusey ML, Paley MS, Turner MB, Rogers RD. Protein Crystallization Using Room Temperature Ionic Liquids. Crystal Growth & Design. 2007;7(4):787-93.
82.   Summers CA, Flowers RA, 2nd. Protein renaturation by the liquid organic salt ethylammonium nitrate. Protein Sci. 2000;9(10):2001-8. PMCID: 2144456.
83.   Lange C, Patil G, Rudolph R. Ionic liquids as refolding additives: N'-alkyl and N'-(omega-hydroxyalkyl) N-methylimidazolium chlorides. Protein Sci. 2005;14(10):2693-701. PMCID: 2253306.
84.   Richards.Dc, Richards.Js, Bier CJ. Two Crystal Forms of Bovine Superoxide Dismutase. Journal of Biological Chemistry. 1972;247(19):6368-&.
85.   Thaller C, Weaver LH, Eichele G, Wilson E, Karlsson R, Jansonius JN. Repeated seeding technique for growing large single crystals of proteins. J Mol Biol. 1981;147(3):465-9.

86.   McPherson A, Jr. The growth and preliminary investigation of protein and nucleic acid crystals for X-ray diffraction analysis. Methods Biochem Anal. 1976;23(0):249-345.

87.   Stura EA, Wilson IA. Applications of the Streak Seeding Technique in Protein Crystallization. J Cryst Growth. 1991;110(1-2):270-82.

88.   D'Arcy A, Villard F, Marsh M. An automated microseed matrix-screening method for protein crystallization. Acta Crystallogr D Biol Crystallogr. 2007;63(Pt 4):550-4.

89.   Ireton GC, Stoddard BL. Microseed matrix screening to improve crystals of yeast cytosine deaminase. Acta Crystallogr D Biol Crystallogr. 2004;60(Pt 3):601-5.

90.   Landau EM, Rosenbusch JP. Lipidic cubic phases: a novel concept for the crystallization of membrane proteins. Proc Natl Acad Sci U S A. 1996;93(25):14532-5. PMCID: 26167.

91.   Luecke H, Richter HT, Lanyi JK. Proton transfer pathways in bacteriorhodopsin at 2.3 angstrom resolution. Science. 1998;280(5371):1934-7.

92.   Pebay-Peyroula E, Rummel G, Rosenbusch JP, Landau EM. X-ray structure of bacteriorhodopsin at 2.5 angstroms from microcrystals grown in lipidic cubic phases. Science. 1997;277(5332):1676-81.

93.   Faham S, Bowie JU. Bicelle crystallization: a new method for crystallizing membrane proteins yields a monomeric bacteriorhodopsin structure. J Mol Biol. 2002;316(1):1-6.

94.   Czerski L, Sanders CR. Functionality of a membrane protein in bicelles. Anal Biochem. 2000;284(2):327-33.

95.   Bilderback DH, Brock JD, Dale DS, Finkelstein KD, Pfeifer MA, Gruner SM. Energy recovery linac (ERL) coherent hard x-ray sources. New Journal of Physics. 2010;12(3):035011.

96.   Cherezov V, Hanson MA, Griffith MT, Hilgart MC, Sanishvili R, Nagarajan V, et al. Rastering strategy for screening and centring of microcrystal samples of human membrane proteins with a sub-10 ¬µm size X-ray synchrotron beam. Journal of The Royal Society Interface. 2009;6(Suppl 5):S587-S97.

97.   Perrakis A, Cipriani F, Castagna JC, Claustre L, Burghammer M, Riekel C, et al. Protein microcrystals and the design of a microdiffractometer: current experience and plans at EMBL and ESRF/ID13. Acta Crystallogr D Biol Crystallogr. 1999;55(Pt 10):1765-70.

98.   Meents A, Gutmann S, Wagner A, Schulze-Briese C. Origin and temperature dependence of radiation damage in biological samples at cryogenic temperatures. Proc Natl Acad Sci U S A. 2010;107(3):1094-9. PMCID: 2798883.

99.   Arthur J, Materlik G, Tatchyn R, Winick H. The LCLS: A fourth generation light source using the SLAC linac. Review of Scientific Instruments. 1995;66(2):1987-9.

100.   Hunter MS, DePonte DP, Shapiro DA, Kirian RA, Wang X, Starodub D, et al. X-ray diffraction from membrane protein nanocrystals. Biophys J. 2011;100(1):198-206. PMCID: 3010013.

101.   DePonte DP, Weierstall U, Schmidt K, Warner J, Starodub D, Spence JCH, et al. Gas dynamic virtual nozzle for generation of microscopic droplet streams. J Phys D Appl Phys. 2008;41(19).

102.   Henderson R. The potential and limitations of neutrons, electrons and X-rays for atomic resolution microscopy of unstained biological molecules. Q Rev Biophys. 1995;28(2):171-93.

103.   Wisedchaisri G, Gonen T. Fragment-based phase extension for three-dimensional structure determination of membrane proteins by electron crystallography. Structure. 2011;19(7):976-87. PMCID: 3153127.

104.   Wisedchaisri G, Reichow SL, Gonen T. Advances in structural and functional analysis of membrane proteins by electron crystallography. Structure. 2011;19(10):1381-93. PMCID: 3197218.

105.   Glaeser RM. Limitations to significant information in biological electron microscopy as a result of radiation damage. J Ultrastruct Res. 1971;36(3):466-82.

106.   Nederlof I, van Genderen E, Li YW, Abrahams JP. A Medipix quantum area detector allows rotation electron diffraction data collection from submicrometre three-dimensional protein crystals. Acta Crystallogr D Biol Crystallogr. 2013;69(Pt 7):1223-30. PMCID: 3689525.

107.   Shi D, Nannenga BL, Iadanza MG, Gonen T. Three-dimensional electron crystallography of protein microcrystals. Elife. 2013;2:e01345. PMCID: 3831942.

108.   Siu FY, He M, de Graaf C, Han GW, Yang D, Zhang Z, et al. Structure of the human glucagon class B G-protein-coupled receptor. Nature. 2013;499(7459):444-9. PMCID: 3820480.

109.   Hollenstein K, Kean J, Bortolato A, Cheng RK, Dore AS, Jazayeri A, et al. Structure of class B GPCR corticotropin-releasing factor receptor 1. Nature. 2013;499(7459):438-43.

110.   ter Haar E, Koth CM, Abdul-Manan N, Swenson L, Coll JT, Lippke JA, et al. Crystal structure of the ectodomain complex of the CGRP receptor, a class-B GPCR, reveals the site of drug antagonism. Structure. 2010;18(9):1083-93.

111.   Tan YV, Couvineau A, Murail S, Ceraudo E, Neumann JM, Lacapere JJ, et al. Peptide agonist docking in the N-terminal ectodomain of a class II G protein-coupled receptor, the VPAC1 receptor. Photoaffinity, NMR, and molecular modeling. J Biol Chem. 2006;281(18):12792-8.

112.   Underwood CR, Garibay P, Knudsen LB, Hastrup S, Peters GH, Rudolph R, et al. Crystal structure of glucagon-like peptide-1 in complex with the extracellular domain of the glucagon-like peptide-1 receptor. J Biol Chem. 2010;285(1):723-30. PMCID: 2804221.

113.   Bisello A, Greenberg Z, Behar V, Rosenblatt M, Suva LJ, Chorev M. Role of glycosylation in expression and function of the human parathyroid hormone/parathyroid hormone-related protein receptor. Biochemistry. 1996;35(49):15890-5.

114.   Pioszak AA, Parker NR, Gardella TJ, Xu HE. Structural basis for parathyroid hormone-related protein binding to the parathyroid hormone receptor and design of conformation-selective peptides. J Biol Chem. 2009;284(41):28382-91. PMCID: 2788887.

115.   Garcia-Ruiz JM, Morena A. Investigations on protein crystal growth by the gel acupuncture method. Acta Crystallogr D Biol Crystallogr. 1994;50(Pt 4):484-90.

116.   Faham S, Ujwal R, Abramson J, Bowie JU, Larry D. Practical aspects of membrane proteins crystallization in bicelles. Curr Top Membr. 2009;63:109-25.

117.   Aquila A, Hunter MS, Doak RB, Kirian RA, Fromme P, White TA, et al. Time-resolved protein nanocrystallography using an X-ray free-electron laser. Opt Express. 2012;20(3):2706-16. PMCID: 3413412.

118.   Boutet S, Lomb L, Williams GJ, Barends TR, Aquila A, Doak RB, et al. High-resolution protein structure determination by serial femtosecond crystallography. Science. 2012;337(6092):362-4.

119.   Kern J, Alonso-Mori R, Tran R, Hattne J, Gildea RJ, Echols N, et al. Simultaneous femtosecond X-ray spectroscopy and diffraction of photosystem II at room temperature. Science. 2013;340(6131):491-5.

120.   Koopmann R, Cupelli K, Redecke L, Nass K, Deponte DP, White TA, et al. In vivo protein crystallization opens new routes in structural biology. Nat Methods. 2012;9(3):259-62. PMCID: 3429599.

121.   Redecke L, Nass K, DePonte DP, White TA, Rehders D, Barty A, et al. Natively inhibited Trypanosoma brucei cathepsin B structure determined by using an X-ray laser. Science. 2013;339(6116):227-30.

122.   Chapman HN, Fromme P, Barty A, White TA, Kirian RA, Aquila A, et al. Femtosecond X-ray protein nanocrystallography. Nature. 2011;470(7332):73-7. PMCID: 3429598.

123.   Kern J, Alonso-Mori R, Hellmich J, Tran R, Hattne J, Laksmono H, et al. Room temperature femtosecond X-ray diffraction of photosystem II microcrystals. Proc Natl Acad Sci U S A. 2012;109(25):9721-6. PMCID: 3382516.

124.   Kissick DJ, Wanapun D, Simpson GJ. Second-order nonlinear optical imaging of chiral crystals. Annu Rev Anal Chem (Palo Alto Calif). 2011;4:419-37. PMCID: 3345893.

125.   Haupert LM, Simpson GJ. Screening of protein crystallization trials by second order nonlinear optical imaging of chiral crystals (SONICC). Methods. 2011;55(4):379-86. PMCID: 3264792.

126.   Judge RA, Swift K, Gonzalez C. An ultraviolet fluorescence-based method for identifying and distinguishing protein crystals. Acta Crystallogr D Biol Crystallogr. 2005;61(Pt 1):60-6.

127.   Wampler RD, Kissick DJ, Dehen CJ, Gualtieri EJ, Grey JL, Wang HF, et al. Selective detection of protein crystals by second harmonic microscopy. J Am Chem Soc. 2008;130(43):14076-7.

128.   Kadima W, McPherson A, Dunn MF, Jurnak FA. Characterization of precrystallization aggregation of canavalin by dynamic light scattering. Biophys J. 1990;57(1):125-32. PMCID: 1280649.

129.   Gill HS. Evaluating the efficacy of tryptophan fluorescence and absorbance as a selection tool for identifying protein crystals. Acta Crystallogr F. 2010;66:364-72.

130.   Du S, Betts L, Yang R, Shi H, Concel J, Ahn J, et al. Structure of the HIV-1 full-length capsid protein in a conformationally trapped unassembled state induced by small-molecule binding. J Mol Biol. 2011;406(3):371-86. PMCID: 3194004.

131.   Desbois S, Seabrook SA, Newman J. Some practical guidelines for UV imaging in the protein crystallization laboratory. Acta Crystallogr Sect F Struct Biol Cryst Commun. 2013;69(Pt 2):201-8. PMCID: 3564629.

132.   Nederlof I, Li YW, van Heel M, Abrahams JP. Imaging protein three-dimensional nanocrystals with cryo-EM. Acta Crystallogr D Biol Crystallogr. 2013;69(Pt 5):852-9.

133.   Pullara F, Guerrero-Santoro J, Calero M, Zhang Q, Peng Y, Spahr H, et al. A general path for large-scale solubilization of cellular proteins: from membrane receptors to multiprotein complexes. Protein Expr Purif. 2013;87(2):111-9.

134.   Wong FT, Jin X, Mathews, II, Cane DE, Khosla C. Structure and mechanism of the trans-acting acyltransferase from the disorazole synthase. Biochemistry. 2011;50(30):6539-48. PMCID: 3144309.

135.   Takagi Y, Calero G, Komori H, Brown JA, Ehrensberger AH, Hudmon A, et al. Head module control of mediator interactions. Mol Cell. 2006;23(3):355-64.

136.   Dieryck W, Noubhani AM, Coulon D, Santarelli X. Cloning, expression and two-step purification of recombinant His-tag enhanced green fluorescent protein over-expressed in Escherichia coli. J Chromatogr B Analyt Technol Biomed Life Sci. 2003;786(1-2):153-9.

137.   Stevenson HP MA, Calero M, Edwards A, Zeldin OB, Mathews II, Lin G, Barnes CO, Santamaria H, Ross T, Soltis M, Khosla C, NagarajanV, Conway JF, Cohen AE and Calero G.

Use of Transmission Electron Microscopy to Identify Nanocrystals of Challenging Protein Targets. Proc Natl Acad Sci USA. 2014.

138.   Boutet Sb, Williams GJ. The coherent X-ray imaging (CXI) instrument at the Linac Coherent Light Source (LCLS). New Journal of Physics. 2010;12(3):035024.

139.   Sauter NK, Hattne J, Grosse-Kunstleve RW, Echols N. New Python-based methods for data processing. Acta Crystallogr D Biol Crystallogr. 2013;69(Pt 7):1274-82. PMCID: 3689530.

140.   Neutze R, Wouts R, van der Spoel D, Weckert E, Hajdu J. Potential for biomolecular imaging with femtosecond X-ray pulses. Nature. 2000;406(6797):752-7.

141.   Hunter MS, Fromme P. Toward structure determination using membrane-protein nanocrystals and microcrystals. Methods. 2011;55(4):387-404. PMCID: 3414265.

142.   DePonte DP, Doak RB, Hunter M, Liu Z, Weierstall U, Spence JC. SEM imaging of liquid jets. Micron. 2009;40(4):507-9.

143.   Johansson LC, Arnlund D, White TA, Katona G, Deponte DP, Weierstall U, et al. Lipidic phase membrane protein serial femtosecond crystallography. Nat Methods. 2012;9(3):263-5. PMCID: 3438231.

144.   Lomb L, Barends TR, Kassemeyer S, Aquila A, Epp SW, Erk B, et al. Radiation damage in protein serial femtosecond crystallography using an x-ray free-electron laser. Phys Rev B. 2011;84(21):214111.

145.   Barty A, Caleman C, Aquila A, Timneanu N, Lomb L, White TA, et al. Self-terminating diffraction gates femtosecond X-ray nanocrystallography measurements. Nat Photonics. 2012;6:35-40. PMCID: 3783007.

146.   Barends TR, Foucar L, Botha S, Doak RB, Shoeman RL, Nass K, et al. De novo protein crystal structure determination from X-ray free-electron laser data. Nature. 2014;505(7482):244-7.

147.   Sierra RG, Laksmono H, Kern J, Tran R, Hattne J, Alonso-Mori R, et al. Nanoflow electrospinning serial femtosecond crystallography. Acta Crystallogr D Biol Crystallogr. 2012;68(Pt 11):1584-7. PMCID: 3478121.

148.   Hart P, Boutet Sb, Carini G, Dubrovin M, Duda B, Fritz D, et al., editors. The CSPAD megapixel x-ray camera at LCLS. Proc SPIE; 2012.

149.   Carpenter EP, Beis K, Cameron AD, Iwata S. Overcoming the challenges of membrane protein crystallography. Curr Opin Struct Biol. 2008;18(5):581-6. PMCID: 2580798.

150.   Mokhonova EI, Mokhonov VV, Akama H, Nakae T. Forceful large-scale expression of "problematic" membrane proteins. Biochem Biophys Res Commun. 2005;327(3):650-5.

151.   Saida F, Uzan M, Odaert B, Bontems F. Expression of highly toxic genes in E. coli: special strategies and genetic tools. Curr Protein Pept Sci. 2006;7(1):47-56.

152.   Gibbs CS, Zoller MJ. Identification of Electrostatic Interactions That Determine the Phosphorylation Site Specificity of the Camp-Dependent Protein-Kinase. Biochemistry. 1991;30(22):5329-34.

153.   Ashkenazi A, Presta LG, Marsters SA, Camerato TR, Rosenthal KA, Fendly BM, et al. Mapping the CD4 binding site for human immunodeficiency virus by alanine-scanning mutagenesis. Proc Natl Acad Sci U S A. 1990;87(18):7150-4. PMCID: 54701.

154.   Cunningham BC, Wells JA. High-resolution epitope mapping of hGH-receptor interactions by alanine-scanning mutagenesis. Science. 1989;244(4908):1081-5.

155.   Blaber M, Baase WA, Gassner N, Matthews BW. Alanine Scanning Mutagenesis of the Alpha-Helix-115-123 of Phage-T4 Lysozyme - Effects on Structure, Stability and the Binding of Solvent. Journal of molecular biology. 1995;246(2):317-30.

156.   Dupeux F, Rower M, Seroul G, Blot D, Marquez JA. A thermal stability assay can help to estimate the crystallization likelihood of biological samples. Acta Crystallogr D. 2011;67:915-9.

157.   Bae E, Bannen RM, Phillips GN. Bioinformatic method for protein thermal stabilization by structural entropy optimization. P Natl Acad Sci USA. 2008;105(28):9594-7.

158.   Hino T, Arakawa T, Iwanari H, Yurugi-Kobayashi T, Ikeda-Suno C, Nakada-Nakura Y, et al. G-protein-coupled receptor inactivation by an allosteric inverse-agonist antibody. Nature. 2012;482(7384):237-40. PMCID: 3303121.

159.   Day PW, Rasmussen SG, Parnot C, Fung JJ, Masood A, Kobilka TS, et al. A monoclonal antibody for G protein-coupled receptor crystallography. Nat Methods. 2007;4(11):927-9.

160.   Steyaert J, Kobilka BK. Nanobody stabilization of G protein-coupled receptor conformational states. Curr Opin Struct Biol. 2011;21(4):567-72. PMCID: 3166880.

161.   Richardson DC, Bier CJ, Richardson JS. Two crystal forms of bovine superoxide dismutase. J Biol Chem. 1972;247(19):6368-9.

162.   Lundstrom K, Wagner R, Reinhart C, Desmyter A, Cherouati N, Magnin T, et al. Structural genomics on membrane proteins: comparison of more than 100 GPCRs in 3 expression systems. Journal of structural and functional genomics. 2006;7(2):77-91.

163.   CHAPOT MÄ, ESHDAT Y, MARULLO S, GUILLET JÄr, CHARBIT A, STROSBERG AD, et al. Localization and characterization of three different Œ≤‚Äêadrenergic receptors expressed in Escherichia coli. European Journal of Biochemistry. 1990;187(1):137-44.

164.   Sarramegna V, Talmont F, Demange P, Milon A. Heterologous expression of G-protein-coupled receptors: comparison of expression systems from the standpoint of large-scale production and purification. Cell Mol Life Sci. 2003;60(8):1529-46.

165.   Grisshammer R, Duckworth R, Henderson R. Expression of a rat neurotensin receptor in Escherichia coli. Biochem J. 1993;295 (Pt 2):571-6. PMCID: 1134918.

166.   Grisshammer R, Averbeck P, Sohal AK. Improved purification of a rat neurotensin receptor expressed in Escherichia coli. Biochem Soc Trans. 1999;27(6):899-903.

167.   Lusty CJ. A gentle vapor-diffusion technique for cross-linking of protein crystals for cryocrystallography. Journal of applied crystallography. 1999;32(1):106-12.

168.   Heras B, Martin JL. Post-crystallization treatments for improving diffraction quality of protein crystals. Acta Crystallographica Section D. 2005;61(9):1173-80.

169.   Wine Y, Cohen‚ÄêHadar N, Freeman A, Frolow F. Elucidation of the mechanism and end products of glutaraldehyde crosslinking reaction by X‚Äêray structure analysis. Biotechnol Bioeng. 2007;98(3):711-8.

170.   Newman J. A review of techniques for maximizing diffraction from a protein crystal in stilla. Acta Crystallographica Section D: Biological Crystallography. 2005;62(1):27-31.

171.   Dierks K, Meyer A, Einspahr H, Betzel C. Dynamic light scattering in protein crystallization droplets: Adaptations for analysis and optimization of crystallization processes. Crystal Growth and Design. 2008;8(5):1628-34.